

General Disclaimer

One or more of the Following Statements may affect this Document

- This document has been reproduced from the best copy furnished by the organizational source. It is being released in the interest of making available as much information as possible.
- This document may contain data, which exceeds the sheet parameters. It was furnished in this condition by the organizational source and is the best copy available.
- This document may contain tone-on-tone or color graphs, charts and/or pictures, which have been reproduced in black and white.
- This document is paginated as submitted by the original source.
- Portions of this document are not fully legible due to the historical nature of some of the material. However, it is the best reproduction available from the original submission.

25
SQT

REPORT NO. CR-165140

(NASA-CR-165140) ANALYSIS AND DESIGN OF ION
THRUSTER FOR LARGE SPACE SYSTEMS Final
Report, 21 May 1979 - 21 May 1980 (Hughes
Research Labs.) 113 p HC A06/MF A01

N83-14158

Unclas

CSCL 21C G3/20 02299

ANALYSIS AND DESIGN OF ION THRUSTERS FOR LARGE SPACE SYSTEMS

R.L. Poeschel and S. Kami

Hughes Research Laboratories

3011 Malibu Canyon Road

Malibu, CA 90265

September 1980

NAS 3-21936

Final Report

21 May 1979 through 21 May 1980

Unclassified - limited

Sponsored by

NASA LEWIS RESEARCH CENTER

21000 Brookpark Road

Cleveland, OH 44135



1. Report No. CR-165140	2. Government Accession No.	3. Recipient's Catalog No.	
4. Title and Subtitle ANALYSIS AND DESIGN OF ION THRUSTERS FOR LARGE SPACE SYSTEMS		5. Report Date September 1980	
		6. Performing Organization Code	
7. Author(s) R.L. Poeschel and S. Kami		8. Performing Organization Report No.	
		10. Work Unit No.	
9. Performing Organization Name and Address Hughes Research Laboratories 3011 Malibu Canyon Road Malibu, CA 90365		11. Contract or Grant No. NAS 3-21936	
		13. Type of Report and Period Covered Final Report 17 May 1979 - 17 May 1980	
12. Sponsoring Agency Name and Address NASA Lewis Research Center 21000 Brookpark Road Cleveland, OH 44135		14. Sponsoring Agency Code	
15. Supplementary Notes Project Manager: Shigeo Nakanishi, NASA Lewis Research Center, Cleveland, Ohio.			
16. Abstract The work performed under this contract was an initial step in advancing "state-of-the-art" ion thruster technology to meet the requirements for both prime propulsion and stationkeeping functions on the large space platforms that are envisioned in the late 1980s, early 1990s time frame. The principal new requirements are higher thrust, the use of inert-gas propellants (argon or xenon), and the capability for scaling using a homologous thruster design. Other objectives that typify ion propulsion systems, such as long lifetime, high efficiency, etc., were also requirements for this design effort. The work performed resulted in the formulation of a conceptual design for a thruster that would produce 0.5-N thrust. No restrictions were placed on the approach used, and the design was based on technical feasibility and performance potential rather than on traditional techniques for fabrication. Emphasis was placed on use of concepts that can be supported analytically or substantiated in part by existing empirical data. The conceptual design consists of drawings and sketches, calculations and analytic models, and narrative descriptions of the recommended 50-cm-diameter multipole thruster. The projected performance of the proposed thruster meets the contractual goals for thruster efficiency and operating specifications.			
17. Key Words (Suggested by Author(s)) Electric propulsion Inert gas ion thruster Large communication satellites Solar power satellites		18. Distribution Statement Unclassified - limited	
19. Security Classif. (of this report) UNCLASSIFIED	20. Security Classif. (of this page) UNCLASSIFIED	21. No. of Pages 115	22. Price*

* For sale by the National Technical Information Service, Springfield, Virginia 22161

FOREWORD

The work described herein was performed primarily at Hughes Research Laboratories by staff members of the Ion Physics Department and the High Voltage Technology Department. The program manager and principal investigator was Dr. R.L. Poeschel (now manager of the Ion Propulsion Project). Key technical contributions were made by Professors Harold R. Kaufman and Paul J. Wilbur, as consultants from Colorado State University. The roles of the key contributors are outlined below:

R.L. Poeschel	—	Program Manager and Principal Investigator
S. Kami	—	Assistant Program Manager and Design Engineer
C. Ball	—	Consultant, Structural Analysis
H.R. Kaufman	—	Consultant
P.J. Wilbur	—	Consultant
H.J. King	}	Internal Design Review
C.R. Collett		
C.R. Dulgeroff		
J. Hyman, Jr.		
J.R. Beattie		
J.H. Molitor		

PRECEDING PAGE BLANK NOT FILMED

TABLE OF CONTENTS

SECTION	PAGE
SUMMARY	9
1 INTRODUCTION	11
2 DESIGN ANALYSES	13
A. Design Goals	13
B. Design Drivers	13
C. Computational Procedures	15
D. Thruster Lifetime Computation	27
E. Magnetic Field Calculations	32
F. Thermal and Mechanical Design Considerations	37
3 RECOMMENDED CONCEPTUAL DESIGN	51
A. Power Processor Requirements	55
B. Technology Areas that Require Verification	58
4 CONCLUSIONS	61
REFERENCES	65
APPENDICES	
A THRUSTER PERFORMANCE CHARACTERIZATION	67
B DETERMINATION OF MULTIPLY CHARGED ION EFFECTS	99

PRECEDING PAGE BLANK NOT FILMED

LIST OF ILLUSTRATIONS

FIGURE		PAGE
1	Thrust versus beam diameter for argon propellant with specific impulse as a parameter	16
2	Thrust versus beam diameter for xenon propellant with specific impulse as a parameter	17
3	Comparison of thruster efficiency (corrected for doubly charged ions and beam divergence) as a function of discharge chamber length for operation with xenon and argon propellants	26
4	Variation of the grid lifetime parameter as a function of the plasma parameter C (xenon)	29
5	Variation of the grid lifetime parameter as a function of the plasma parameter C (argon)	30
6	Demagnetization curve for ALNICO 8	33
7	Typical discharge-chamber configuration for multipole magnetic confinement	34
8	Typical magnet/pole-piece cross section showing anode configuration that provides for direct radiation of thermal input	38
9	Steady-state temperature attained by radiation cooling as a function of surface emissivity	40
10	Magnet properties that limit thruster operating temperature	41
11	Isometric view of the computer modeling for a 2-grid 50-cm thruster ion-optics assembly	45
12	Isometric view of the computer modeling for a 3-grid 50-cm thruster ion-optics assembly	45
13	Cross section of the ion accelerator grid assembly for the J-series 30-cm thruster showing temperatures used in stress analysis	47
14	Cross section of the ion accelerator grid assembly showing temperatures representative of thermal input	47

FIGURE		PAGE
15	Ion-optics model showing temperatures assumed for condition that operating temperature would be 100°C greater than for $J_b = 6 \text{ A}$	48
16	Plane view — 50-cm x 100-cm oval accel electrode model	49
17	Displacements of model elements in thermal expansion	50
18	Layout drawing of the proposed thruster diagram	52
19	Block diagram showing proposed thruster power processor requirements	56
20	Block diagram showing four-cathode control concept	57

SUMMARY

The objective of this study was to formulate a conceptual design for an ion thruster that would meet the anticipated performance requirements of large space systems. The principal thruster performance goals for the design analysis performed under this contract were a thrust of 0.5 N, operation on inert gas propellant (xenon or argon), operation at a specific impulse of 3530 sec for xenon and 6076 for argon, and achievement of a total thruster efficiency of 74% for xenon and 68% for argon. The design study was totally analytic, drawing heavily on the analytic models for inert gas thruster operation that have been developed at Colorado State University. As a consequence, the thruster discharge chamber makes use of a multipole magnetic confinement configuration for which scaling and analytic description have been demonstrated. To achieve the thruster efficiency goals, a beam diameter of approximately 50 cm was found to be necessary. Having determined that this was the major design driver, tractable solutions to all of the remaining design problems were worked out (in concept). The resultant conceptual design for the 50-cm inert-gas thruster provides a promising basis for further engineering and confirmation of untested design approaches (such as multiple hollow cathode operation).

SECTION 1

INTRODUCTION

Ion thruster development has concentrated primarily on mercury electron bombardment thrusters that accelerate mercury ions electrostatically. The technology for thrusters producing 8-cm and 30-cm-diameter ion beams (producing thrust levels of 5 mN and 125 mN, respectively) has reached a relatively advanced status. These thrusters are now considered ready for application as auxiliary propulsion (8-cm thrusters) for satellites in earth-orbit and for primary propulsion (30-cm thrusters) for interplanetary exploration. Projecting to the future, large space systems (LSS) are contemplated for near-earth space platforms (earth orbital systems) having a variety of functions. To be cost effective, ion thrusters would have to produce greater thrust (per thruster), have long life, and be compatible with other LSS functions. The work described in this report represents an initial analysis and conceptual design for an ion thruster to meet the projected requirements of LSS.

Environmental concerns over the relatively large quantities of propellant that would be required for an LSS preclude using mercury as a propellant, and argon and xenon were specified as the required alternative propellants. This represented the major design constraint, and the design analyses were performed with the objective of showing the capability of the thruster concept developed for meeting the performance and operational characteristics specified as the contract goals. At the outset, these goals (described in Section 2) seemed to be a challenging, if not overly ambitious, extrapolation from the state of the art. At the completion of the analyses, however, the contractual goals appear realizable with some reasonable and realistic assumptions about scaling the thruster design using experimentally verified principles and correlation parameters. With regard to performance analyses and experimental correlations, the work reported herein draws heavily on research conducted at Colorado State University¹⁻¹⁵ (under NASA grants).

SECTION 2

DESIGN ANALYSES

The analysis of ion thruster performance must take into account several figures of merit (such as efficiency, operating range, and reliability) that are interdependent. Consequently, we began by evaluating the design goals with respect to which characteristic was most difficult to satisfy. This section describes the design goals, identifies the design drivers, and outlines the computational procedures used to obtain the required thruster characteristics.

A. DESIGN GOALS

The design goals specified in the statement of work for this contract are summarized in Table 1. The dominant independent parameters specified in this table are thrust, specific impulse, and type of propellant. As shown below, all the other quantities have to be derived from these three quantities using analytic models for thruster performance. Since analytic models for ion thruster performance are only reliable for certain thruster configurations, the design features specifying module scalability, variable thrust, and specific impulse are more restrictive than might appear. Only the multipole discharge chamber geometry described by Isaacson⁶ has been scaled analytically and verified experimentally. Scalability is the major design driver for discharge chamber configuration. Other design drivers are discussed in the following section.

B. DESIGN DRIVERS

We initially thought that thruster lifetime would be the major design driver dictating thruster diameter. But computation of thruster efficiency (based on specifying the design parameters to satisfy screen grid lifetime) showed that thruster efficiency goals could not be satisfied using this approach; therefore, satisfying efficiency became the major design driver. Efficiency computations by Kaufman (described in Appendix A and also in Ref. 12) were useful in defining the thruster

Table 1. Specifications for Design of a Thruster for
LSS Application (Design Goals)

Propellant: inert gases argon or xenon

Thrust: 0.5 N

Specific impulse:

Argon, 6076 sec

Xenon, 3530 sec

Thruster efficiency:

Argon, 68%

Xenon, 74%

Lifetime: 15,000 hr

Design features

- Specific impulse and thrust variable $\pm 50\%$
- Module scalable from half to double nominal
- Constructed from commercially available materials
- Concepts ultimately applicable to space flight
- Unitized construction for possible replacement of critical components

diameter through the relationships shown in Figures 1 and 2. These computations were made under the assumption that the thruster can be operated at a discharge voltage sufficiently low to neglect the effects of doubly or triply charged ions. Unless the ratio of the length of the discharge chamber to its diameter is very small, multiply charged ion effects are found to be appreciable for operation with xenon as the propellant. Accounting for these effects was facilitated using the analyses and design curves prepared by Wilbur and presented in Appendix B. Using overall thruster efficiency as the major design driver, the computational technique used in defining the design is described in Section 2.C.

C. COMPUTATIONAL PROCEDURES

To compute the theoretical performance of an ion thruster, the quantities identified in Table 2 must be specified or computed using the relationships derived by Kaufman and Wilbur¹⁰ and described in detail in Appendices A and B. Having noted from the cross-plots of Kaufman's results shown in Figures 1 and 2 that the beam diameter for maximum thruster efficiency is ~44 cm for the values of thrust and specific impulse under consideration here, it remained to determine the optimum discharge chamber length. For computational purposes, we assumed that the cyclic pole-piece/anode dimension is 2.7 cm (the same as that used by Isaacsen at Colorado State University). The thruster operating parameters and total efficiency were computed as a function of discharge chamber length to obtain the values listed in Table 3; the procedure is illustrated by the sample calculation for xenon propellant which follows. A nominal beam diameter of 50 cm has been assumed for these computations.

ORIGINAL DESIGN BY
OF POOR QUALITY

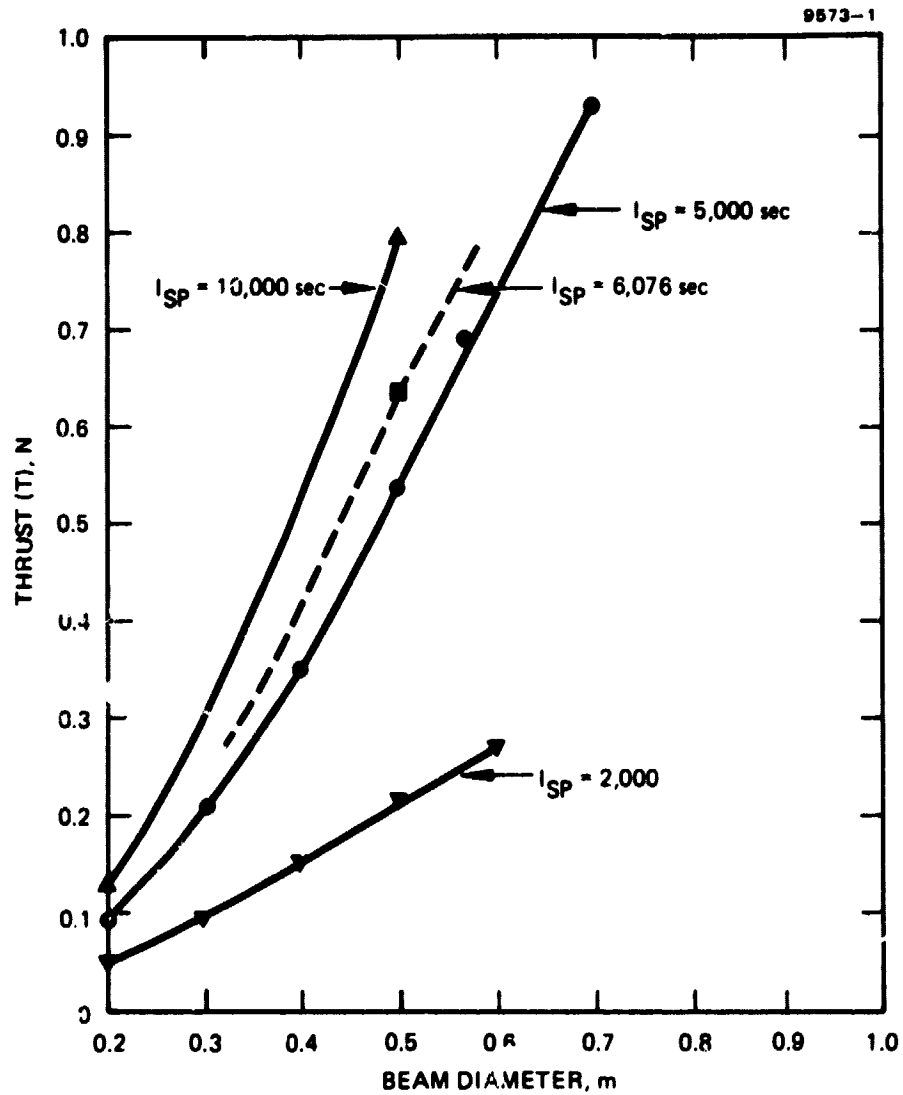


Figure 1. Thrust versus beam diameter for argon propellant with specific impulse as a parameter (thruster operated for maximum efficiency). Dashed line is specific impulse design goal.

OPTIMAL DESIGN OF POOR QUALITY

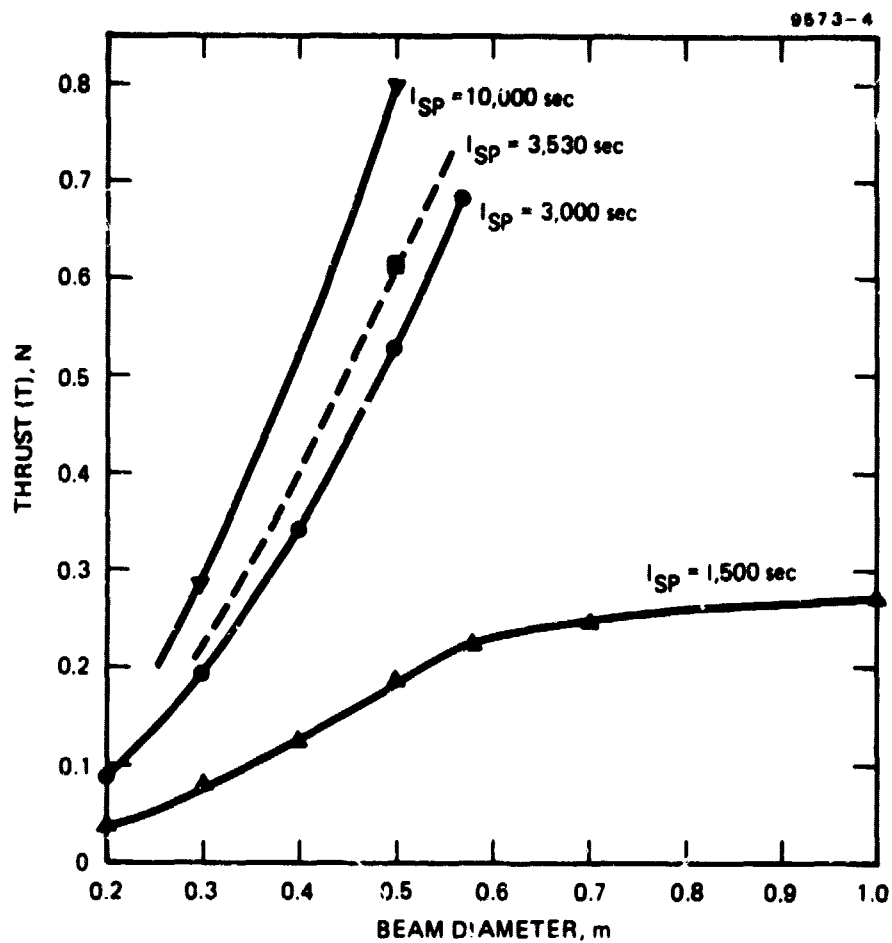


Figure 2. Thrust versus beam diameter for xenon propellant with specific impulse as a parameter (thruster operated for maximum efficiency). Dashed line is specific impulse design goal.

ORIGINAL PAGE IS
OF POOR QUALITY

Table 2. Definition of Symbols Used for the Quantities Necessary for Computing Thruster Performance Characteristics (Including Assigned Values where Applicable)

Quantity	Symbol	Value
Propellant mass	m_0	
Specific impulse	I_{sp}	
Thrust	T	
Beam diameter	d_b	
Beam area	A_b	
Discharge chamber length	l_d	
Accelerator grid transmission	ϕ_a	0.2
Screen grid transmission	ϕ_s	0.7
Screen grid thickness	t_s	0.051 cm
Beam voltage	V_b	
Beam current	J_b	
Beam power	P_b	
Beam uniformity parameter	F_b	0.95
Total thrust correction factor	r	
Discharge voltage	V_d	
Emission current	J_E	
Discharge power	P_D	
Neutral propellant flow	J_0	
Propellant efficiency (measured)	η_m	
Electrical efficiency	η_e	
Thrust correction factor for beam divergence	F_c	0.985
Thrust efficiency	η_T	
Thruster (screen grid) lifetime	Z	
Primary electron region surface area	A_p	
Primary electron region volume	V_p	
Electron temperature (Maxwellian)	T_e	4 eV
Plasma uniformity factor	F_+	5 or 7
Neutral atom velocity	v_0	$\approx 800^\circ K$
Bohm velocity (ions)	v_+	
Neutral loss parameter	P_{NL}	3.4 (Ar); 0.61 (Xe)
Discharge loss parameter	P_{DL}	67 (Ar); 62.2 (Xe)
Ionization efficiency	η_i	
Flux of singly charged ions	Γ_+	
Flux of doubly charged ions	Γ_{++}	
Discharge plasma parameter	C_j	
Ionization rate factors	Z_1	
Ratio of doubly to singly charged ion flux	Γ_{++}/Γ_+	
Thrust correction factor for doubly charged ions	ϵ	
Primary electron confinement parameter	$/Bd_x$	54×10^{-6} Tesla-m
Anode area	A_A	
Maximum anode current	J_{AN}	
Specific discharge power	P_{SD}	
Minimum discharge voltage	V_{DM}	
Sputtering yield for singly charged ions	S^+	
Sputtering yield for doubly charged ions	S^{++}	
Density of screen grid material	ρ	$6.4 \times 10^{22} \text{ cm}^{-3}$
Total acceleration voltage	V_T	
Ratio of beam voltage to total acceleration voltage	R	

7174

Table 3. Theoretical Operating and Performance Quantities Computed as a Function of Discharge Chamber Length for a 50-cm (beam diameter) Thruster

Propellant	l_d , cm	F_+	η_1	J_b , A	V_b , V	γ	V_{Dm} , V	V_D , V	P_{TOT} , W	η_e , %	η_m , %	η_T , %
Xe	8.1	7	0.950	12.5	760	0.879	24.8	34	11,563	82.1	117.9	74.7
	8.1	5	0.950	12.0	790	0.901	24.8	34	11,460	82.7	113.2	76.0
	10.8	7	0.960	13.0	723	0.864	23.2	34	11,544	81.4	122.6	74.5
	10.8	5	0.960	12.5	755	0.887	23.2	34	11,500	82.1	117.9	76.1
	13.5	7	0.965	13.4	700	0.853	22.1	34	11,591	80.9	126.4	74.4
	13.5	5	0.965	12.8	731	0.875	22.1	34	11,469	81.6	120.7	75.4
Ar	16.2	7	0.969	13.7	683	0.845	21.1	34	11,618	80.5	129.2	74.2
	16.2	5	0.969	13.0	716	0.869	21.1	34	11,453	81.3	122.6	75.2
	8.1	7	0.782	17.5	1114	0.933	54.9	55	23,100	84.4	86.6	63.6
	8.1	5	0.782	17.1	1138	0.945	54.9	55	22,983	84.7	84.6	63.9
	10.8	7	0.824	18.6	997	0.930	50.6	51	22,376	82.9	92.0	66.0
	10.8	5	0.824	18.1	1022	0.943	50.6	51	22,227	83.2	89.6	66.3
	13.5	7	0.849	19.1	939	0.928	47.2	48	21,870	82.0	94.9	66.2
	13.5	5	0.849	18.5	961	0.943	47.2	48	21,599	82.4	91.6	66.3
	16.2	7	0.865	19.4	911	0.934	44.8	45	21,699	81.6	96.0	68.3
	16.2	5	0.865	18.9	932	0.947	44.8	45	21,508	81.9	93.5	68.6
	18.9	7	0.877	19.5	894	0.938	42.7	43	22,016	79.2	96.5	67.2
	18.9	5	0.877	19.1	910	0.949	42.7	43	21,871	79.4	94.6	67.1

7174

ORIGINAL PAGE IS
OF POOR QUALITY

1. Compute areas and volumes using:

Beam diameter = $d_b = 50$ cm

Chamber length = $\ell_d = 8.1$ cm

a. Primary electron region surface area

$$A_p = 2 \left(\frac{\pi d_b^2}{4} \right) + \pi d_b \ell_d = \pi d_b \left(\frac{d_b}{2} + \ell_d \right) = 0.5182 \text{ m}^2 \quad (1)$$

b. Anode area

$$A_A = \frac{\pi d_b^2}{4} + \pi d_b \ell_d - \underbrace{A_{\text{cath}}}_{\text{area of cathode plus other vacant area}} = 0.3154 \text{ m}^2 \quad (2)$$

c. Beam area

$$A_b = \frac{\pi d_b^2}{4} = 0.1963 \text{ m}^2 \quad (3)$$

d. Primary electron region volume

$$V_p = \frac{\pi d_b^2 \ell_d}{4} = 0.0157 \text{ m}^3 \quad (4)$$

e. Volume-to-surface area ratio — primary electron region

$$\frac{V_p}{A_p} = \frac{d_b \ell_d}{2d_b + 4\ell_d} = 0.0303 \text{ m} \quad (5)$$

ORIGINAL DESIGN
OF POOR QUALITY

2. Compute neutral propellant flow rate

$$J_o = \frac{Te}{I_{sp} m_o g_o} = 10.6 \text{ A} \quad , \quad (6)$$

where T = thrust (in N), $e = 1.6 \times 10^{-19}$ C, I_{sp} = specific impulse (in sec), m_o = propellant atom mass (in kg), and $g_o = 9.8 \text{ m/sec}^2$.

3. Compute ionization efficiency (defined here as the ratio of the ion loss rate to the neutral atom supply)

$$\eta_i = 1 - \frac{P_{NL} A_b \phi_a}{J_o (V_p / A_p)} = 0.95 \quad , \quad (7)$$

where P_{NL} is the neutral loss parameter (from Ref. 6), and ϕ_a is the transparency of the accelerator.

4. Compute the plasma parameter "C" for $F_+ = 5$

$$C = \frac{70}{F_+} \frac{1 - \eta_i}{\eta_i} = 0.53 \quad . \quad (8)$$

5. Compute chamber specific discharge loss level

$$P_{SD} = P_{DL} \frac{A_p}{A_b} = 165 \text{ eV/ion} \quad , \quad (9)$$

where $P_{DL} = 62.2 \text{ eV/ion}$ (obtained from Ref. 6 and adjusted for $\phi_s = 0.7$).

ORIGINAL PAGE IS
OF POOR QUALITY

6. The minimum discharge voltage V_{Dm} is determined by the criterion for multipole thruster anode area, which determines the maximum anode current J_{AM} by the relation

$$J_{AM} = \frac{kT_e n_e A_A}{13fBdx} \quad (10)$$

coupled with the definition of specific discharge power

$$V_{Dm} = \frac{P_{SD} J_b}{J_{AM} - J_b} \quad (11)$$

and the expression for the discharge chamber electron density* (n_e)

$$n_e = n_i = \frac{J_b}{eA_b \phi_s} \sqrt{\frac{m_o}{kT_e}} \quad (12)$$

where T_e is the electron temperature, k is Boltzmann's constant, A_A is the anode area, J_A is the anode current, and J_b is the beam current. Combining the last three equations yields the expression for minimum discharge voltage determined by the anode current limitation:

$$V_{Dm} = \frac{P_{SD}}{\left(\frac{A_A}{A_b}\right) \left(\frac{1}{13\phi_s e f B dx}\right) \left(\sqrt{kT_e m_o}\right) - 1} = 24.8 \quad (13)$$

*The correct expression for density in this case is

$$n_e = \frac{J_b}{eA_b \phi_s} \sqrt{\frac{m_o}{kT_e (1+n_p/n_m)}} \left[\frac{1+\sqrt{2}(\Gamma_{++}/\Gamma_+)}{1+2(\Gamma_{++}/\Gamma_+)} \right] \quad ,$$

but the equation given in this case should be an adequate approximation.

ORIGINAL PAGE IS
OF POOR QUALITY

7. Having determined the minimum value for discharge voltage, one can estimate V_D and $V_D - V_K$ such that

$$V_D > 24.8 \quad . \quad (14)$$

For the proposed design, since $V_D - V_K$ was chosen to be 28 V, and V_K was assumed to be 6 V, it follows that $V_D = 34$ V. The remaining design values are found from the design curves shown in Appendix B. Using the value of 0.53 computed for the plasma parameter, it is found that

$$\Gamma_{++}/\Gamma_+ = 0.27 \quad ; \quad (15)$$

from Figures B-1 and B-3, it is found that

$$V_b \eta_i^2 = 686 \quad (16)$$

$$V_b = 760 \quad . \quad (17)$$

Figure B-4 produces

$$\frac{J_b}{\eta_i} = 12.9 \quad (18)$$

$$J_b = 12.3 \quad , \quad (19)$$

assuming no beam divergence. Including the effect of beam divergence ($F_t = 0.985$),

$$J_b = 12.5 \quad . \quad (20)$$

From Figure B-5, the thrust correction factor for doubly charged ions, α , is found to be

$$\alpha = 0.892 \quad . \quad (21)$$

ORIGINAL PAGE IS
OF POOR QUALITY

The total thrust correction factor becomes

$$\gamma = \alpha F_t = 0.879 , \quad (22)$$

the beam power is

$$P_b = V_b J_b = 9500 , \quad (23)$$

the discharge power is

$$P_D = V_D J_E = J_b P_{SD} = 2062 , \quad (24)$$

and the total power becomes

$$P_{TOT} = P_b + P_D = 11,563 . \quad (25)$$

The electrical efficiency is

$$\eta_e = \frac{P_b}{P_b + P_D} = 0.821 . \quad (26)$$

The propellant efficiency that would be measured in an operating thruster is

$$\eta_m = \frac{J_b}{J_o} = 1.18 . \quad (27)$$

The overall thruster efficiency is

$$\eta_T = \eta_e \eta_m \gamma^2 = 0.747 . \quad (28)$$

This procedure was repeated for all of the values of ℓ_D listed in Table 3.

ORIGINAL PAGE IS
OF POOR QUALITY

If the losses associated with a neutralizer are included, then J_o has to be increased by the neutralizer flow

$$J_{OT} = J_o + J_{ON} \quad (29)$$

$$= 10.6 + 1.0 = 11.6$$

$$\eta_m^* = \frac{J_b}{J_{OT}} = 1.08 \quad (30)$$

Electrical efficiency is modified to be

$$\eta_e^* = \frac{P_b}{P_D + P_b + P_N} = 0.806 \quad (31)$$

$$P_N = 16(J_b + 1.5) = 224 \quad (32)$$

The overall corrected thruster efficiency becomes

$$\eta_T = \eta_m^* \eta_e^* \gamma^2 = 0.672 \quad (33)$$

Note that the values of η_m shown in Table 3 for operation with Xe propellant are always greater than 100% because of the relatively high percentage of doubly charged ions. Surprisingly, as shown in Section 2.D, this high percentage of doubly charged ions does not present a screen-grid lifetime problem. On the other hand, the relatively high discharge voltage required for operation with argon (to satisfy the maximum anode current condition) does present a severe lifetime problem. Triply charged ions could be appreciable if the discharge voltage were greater than 34 V for Xe operation, and if the ionization efficiency (η_i) for Ar operation were to exceed 0.9. Neither of these conditions occurs at the design operating point selected here and therefore the effect of triply charged ions can be neglected.

ORIGINAL PAGE IS
OF POOR QUALITY

A plot of overall thruster efficiency (η_T) as a function of discharge chamber length (ℓ_D), given in Figure 3, shows that the best performance (efficiency) is obtained at a different value of ℓ_D for operation with Ar than for operation with Xe. Specification of an ℓ_D of 16.2 cm produces performance that meets the contractual goals for operation with both Xe and Ar.

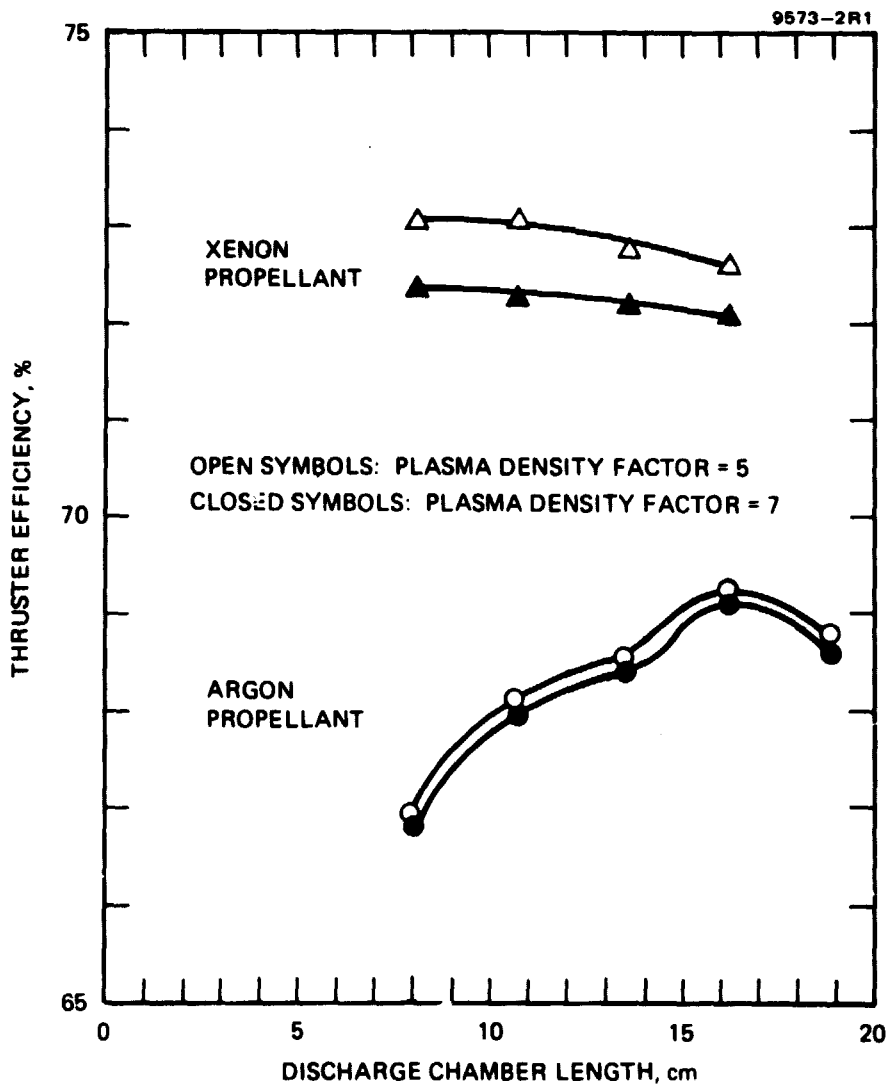


Figure 3. Comparison of thruster efficiency (corrected for doubly charged ions and beam divergence) as a function of discharge chamber length for operation with xenon and argon propellants.

D. THRUSTER LIFETIME COMPUTATION

The principal life-limiting factor has not yet been determined for inert gas ion thrusters; however, it is reasonable to assume that component development will result in the same situation for inert-gas thrusters as for the mercury ion thruster. The screen grid electrode of the ion optics assembly must be fabricated from relatively thin material to achieve efficient ion extraction. If the screen grid is sufficiently thin, it is thought that ions may, in fact, miss the electrode, and hence ion sputtering would not present a lifetime problem. Until this supposition has been verified, the thinning of the ion optics screen grid electrode by ion sputtering is considered to be the principal wearout mechanism. The expression used to calculate the useful lifetime, τ , is

$$\tau = \left(\frac{0.9 t_s e A_b \phi_s F_b \rho}{3600 \eta_i J_o} \right) \left(\frac{1 + \Gamma_{++}/\Gamma_+}{S^+ + S^{++} \Gamma_{++}/\Gamma_+} \right), \quad (34)$$

where τ is the grid lifetime (in hr), t_s is the grid thickness (in cm), A_b is the area of the beam (in cm^2), ϕ_s is the screen grid open area fraction, F_b is the ion beam flatness parameter, ρ is the density of the grid material, S^+ is the sputter yield of the grid material corresponding to the energy of singly charged ions ($\sim V_D$), and S^{++} is the sputter yield for doubly charged ions ($\sim 2 V_D$). The factor 0.9 in the numerator corresponds to an assumed condition of screen grid failure when 90% of the initial grid thickness has been eroded away. Using a grid thickness of 0.051 cm, a screen grid open area fraction of 70%, a beam flatness parameter of 0.95, and other parameters defined previously, Eq. (34) becomes

$$\frac{\tau \eta_i}{A_b} = 8.52 \times 10^{-3} \left(\frac{1 + \Gamma_{++}/\Gamma_+}{S^+ + S^{++} \Gamma_{++}/\Gamma_+} \right). \quad (35)$$

As shown in Appendix B, Γ_{++}/Γ_+ is a function of the plasma parameter C and the electron energy ($V_D - V_K$). The sputtering coefficients S^+ and S^{++} are functions of V_b (see Table 4). If $V_D \approx (V_D - V_K)$, then the life-time parameter $\tau\eta_1/A_b$ can be computed as a function of the plasma parameter, as shown in Figures 4 and 5. If $V_D \gg (V_D - V_K)$, then it is necessary to use the pertinent values of S and Γ_{++}/Γ_+ , respectively, in Eq. 35.

If a thruster is operated on xenon propellant at values of $(V_D - V_K) > 32$ V and relatively higher values of η_1 , then the grid lifetime could be altered appreciably by triply charged ions. The expression for the grid lifetime is

$$\tau = \frac{8.52 \times 10^{-3} A_B}{\eta_1} \left[\frac{1 + \Gamma_{++}/\Gamma_+ + \Gamma_{+++}/\Gamma_+}{S^+ + S^{++}\Gamma_{++}/\Gamma_+ + S^{+++}\Gamma_{+++}/\Gamma_+} \right]. \quad (36)$$

Table 4. Sputtering Coefficients for Sputter Yields of Singly and Doubly Charged Ions on Molybdenum as Functions of Discharge Voltage, V_D .

Gas	V_D	$S^+ \times 10^{-6}$ atoms/ion	$S^{++} \times 10^{-3}$ atoms/ion
Ar	40	40	40
	35	20	16
	34	15	15
	32	9	9
Xe	35	9	5.3
	34	7	4
	32	5	3
	30	2	1.5
	28	1	0.5

ORIGINAL COPY
OF POOR QUALITY

9573-32R1

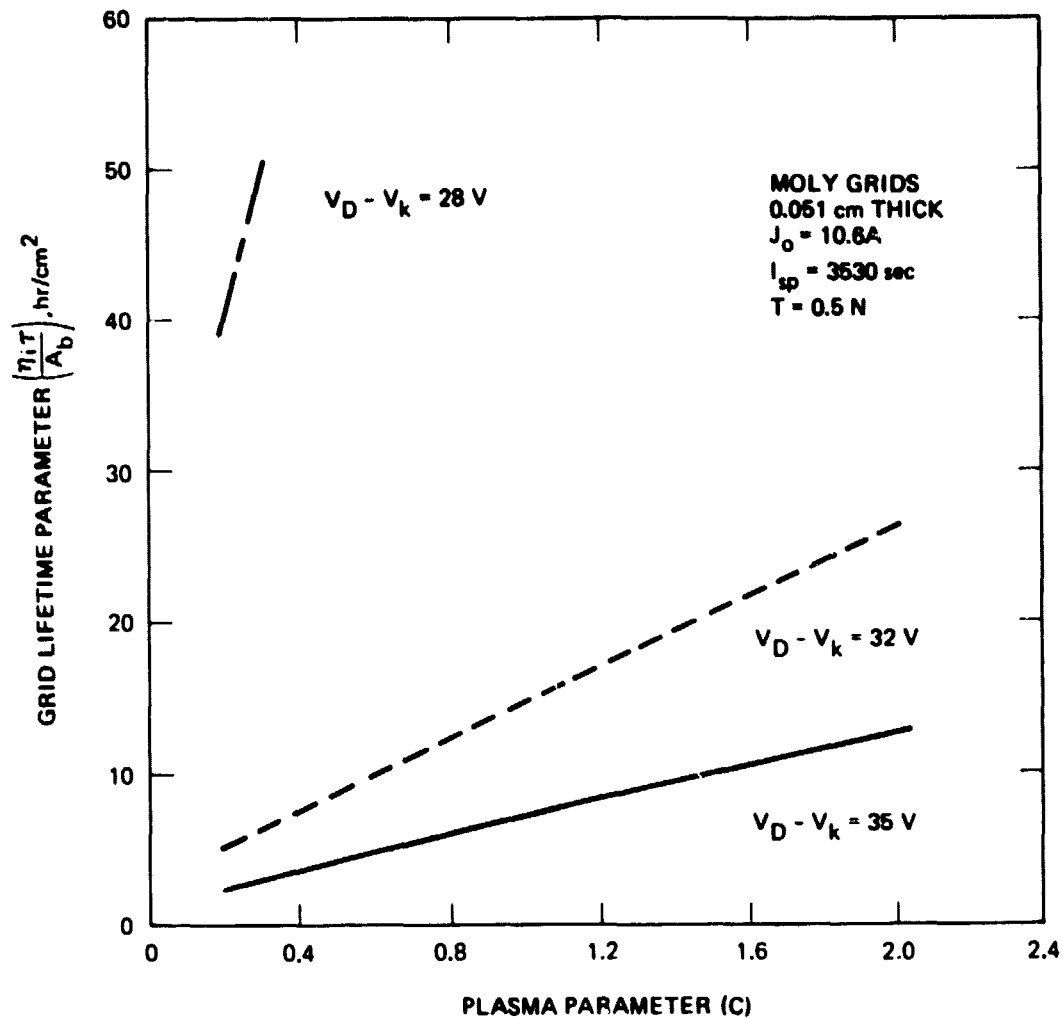


Figure 4. Variation of the grid lifetime parameter as a function of the plasma parameter C. (Xenon propellant).

ORIGINAL STATE OF
OF POOR QUALITY

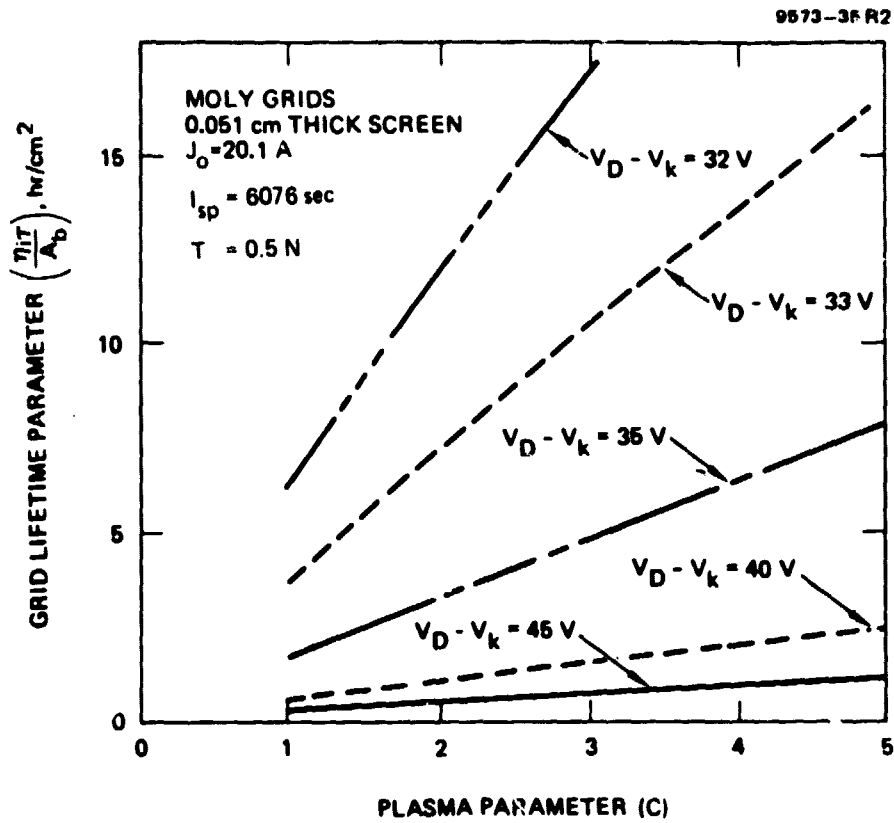


Figure 5. Variation of the grid lifetime parameter as a function of the plasma parameter C. (Argon propellant).

ORIGINAL PAGE 23
OF POOR QUALITY

The quantities S^+ , S^{++} , and S^{+++} are the sputtering yields for singly, doubly, and triply charged ions, and A_b is the beam cross-sectional area. For a beam cross-sectional area of 2000 cm^2 and an ionization efficiency η_i of 0.96, the grid lifetimes are given in the following table along with sputter yields for the triply charged and the corresponding lifetimes for the case where triply charged ions are not considered:

E, eV	S^{+++}	τ^a , hr	τ^b , hr
35	0.09	11,400	12,500
32	0.045	25,000	25,000
^a With triply charged ions			
^b Without triply charged ions			

The above table shows that triply charged xenon ions can have a small effect on grid lifetime when the discharge-keeper voltage difference is 35 V. This effect is eliminated when this voltage is dropped to 32 V or less.

E. MAGNET 3 FIELD CALCULATIONS

It is anticipated that the thruster body, including the magnets and pole-pieces, will have to operate at a relatively high equilibrium temperature. Consequently, the magnet material selected should have superior resistance to demagnetization. Of the magnetic materials available, ALNICO 8 appears to have the best characteristics with regard to demagnetization. In comparison with ALNICO 5, the material used for 30-cm mercury ion thrusters, ALNICO 8 has a better resistance to demagnetization. For example, in reducing the magnet length-to-diameter ratio (L/D) from infinity to a value of 4, ALNICO 8 loses only 15% flux, whereas ALNICO 5 loses 25%. Figure 6 shows a demagnetization curve that is representative of ALNICO 8 material. Assuming a value of 4 for the L/D ratio, a flux density of 0.75 T is considered reasonable. This value will not be sensitive to small changes in L/D .

In a discharge chamber that employs a multipole magnetic confinement configuration, the magnetic circuit is composed of ring-shaped pole-pieces for the wide-wall discharge chamber boundary with short permanent magnets spaced between the rings, as shown schematically in Figure 7. The upstream end of the discharge chamber is composed of concentric cylinder pole-pieces with the permanent magnets spaced around each annulus. The pole-piece thickness is required to be approximately $1/4$ of the magnet diameter to avoid saturation where the magnet contacts the pole-piece. The milled recess that holds the magnet in position does not change this requirement because it is the thickness of the material that surrounds the end of the magnet that is important. It is important that magnets from adjacent "cusps" are not aligned on opposite sides of the pole-pieces. Although this is relatively easy to satisfy on the side walls, magnet placement in the upstream end pole-pieces requires some compromise between achieving a uniform spacing between magnets and separating the point of contact of magnets on opposite sides of the pole-pieces.

The objective of the computations performed here is to determine the number of magnets required to generate the desired confinement fields. The procedure for calculating the magnet requirements has already been

ORIGINAL DRAWING
FOR QUALITY

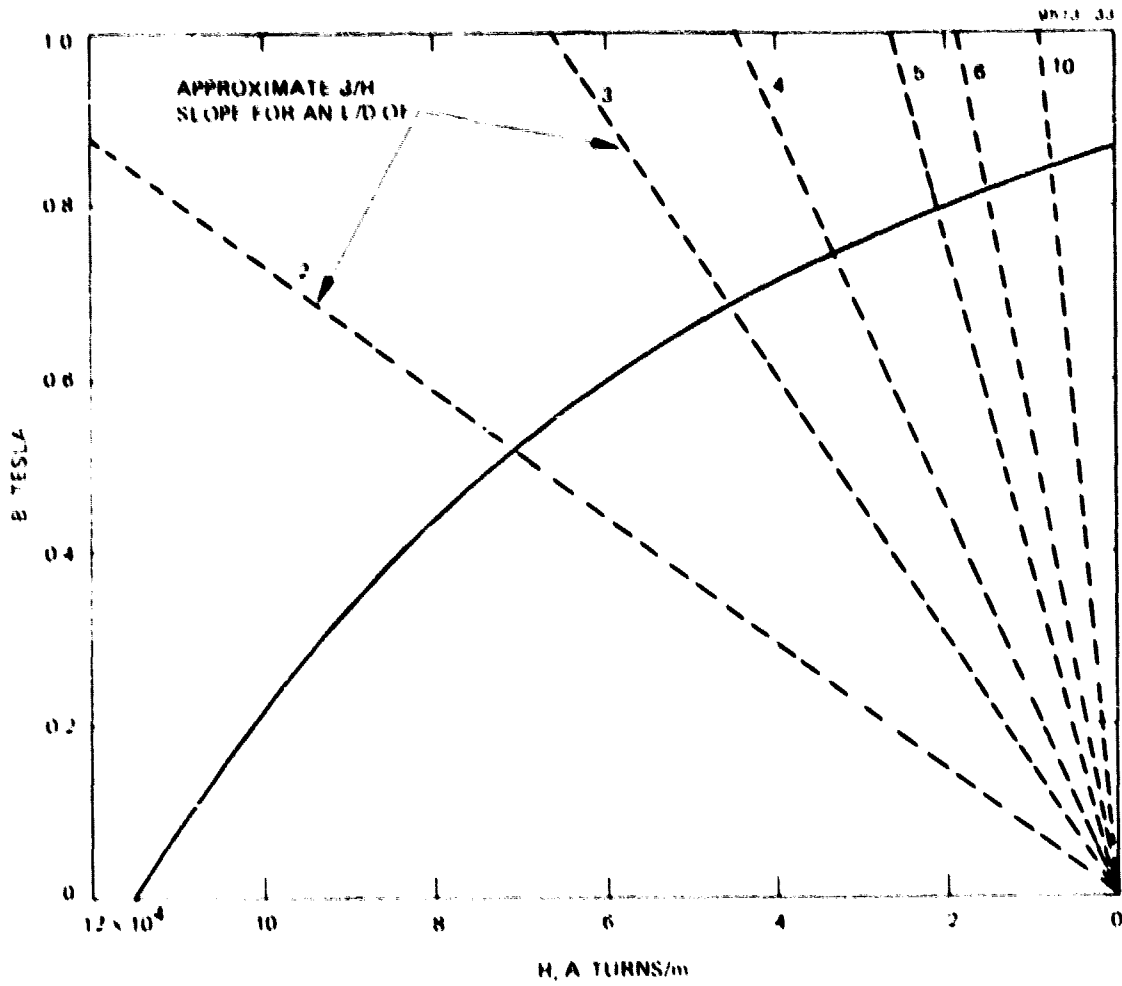


Figure 6. Demagnetization curve for ALNICO 8 (from Crucible Steel Company of America, Publication 5-57).

ORIGINAL PAGE IS
OF POOR QUALITY

9991-1

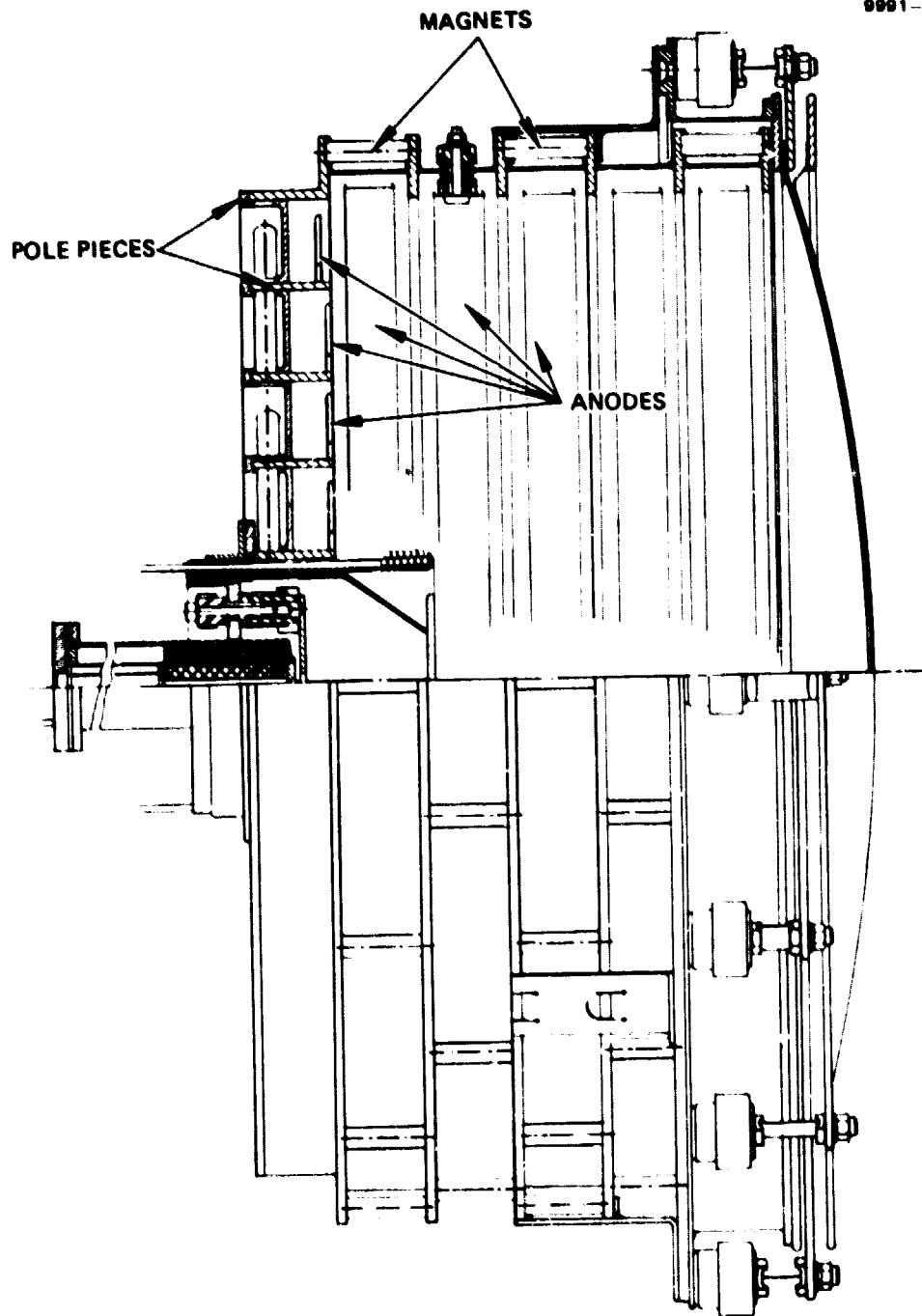


Figure 7. Typical discharge-chamber configuration for multipole magnetic confinement.

developed at Colorado State University and reported in Ref. 4 and 11. As discussed in Ref. 11, the curvature of the side wall pole-pieces is most important. But since the curvature effects for a 30-cm-diameter chamber were found to be small, these effects should be even smaller for the proposed 50-cm chamber. From Ref. 4 (30-cm chamber), the curve describing the magnetic field variation in the pole-piece region can be integrated to show that about 20% of the flux falls within the inner surface of the anode (see Figure 7), with this inner surface assumed to have the same diameter as the inner edge of the pole-piece (as shown in Figure 7). For the proposed 50-cm design, the radial depth of the pole-piece is 3.5 cm, while the axial spacing is 2.7 cm. This depth-to-spacing ratio would be expected to reduce the flux inside the anode inner edge to about 16% of the total, compared to the 20% for the 2.5-cm-deep design of Ref. 4.

For adequate primary electron containment, the flux integral over an anode (toward the axis) should be about 1.5 times the theoretical value given by

$$\int B dx = 6.74 \times 10^{-6} E_e^{1/2} ,$$

where E_e , the primary electron energy, is in eV. For a maximum primary electron energy of 35 eV, the theoretical integral should be about 40×10^{-6} T-m (40 G-cm). Something around 60×10^{-6} T-m should therefore be used in the design. For the low discharge voltages of interest, a low value of this integral is desired to maximize the electron diffusion limit. An integral of 54×10^{-6} T-m (1.4 times the theoretical value) has therefore been selected. The total flux at about a 50-cm diameter (above the anodes) is thus $\pi \times 0.5 \times 54 \times 10^{-6}$ Wb (neglects curvature effect). With this flux, 16% of the total, the total flux should be about 5.3×10^{-4} Wb. The flux through one 6.35 mm (1/4 in.) diameter magnet at the assumed flux density of 0.75 T is $(6.35 \times 10^{-3})^2 (\pi/4) 0.75$, or 2.375×10^{-5} Wb. The number of magnets for one pair of pole-pieces is therefore $5.3 \times 10^{-4} / 2.375 \times 10^{-5} = 22.3$. One should not be

overimpressed with the accuracy of this calculation. A value of 22, though, will be used here for further calculations.

For the upstream end of the discharge chamber, the number of magnets must be varied with the anode diameter.⁴ Note that the inner diameter of the side wall anodes is used, not the mean diameter. The justification for this choice is simply agreement with the experimental fields observed. Using this means of varying magnet number, one finds:

	<u>Anode Diameter</u>	<u>Number of Magnets</u>
Side-wall anodes	49.7 cm	22
End-wall anode	47.0	20.8 → 21
End-wall anode	41.6	18.4 → 18
End-wall anode	36.2	16.0 → 16
End-wall anode	30.8	13.6 → 14
End-wall anode	25.4	11.2 → 11
End-wall anode	20.0	8.9 → 9
End-wall anode	14.6	6.46 → 6-7
End-wall anode	9.2	4.1 → 4

It may be necessary to change the diameters of the upstream pole-pieces slightly, but the method used to select magnet numbers should be clear.

F. THERMAL AND MECHANICAL DESIGN CONSIDERATIONS

The primary concern in the mechanical design for operation at the beam current levels being considered is the rejection of the thermal energy from the discharge and the relatively high operating temperatures that will have to be accommodated by the thruster structure and ion optics assemblies. Our initial analyses have been based on the concept that heat rejection can be obtained by direct radiation from the components heated and that heat pipes or other heat transfer devices will not be required.

In the LeRC/Hughes J-series 30-cm thruster, the thruster structural elements act as a heat shield between the anode and the ground screen, which would require extremely high anode temperatures. A multipole magnetic field geometry is favored for meeting the design goals of this study, and the possibility exists that the discharge chamber can be constructed with a configuration that permits the multipole anodes to radiate directly through the ground screen. Figure 8 shows several typical pole-piece/anode sections. The anodes are formed to have a "T" cross section; the leg projects into the ionization region, and the "cross" of the "T" forms the discharge chamber wall. Electrical isolation of the interior pole-piece (Figure 8) from the discharge chamber (which is at anode potential) is obtained by providing a gap between the interior pole-piece and the exterior pole-piece that holds the magnets.

Previous thermal analysis of LeRC/Hughes 30-cm mercury ion thrusters was based on the assumption that approximately one-half of the discharge power is deposited in (and has to be radiated from) the discharge anode. In a multipole thruster, anode currents should be relatively uniformly distributed around the internal surfaces of the discharge chamber (predominantly to anodes) and consequently it is reasonable to assume that the discharge power will be uniformly radiated from the anode surfaces. The worst-case condition occurs for operation with argon because of the higher beam current and discharge power required. Previous thermal modeling of the 30-cm mercury ion thruster apportioned

ORIGINAL PAGE IS
OF POOR QUALITY

9573-40

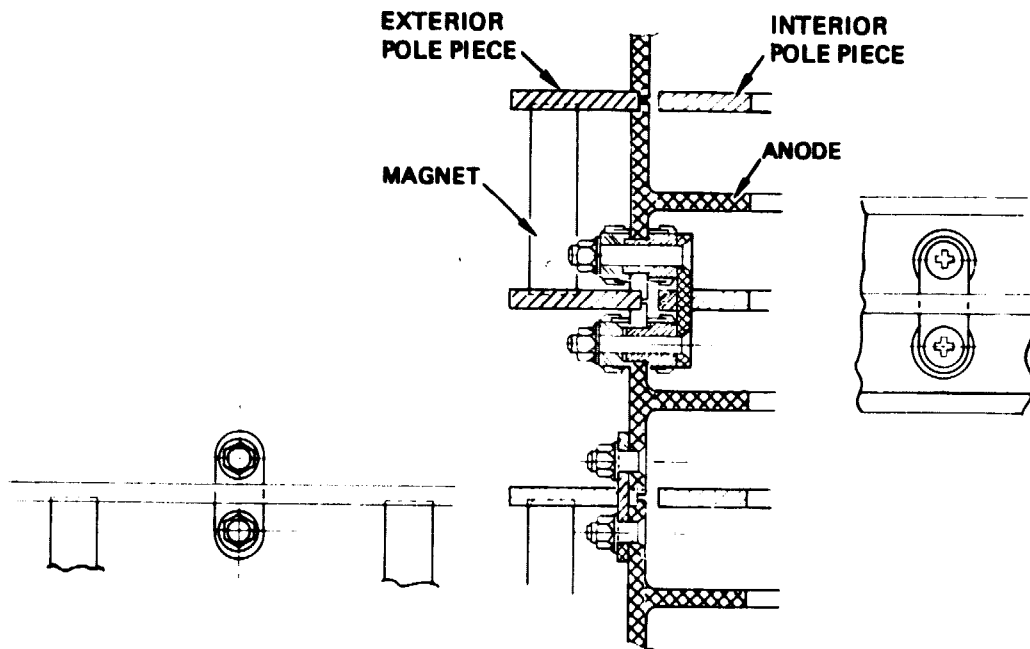


Figure 8. Typical magnet/pole-piece cross section showing anode configuration that provides for direct radiation of thermal input.

the power inputs to the discharge chamber components (approximately) as follows:

Anode	105 J _b
Screen	20 J _b
Backplate	20 J _b
Lost through optics	40 J _b
	<hr/> 185 J _b

If the specific discharge power is apportioned accordingly for the 50-cm multipole thruster, the power input to the components will be:

Anodes	140 J _b
Screen	33 J _b
Lost through optics	33 J _b
	<hr/> 206 J _b

In the multipole thruster, the entire interior surface of the discharge chamber is effectively anode area. For the 50-cm multipole thruster design formulated for argon operation, the anode area is 0.4 m^2 and the power input is 2604 W. Consequently, the steady-state anode temperature will be determined approximately by:

$$T^4 = \frac{1.148 \times 10^{11} \text{°K}}{\epsilon},$$

where ϵ is the emissivity of the anode material. Figure 9 shows the relationship between the steady-state temperature in °C and the emissivity. Since the magnets are in relatively good contact with the anode (thermally), the maximum allowable temperature for the anodes must be the same as for the permanent magnets. Figure 10 shows the thermal characteristics of several magnet materials, and ALNICO 8 is the obvious choice. As shown, 550°C is the maximum allowable temperature, and the objective would be to limit temperature to 450°C or less to have some margin of safety

ORIGINAL PAGE IS
OF POOR QUALITY

9573-41

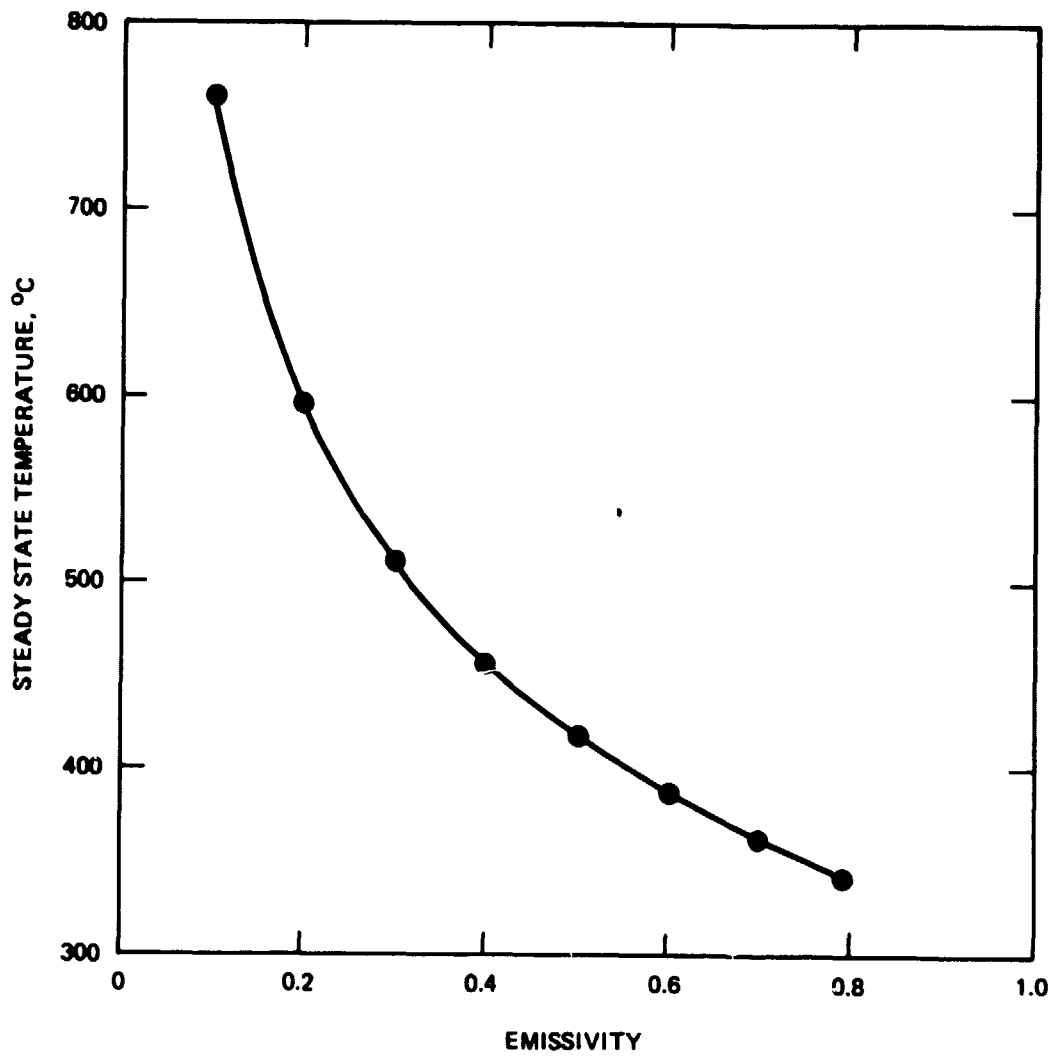


Figure 9. Steady-state temperature attained by radiation cooling as a function of surface emissivity (50-cm thruster, argon propellant).

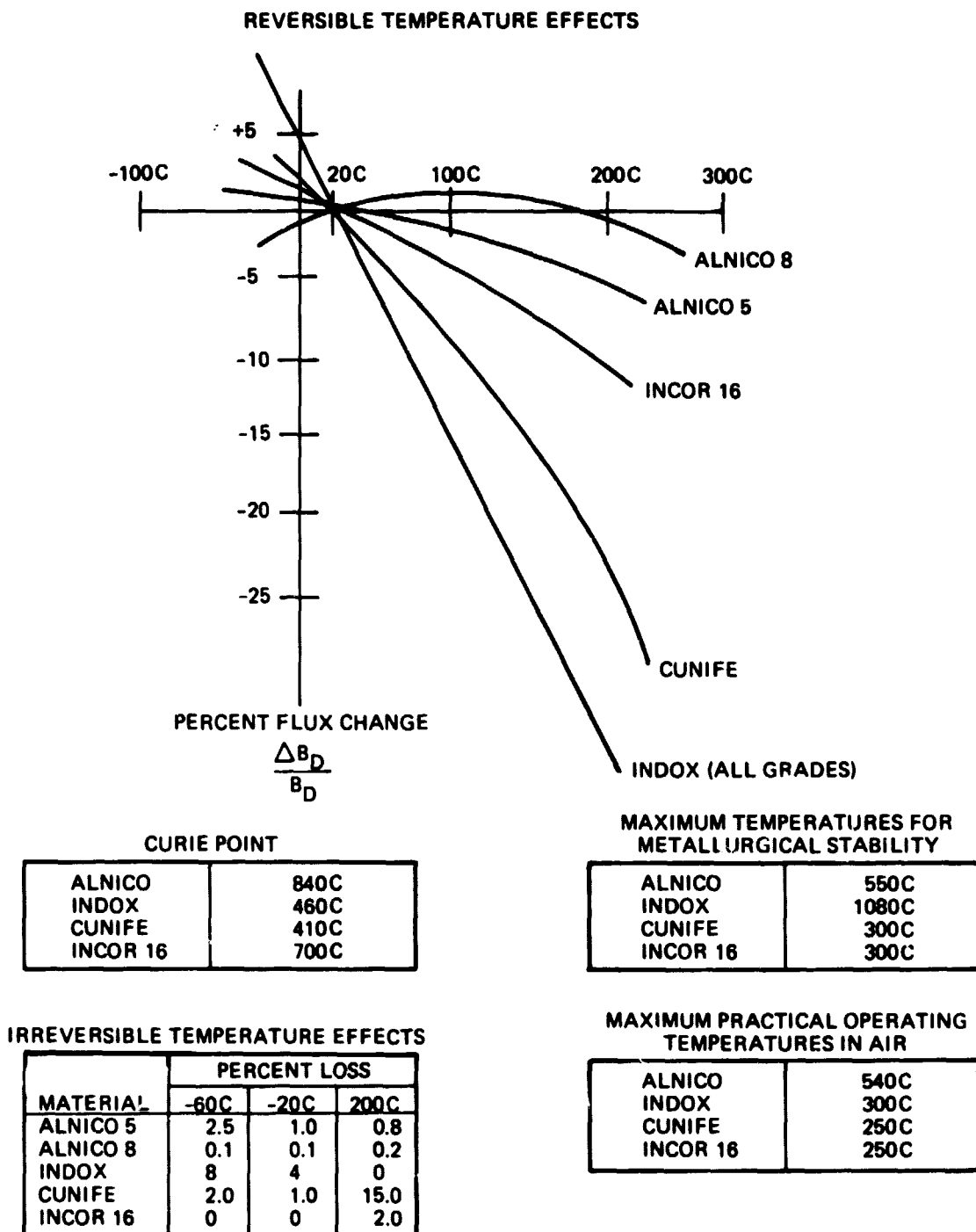


Figure 10. Magnet properties that limit thruster operating temperature.

and also to minimize degradation. Figure 9 shows that an emissivity of 0.4 or greater is required. As seen in Table 5, the emissivities available are on the order of 0.2 for typical materials that could be used to fabricate thruster anodes. Consequently, a thermal-control coating will be necessary to achieve satisfactory temperatures. Two thermal-control coatings are available that provide a minimum emissivity of 0.8 and have been qualified for space applications. The properties of these thermal-control coatings are described below:

Thermal Control Finishes (From HAC "Process Manual")

Specification: HP 4-190

Application: This flat white coating is a high-temperature 650°C resistant, passive thermal-control coating suitable for use in a space environment. The coating provides low solar absorptance and high IR emittance. It can be used on surfaces that are rapidly heated to and exposed to continuous service at 650°C. However, volatile material will be released at the latter temperature. The coating has moderate resistance to UV degradation (i.e., change in solar absorptance). Because of limited testing and 425°C curing temperature, current use of this coating is restricted to nickel-plated metals and CRES steels.

Material: HMS 14-1789

Typical Callout: Paint Per HP 4-190

Specification: HP 4-189

Applications: This flat black, high-temperature (650°C) resistant, passive thermal control coating is suitable for use in a space environment. The coating provides a high solar absorptance and high IR emittance. Because of limited testing and 425°C curing temperature, current use of this coating is restricted to nickel-plated and CRES steels.

Material: HMS 15-1766

Typical Callout: Paint Per HP 4-189

- By using one of these finishes on the external anode and pole-piece surfaces, steady-state temperatures on the order of 350 to 400°C should be achievable.

ORIGINAL PAGE IS
OF POOR QUALITY

Table 5. Properties of Potential Thruster
Fabrication Materials

Thruster Part Candidate Material	$k, \frac{W}{cm^{\circ}C}$	Melting Point, $^{\circ}C$	ϵ_N	$\alpha, ^{\circ}C^{-1}$
Anode				
Aluminum	2.22	646	0.15	23×10^{-6}
Copper	3.91	1083	0.15	17.6×10^{-6}
Beryllium	1.51	1285	0.10	11.5×10^{-6}
Magnesium	0.76	566	0.10	28.8×10^{-6}
Austenitic CRES	0.16	1400	0.27	18.4×10^{-6}
Pole				
1010/1020 steel	0.47	1500	0.27	13.5×10^{-6}
Electrode				
Molybdenum	1.46	2610	0.15	4.9×10^{-6}
Titanium	0.07	1650		9.2×10^{-6}
Magnet				
Alnico				13.0×10^{-6}
where: k is thermal conductivity (in $W/cm^{\circ}C$) ϵ_N is normal total emissivity (dimensionless). α is thermal expansion ($^{\circ}C^{-1}$).				

7174

The conceptual approach for achieving heat rejection and tractable equilibrium temperatures forms the basis for examining the mechanical/structural design of the thruster. At the outset, noncircular, oblong thruster cross sections were investigated to achieve larger beam areas without exceeding the limitations of available molybdenum sheet material (necessary to fabricate the ion-optics grids). The ion-optics subassembly is unquestionably the most critical subassembly with regard to dimensional stability under variations in temperature. The inter-electrode spacing must be maintained at about $0.75 \text{ mm} \pm 0.2 \text{ mm}$ for all temperatures within the thruster operating range. All structural and mechanical design features must be tailored to enable this type of dimensional stability in the ion-optics subassembly. Consequently, the ion-optics subassembly was analyzed extensively (by finite element analysis) to determine which factors have the most effect on inter-electrode spacing.

Structurally, the 30-cm ion-optics and the 50-cm ion-optics are nearly identical. The 50-cm ion-optics was modeled by increasing the radial dimensions of the 30-cm ion-optics EASE-2 structural analysis program. The axial dimensions, and thus the dish depth, were not changed. This resulted in a proportionately shallower dish electrode structure. The radius of curvature of the spherically dished portion was increased from 0.5 m (20 in.) to 1.3 m (51 in.). Both two- and three-grid designs were modeled by this means. Isometric views of the models are shown in Figures 11 and 12.

The thin (0.4 mm) grids of both 30-cm and 50-cm ion-optics subassemblies are attached to thicker (1.9 and 2.5 mm) support rings around their periphery. The screen grid support ring (2.5 mm thick) is then attached to the mounting ring. This mounting ring consists of a thick (5.1 mm) ring forming the base with a thin wall (0.1 mm) short cylindrical section at the inside diameter. The cylindrical section is slotted about two-thirds the distance from the open end towards the base on both sides of 12 attachment points for joining the screen grid support ring to the mounting ring. The slots, located 0.6 cm from the attachment points, form a flat spring column 1.2 cm wide and 2.3 cm high which may

ORIGINAL PAGE IS
OF POOR QUALITY

9573-44

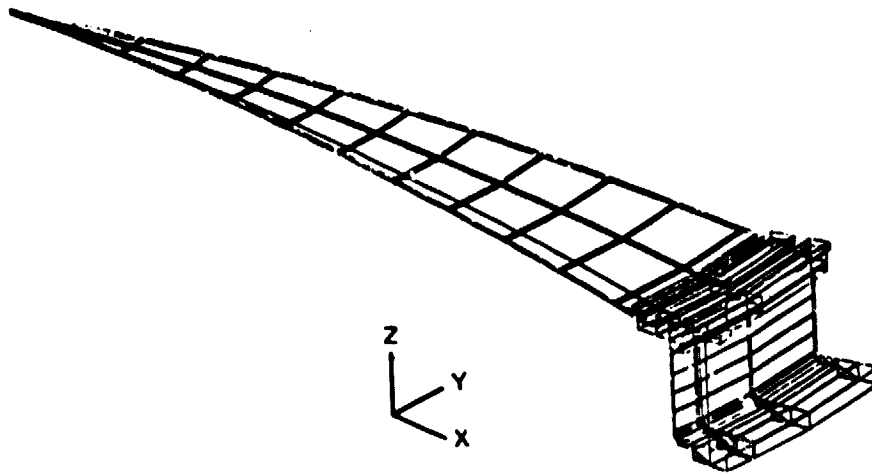


Figure 11. Isometric view of the computer modeling for a 2-grid 50-cm thruster ion-optics assembly.

9573-45

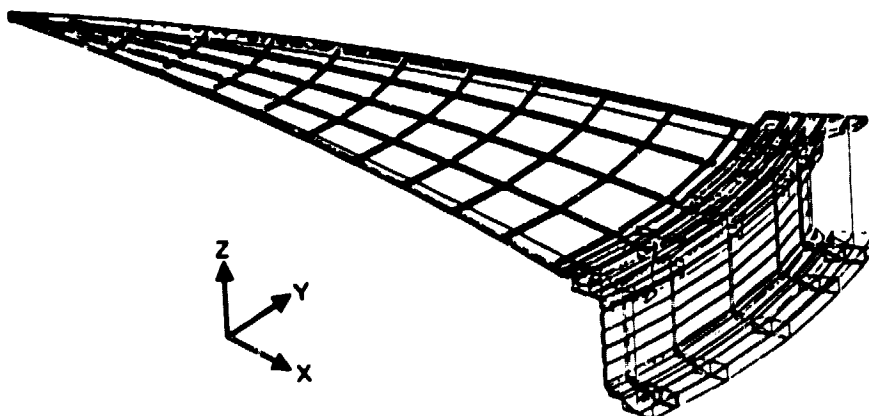


Figure 12. Isometric view of the computer modeling for a 3-grid 50-cm thruster ion-optics assembly.

flex radially and is stiff tangentially through its width. The accel (and for three-grid, the decel) are attached to the base of the mounting ring. They are electrically isolated by alumina insulator assemblies mounted to the base with flat spring assemblies, similar in form and function to the flat spring columns in the mounting ring, between the insulators and the grid support rings.

The support rings and mounting ring are modeled as solid elements and the insulator as pipe elements; the flat spring flex member is modeled to support axial loads only. For the analytic model, the grids are attached to the mounting ring with rigid beams (at the base only), and the slots in the mounting ring next to the shoulder are included in the model. The modeling is three dimensional. A 30° section, shown in Figure 11, was modeled as defined by symmetry of the structure.

The center nodes of the accel and the screen electrodes are allowed to move only in the axial direction. The bottom of the mounting ring is considered to be placed on rollers.

The grid and support rings are molybdenum, the mounting ring is titanium alloy, the insulator is alumina ceramic, and the flex member is stainless steel.

Thermal loading was varied to correspond to temperatures that were measured for operation of the 30-cm thruster at beam currents of 2 A and 6 A, and for a temperature 100°C greater than those for operation at a beam current of 6 A, shown in Figures 13 through 15. In modeling the two-grid ion-optics assembly, temperature data were obtained from NASA LeRC tests for thruster operation at 2 A: temperature data for thruster operation at 6 A were obtained from Hughes Advanced Technology Program. Since the data originated from tests of two-grid ion-optics assemblies, temperature data for three-grid ion-optics assemblies were derived by assuming the accel temperature of the two-grid assembly to be the decel temperature of the three-grid assembly; accel temperature of the three-grid assembly was then assumed to be higher than the screen grid temperature by one-half the differential between the temperatures of the screen and decel grids.

ORIGINAL PAGE IS
OF POOR QUALITY

8998-18 R1

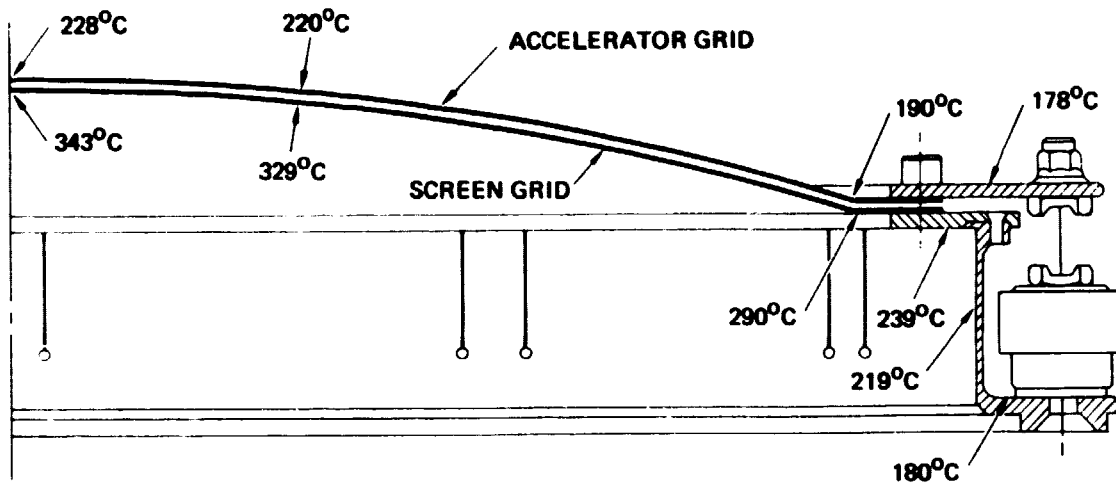


Figure 13. Cross section of the ion accelerator grid assembly for the J-series 30-cm thruster showing temperatures used in stress analysis $J_b = 2$ A.

8996-17 R1

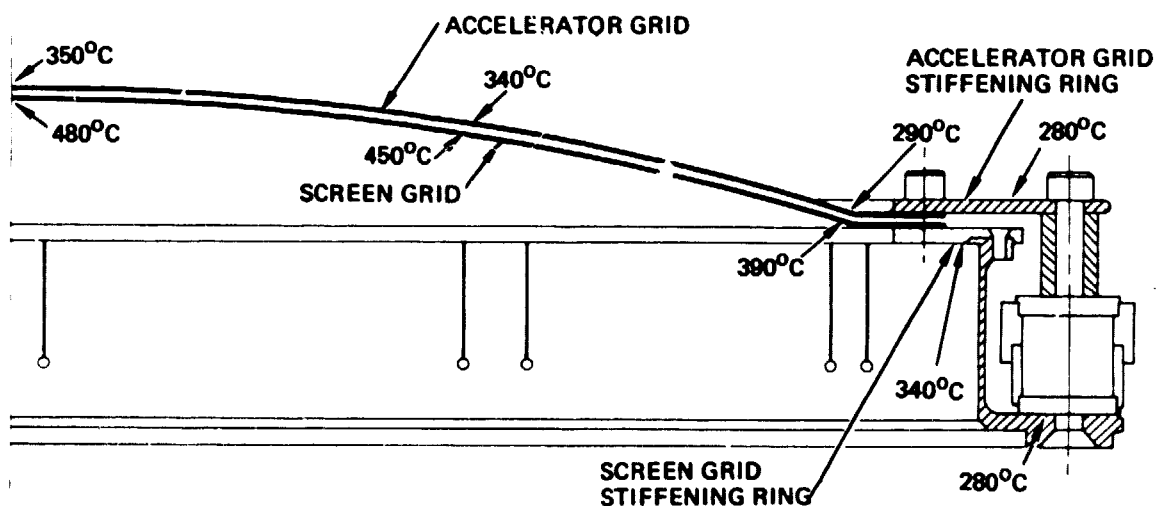


Figure 14. Cross section of the ion accelerator grid assembly showing temperatures representative of 1.4 W/cm^2 thermal input $J_b = 6$ A.

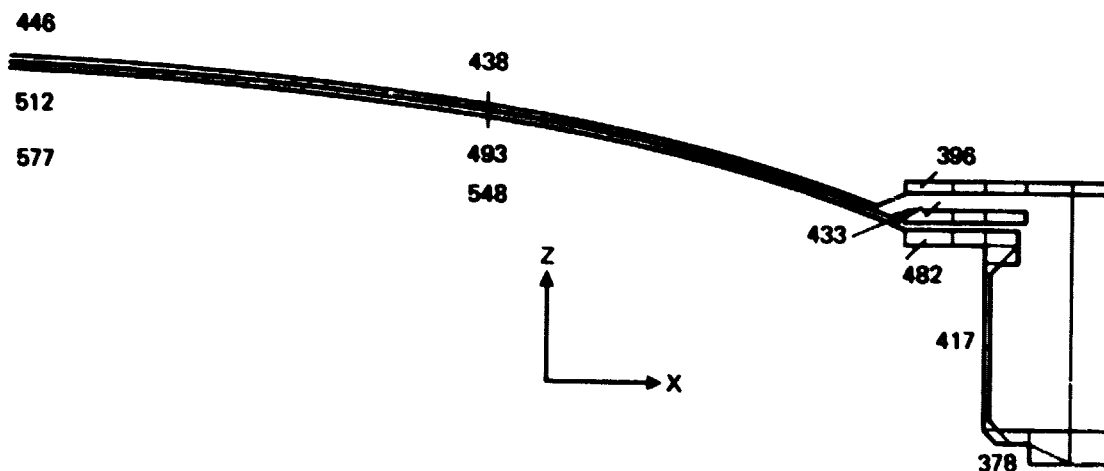


Figure 15. Ion-optics model showing temperatures assumed for condition that operating temperature would be 100°C greater than for $J_b = 6$ A.

The results of these analyses show good stability of all of the electrodes with interelectrode spacing varying only due to thermal expansion. There was no apparent deformation of the electrodes from electrode supporting rings, indicating that the flex members connecting the molybdenum electrode supporting ring to the titanium electrode mounting ring are decoupling the effects of differential thermal expansion between the two rings.

The accel electrode for a 50-cm-wide by 100-cm-long oval thruster was modeled and analyzed. A quadrant of the accel electrode was modeled using the two axes of symmetry as boundaries. Motion at the intersection was limited to axial direction only. The bottom of the mounting ring was mounted on rollers, free to move in two directions but not axially. Flex member supports connected the support ring with the mounting ring. A plane view of the accel electrode model is shown in Figure 16. The temperatures were the same as those for the round electrodes with the temperature at the center of the semicircular end assumed to be constant along the center of the rectangular part of the oval electrode.

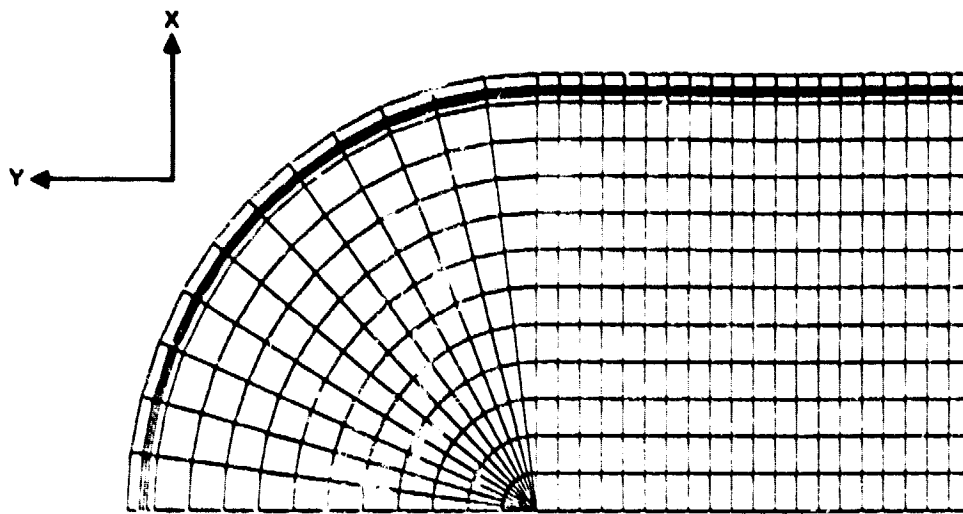


Figure 16. Plan view 50-cm x 100-cm oval accel electrode model.

The result of the analysis for load case 2 (30-cm electrode temperatures at 6 A beam) is shown superimposed on the room-temperature model in Figure 17. The room-temperature model is shown in this figure as broken lines. Thermal displacement of the nodes in the rectangular part of the grid is nonuniform, with the hotter central axis expanding more than the cooler outside edges. This causes the circular quadrant to be distorted such that the point of maximum displacement parallel to the long axis of the electrode is along a radial at 30° from the center of the circular quadrant, not along the long axis as would be expected. Consequently, the symmetrical expansion necessary to preserve electrode aperture alignment cannot be assured.

The quasi-radial lines beyond the outline of the grid nodes are the two ends of the flex members. The outer-most end is the end that is attached to the insulators. The inner ends are attached to the accel stiffening ring. The flex members along the two axes are the least affected by differential thermal expansion between the titanium electrode and molybdenum stiffening rings. The other four flex member supports would have to be able to flex in two directions and carry axial loads

ORIGINAL PAGE IS
OF POOR QUALITY

only. Consequently, non-circular thruster cross sections are not considered to be tractable from an ion optics assembly point of view (at least for large thrusters that are operated at high temperature).

9573-48

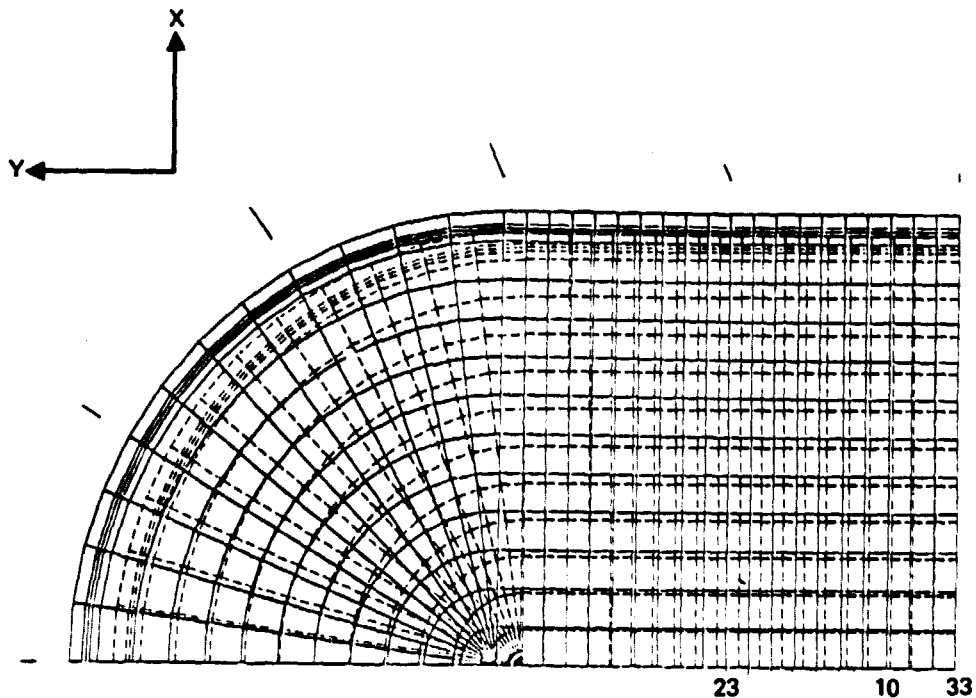


Figure 17. Displacements of model elements in thermal expansion.

SECTION 3

RECOMMENDED CONCEPTUAL DESIGN

The analyses and computations described in the previous section lead to the recommendation of a 50-cm-diameter multipole thruster configured as shown in the layout drawing of Figure 18. The main design specifications and performance characteristics are listed in Table 6. The design features that distinguish this conceptual design from the NASA/Hughes 30-cm mercury ion thruster are listed as follows:

- Modular, multipole magnetic confinement discharge chamber
- Three-electrode ion-optics assembly for high-current, low- I_{sp} operation
- Anode potential support structure to facilitate heat rejection
- Multiple cathodes to build on state-of-the-art hollow-cathode technology
- Plenum-type distributed electron injection with electromagnets for control
- Major subassemblies electrically isolated to enable choice of bias
- Propellant flow controlled with piezoelectric valves
- Thruster assembled from major subassemblies.

The major structural element in this design is the angle cross-section ring at the intersection of the end and the side walls. This ring is fabricated of austenitic stainless steel for its non-magnetic characteristic. The angle cross section supplies the stability required. Not only is it the main structural element, but it also serves as the main propellant plenum and is shown with four main isolators directly feeding into the upstream wall of the ring. The arms of the angle are partially closed by the external magnetic poles of the end and side wall. Two annular slots are provided by the inclusion of the internal corner magnetic pole, which also has an angle cross section. Propellant distribution uniformity will be provided by a fine wire mesh cloth ring

ORIGINAL PAGE IS
OF POOR QUALITY

9573-34R1

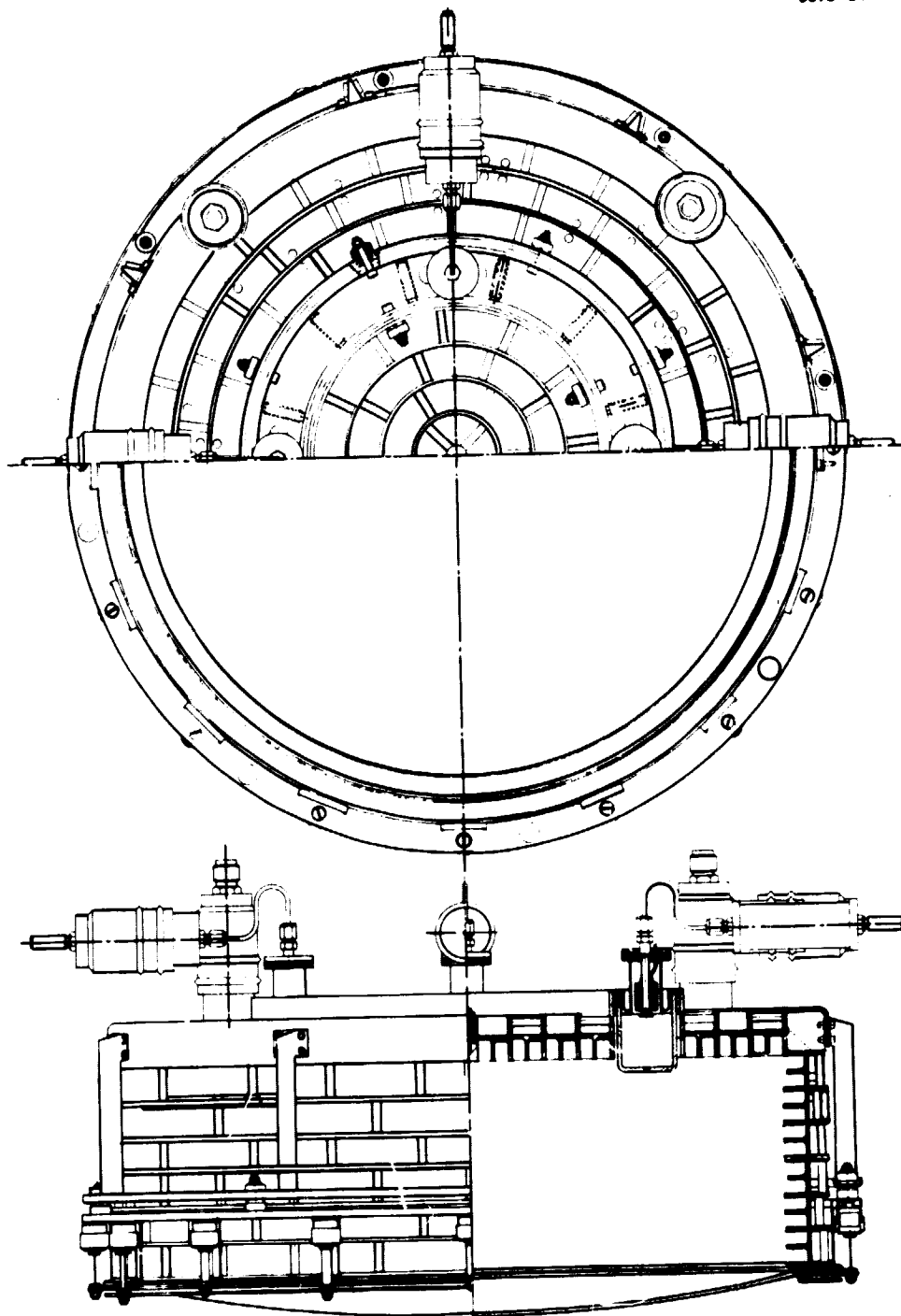


Figure 18. Layout drawing of the proposed thruster diagram.

Table 6. Thruster Design Specifications and Predicted Performance Characteristics

Specification or Characteristic	Design Value	
	Argon Propellant	Xenon Propellant
Specific impulse, sec	6,076	3,530
Thrust, N	0.5	0.5
Beam diameter, cm	50	50
Discharge chamber length, cm	16.2	16.2
Beam voltage, V	932	716
Discharge voltage, V	45	34
Emission current, A	86.5	63.1
Beam current, A	18.9	13.0
Total power input, W	21,500	11,453
Electrical efficiency, %	81.9	81.3
Propellant efficiency, uncorrected, %	93.5	122.6
Thrust correction factor	0.947	0.869
Thruster efficiency, %	68.6	75.2
Screen grid wearout, hr	6,130 ^a	34,000
Specific discharge power, eV/ion	206	165
Total extraction voltage, V	1,550	1,795
Ratio of beam voltage to total voltage	0.6	0.4
Number of cathodes	4	4
Total propellant flow, A, equivalent	20.2	10.6
Cathode propellant flow, each, A, equivalent	2	1.4
Neutralizer propellant flow, A, equivalent	1.5	1.0
Propellant efficiency including neutralizer, %	87.0	112.1
Electrical efficiency including neutralizer, %	80.6	79.6
Thruster efficiency including neutralizer, %	62.9	67.3
^a Can be extended to 24,500 by adding 0.26% (mass) nitrogen to the argon propellant. ^{15,16}		

suspended between the two external magnetic poles aided by baffles which will deflect the incoming propellant stream from the isolators.

The end wall anodes will be attached to the external magnetic pole. The end wall anode will be machined in two rings, separated by the electron plenum, an annular chamber containing the multiple hollow cathode. As shown in Figure 18, the electron plenum is electrically isolated from the anode and cathodes so that the electron plenum can be maintained at keeper potential. For maximum flexibility, the prototype thruster would be constructed so that the cathode, cathode keeper, and the electron plenum can all be isolated from each other, and their potentials can be changed during tests without breaking chamber vacuum or touching the thruster.

The end wall magnetic poles can be easily formed from strips of 1010 to 1020 steel. The external poles will be attached directly to the anode, while the internal poles will be electrically isolated with ceramic insulators. A maximum gap between matching external and internal poles of 0.32 cm will be maintained by locating the external poles in annular slots cut in the upstream surface of the end wall anodes. The poles will be segmented to allow for differential thermal expansion between the copper or stainless-steel anode and the steel poles.

The side wall is modular, consisting of alternating flat steel magnetic pole rings and the cross section anode rings. This construction provides the flexibility to change the chamber length in increments of 2.7 cm, which is the nominal cyclic length for the multipole thruster as developed by the researchers at CSU. Although the analysis described earlier shows that xenon and argon will require different chamber lengths to obtain maximum efficiency, a single discharge chamber length of 16.2 cm is recommended. Chamber length can be varied by adding or removing poles and anodes as determined by testing.

The electrode assembly is supported by sheet metal columns attached to the outer-ring propellant plenum. An intermediate ring with a channel cross section is also shown as a support for the insulation isolating the electrode assembly from the thruster. This intermediate ring and the electrode mounting ring will be fabricated from titanium alloy to minimize the possibility of distorting the electrode mounting ring

due to differential thermal expansion. The electrode mounting ring is a flat ring of approximately 0.63 cm. thickness to present the least profile to the anode. This cross section may not provide sufficient rigidity or stability, which would require the addition of a rim or rims to increase the section modulus. As in the design of the 30-cm mercury thruster, the thruster is composed of major subassemblies for ease in fabrication and to enable refurbishment. The major subassemblies are listed as follows:

- Three-electrode ion optics and support ring
- Outer multipole discharge-chamber boundary and magnets (separate designs for xenon and argon)
- Rear wall multipole discharge-chamber boundary and magnets
- Electron injection plenum with hollow cathodes
- Propellant injection plenum
- Propellant valve and isolator
- Ground screen
- Neutralizer.

A. POWER PROCESSOR REQUIREMENTS

The power processor requirements are shown conceptually in the schematic shown in Figure 19 (note that the power supplies have dual outputs). There are four major power source requirements -- propellant control, discharge, screen/accel, and neutralizer. A power supply has not been included for the electromagnets used to adjust the magnetic field in the electron injection gap because it is thought that permanent magnets will replace the electromagnet after the initial thruster development. The control concept for controlling discharge voltage, V_0 , and for balancing cathode emission is shown in Figure 20. The gas flow through the valve supplying each hollow cathode is controlled in

ORIGINAL PAGE IS
OF POOR QUALITY

9573 3

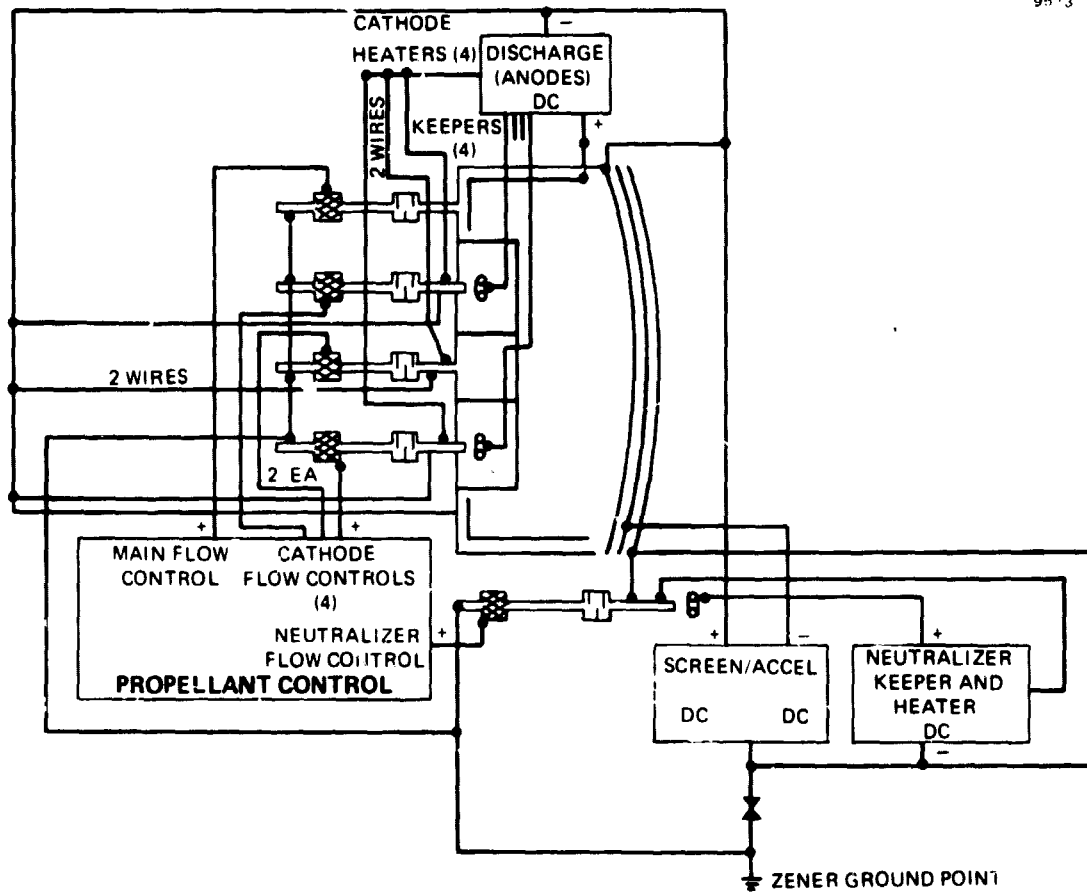


Figure 19. Block diagram showing proposed thruster power processor requirements.

ORIGINAL PAGE IS
OF POOR QUALITY

9455 2H 2

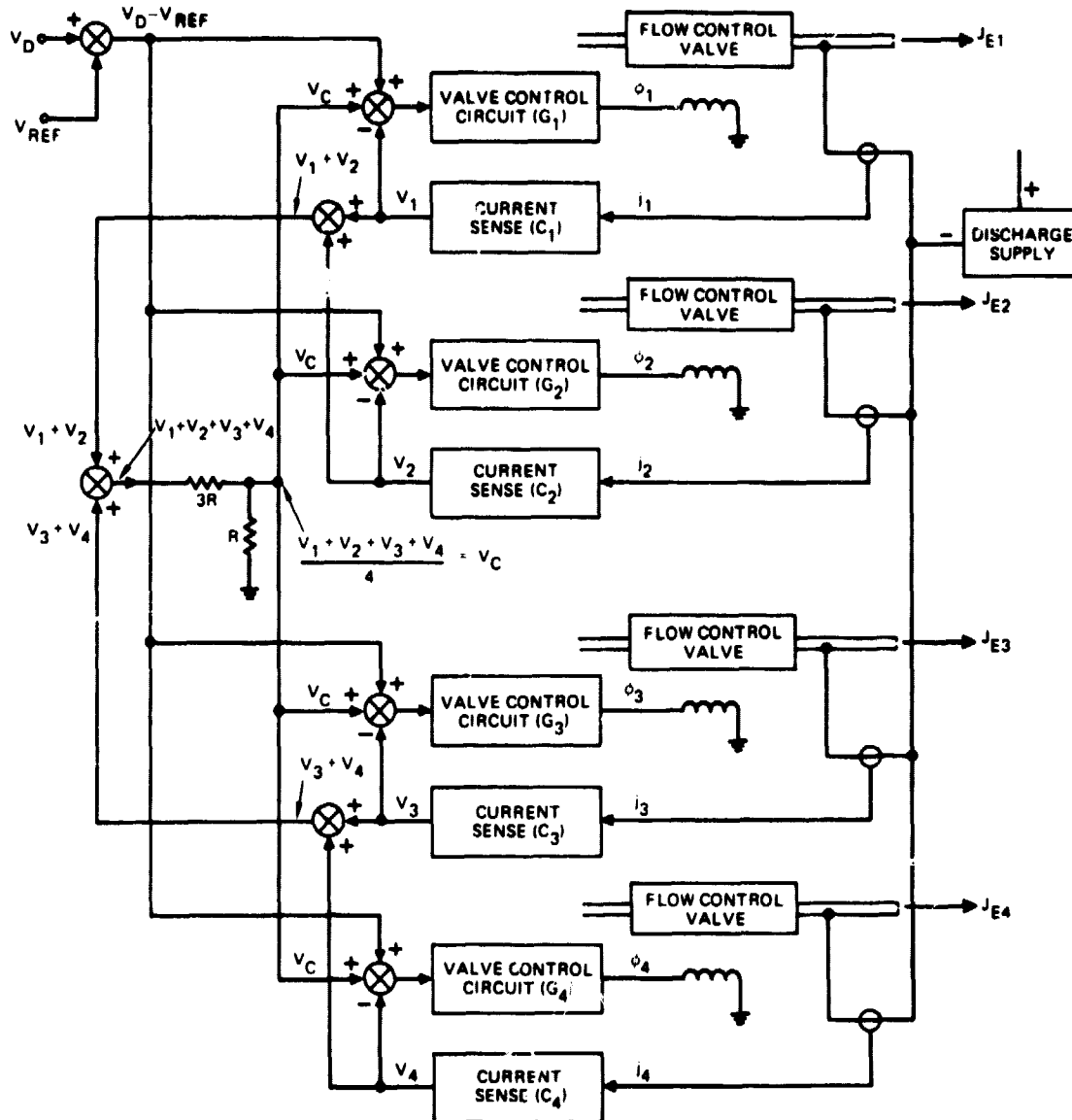


Figure 20. Block diagram showing four-cathode control concept.

proportion to the output of the control circuit, ϕ_1 , according to the expression

$$\phi_1 = (V_D - V_{REF} + V_C - j_1 C_1) G_1 \quad ,$$

where the symbols are defined in Figure 20. The power input to the control circuitry for the piezoelectric valves should be negligible with respect to the other power inputs and has not been included in the efficiencies quoted previously. The nominal power supply requirements for the specifications listed earlier in Table 6 are shown in Table 7. It should be recognized that the voltage and currents listed in Table 7 are not the recommended maximum ratings required for the thruster power supplies. Power supply specifications would have to be determined on the basis of reserve margins that are considered adequate to the applications of the thrust systems in addition to the nominal power levels considered here.

B. TECHNOLOGY AREAS THAT REQUIRE VERIFICATION

The proposed design as described in the previous section is based on systematic extrapolation of analytic models for describing multipole thruster operation. Many of these concepts have been correlated with experimental data; however, the proposed design includes several concepts that have not yet been demonstrated. There are several technology areas that apply to large multipole thrusters in general, and some that are more relevant for use with a specific propellant. Some of the general technology areas that require verification are

- Verification of the uniform discharge plasma conditions that are assumed in the performance analysis
- Demonstration of discharge chamber operation with two or more hollow cathodes
- Balancing of emission between hollow cathodes by control of gas flow
- Determination of operating criteria for long-life operation of hollow cathodes on inert gases

- Verification of dimensional stability of ion optics grids that have longer radius of curvature (than 30-cm thruster grids)
- Verification of dimensional stability at higher operating temperatures (than demonstrated for 30-cm thrusters)
- Demonstration of the effectiveness of thermal control coatings for reducing the operating temperature of an ion thruster
- Verification that the value of $\int B dx$ used enables achievement of the discharge loss parameter assumed in the analysis
- Verification of the magnet requirement specification for pole-piece geometries with an "air gap"
- Development of a valid thermal model.

Many of the items in the list above are not really dependent on thruster size or the propellant used (e.g., multipole cathode operation, grids

Table 7. Power Supply Requirements for the Proposed 50-cm-Diameter Inert Gas Ion Thruster(s)

Power Supply	Nominal Requirements		
	Voltage, V	Current, A	Power, W
Argon propellant			
Screen	900	19.0	17,100
Accel	700	0.05	35
Discharge	45	105.4	4,743
Neutralizer	15	4	60
Xenon propellant			
Screen	700	13	9,100
Accel	1,100	0.03	33
Discharge	34	76	2,584
Neutralizer	15	2	30

7174

with increased radius of curvature) and are being investigated under several other programs.^{12,13,14}

For operation of the proposed thruster design on xenon propellant, several unique technology issues are raised:

- Feasibility of simultaneously achieving the relatively high propellant utilization efficiency predicted theoretically and the relatively low discharge voltage required for limiting multiple ionization
- Dimensional stability of three-grid ion optics assembly (operated at $R = 0.4$)

Operation of the thruster designed for use with argon propellant raises still other technology issues

- Achievement of adequate lifetime with the high discharge voltage required (45 V)
- Feasibility of reducing discharge chamber sputtering by adding nitrogen to the propellant
- Effect of nitrogen propellant additive on hollow cathode operation and lifetime
- Feasibility of achieving long operating lifetime with hollow cathodes operated at greater than 20-A emission current.

Experiments will be required to settle these issues.

SECTION 4

CONCLUSIONS

The design analyses performed during this study have shown that an ion thruster of ~50 cm in diameter will be required to produce a thrust of 0.5 N using xenon or argon as propellants, and operating the thruster at a specific impulse of 3530 sec or 6076 sec (respectively). A multi-pole magnetic confinement discharge chamber was specified because the thruster can (as has been demonstrated experimentally) be scaled to other values of thrust or beam diameter without the requirement for appreciable empirical optimization. Because of this fact, an analytic description of the thruster operating characteristics is considered valid. Achievement of the thruster efficiency goals of 68% for argon and 74% for xenon was determined to be the most demanding of the thruster performance goals (limited by basic physical laws). Achieving this goal requires that the value of the surface-to-volume ratio of the primary electron region of the discharge chamber be adjusted to obtain an acceptable balance between the ion production cost (power) and the resultant propellant efficiency.

Other design challenges were identified as listed below:

- Heat rejection at high power density
- High ion beam current at relatively low net acceleration voltage
- Long operating lifetime at high discharge plasma density (erosion by ion sputtering)
- Dimensional stability under severe thermal load

Engineering innovations have been devised to answer each of these challenges. The heat generated can be radiated by providing good thermal paths through the thruster body to high emissivity surfaces (treated with thermal control coatings). High ion beam currents can be generated at low net acceleration voltages (high permeance) by using three-grid ion optics. Long operating lifetime can be achieved by operating at low discharge voltage and/or adding nitrogen to the propellant to reduce

sputtering rates. Dimensional stability can be achieved by using flexible members in appropriate places to permit predictable elastic deformation of thruster components without appreciably changing critical relative dimensions (such as interelectrode spacing). A circular thruster (ion beam) cross section was found to be necessary for ensuring predictable elastic deformation under severe thermal loads.

The conceptual design that was formulated includes several design features that require experimental verification. The more important of the untested design approaches are listed below:

- Achievement of dimensional stability of dished ion optics grids that have a 1.3-m radius of curvature
- Provision of a satisfactory magnetic field distribution in the anode/pole-piece region when an "air gap" is introduced into the pole-piece magnetic circuit
- Achievement of uniform discharge plasma conditions by operating the thruster with multiple cathodes (balancing current between cathodes)
- Feasibility of reducing the discharge chamber sputtering by adding nitrogen to the propellant
- Feasibility of achieving enhanced thermal rejection through use of thermal control coatings.

The design features listed above are considered to be reasonable extrapolations on exploratory work in progress and, therefore, are not great developmental risks. Assuming that the engineering details for these design innovations can be successfully implemented, the resultant thruster will fulfill the design goals set forth under this contract (exclusive of the neutralizer). Using state-of-the-art technology for hollow cathodes operated on inert gases to predict neutralizer propellant requirements leads to a severe performance penalty; however, an extrapolation of achievable performance improvements would be pure conjecture at this time. Consequently, detailed design specifications for the neutralizers have been left as an open item under this study. Similarly, propellant electrical isolators and gas control were considered in concept only.

At the outset, and early in the study, the contractual goals seemed unattainable within reasonable extrapolations on proven state-of-the-art technology and analyses. It now appears that the conceptual thruster design that has evolved during this study can be developed to meet or exceed these goals without the requirement for any major technological "breakthroughs."

REFERENCES

1. H.R. Kaufman, "Experimental Investigation of Argon and Xenon Ion Sources," Annual Report, CR-134845, Colorado State University, June 1975.
2. H.R. Kaufman, "Inert Gas Thrusters," Annual Report, CR-135100, Colorado State University, July 1976.
3. L.A. Rehn, "Argon Hollow Cathode," NASA CR-135102. Thesis for Grant NSG-3011, November 1976.
4. H.R. Kaufman, "Industrial Ion Source Technology," NSG-3086, NASA CR-135149, November 1976.
5. H.R. Kaufman, "Inert Gas Thrusters," NSG 3011, CR-135226, Colorado State University, July 1977.
6. G.C. Isaacson, "Multipole Gas Thruster Design," NASA CR-135101, for Grant NSG-3011, June 1977.
7. H.R. Kaufman and P.J. Wilbur, "Scaling of Mercury and Gaseous Propellant Ion Thrusters to Large Sizes," AIAA 78-667. Presented at AIAA 13th International Electric Propellant Conference, San Diego, California, April 1978.
8. L. Rehn and H.R. Kaufman, "Correlation of Inert Gas Hollow Cathode Performance," AIAA 78-707, Colorado State University. Presented at AIAA 13th Electric Propellant Conference, San Diego, California, April 1978.
9. H.R. Kaufman, "Industrial Ion Source Technology," NSG-3086, CR-135353, November 1977.
10. P.T. Wilbur and H.R. Kaufman, "Scaling Relationships for Mercury and Gaseous Propellant Ion Thrusters," AIAA Paper 78-667, April 1978.
11. H.R. Kaufman, "Inert Gas Thrusters," NSG 3011, NASA CR-159527, Colorado State University, 1978.
12. H.R. Kaufman and R.S. Robinson, "Plasma Processes in Inert Gas Thrusters," Paper 79-2055, Princeton University, AIAA/DGLR 14th Electric Propulsion Conference, November 1979.
13. G.R. Longhurst and P.J. Wilbur, "Plasma Property and Performance Prediction for Mercury Ion Thrusters," Paper No. 79-2054, presented at Princeton/AIAA/DGLR 14th Electric Propulsion Conference, Princeton, NJ, November 1979.

14. J.R. Brophy and P.J. Wilbur, "Electron Diffusion through the Baffle Aperture of a Hollow-Cathode Thruster," Paper No. 79-2060, presented at Princeton/AIAA/DGLR 14th Electric Propulsion Conference, Princeton, NJ, November 1979.
15. P.J. Wilbur, "A Model for Nitrogen Chemisorption in Ion Thrusters," Paper No. 79-2062, presented at Princeton/AIAA/DGLR 14th Electric Propulsion Conference, Princeton, NJ, November 1979.
16. M.A. Mantenieks and V.K. Rawlin, "Sputtering in Mercury Ion Thrusters," Paper No. 79-2061, presented at Princeton/AIAA/DGLR 14th Electric Propulsion Conference, Princeton, NJ, November 1979.

APPENDIX A

THRUSTER PERFORMANCE CHARACTERIZATION

Optimum discharge-chamber performance is normally obtained near the "knee" of the discharge-chamber performance curve. This is because operation at higher discharge losses will substantially increase the power loss for a much smaller increase in utilization. Conversely, operation at lower discharge losses will decrease propellant utilization more than the power loss will be decreased. The exact point near the knee that will prove optimum for a given set of thruster operating specifications will depend on the required operating conditions. To simplify the iteration procedure, however, a single knee point will be used for this calculation. The error associated with this assumption should be less than the uncertainty in the discharge-chamber performance, when the latter is projected from a limited number of tests. For ease of calculation and rapid hardware development, the multipole type of discharge chamber was assumed.

Using earlier correlations obtained with argon and xenon,^{A-1} together with the screen open-area fraction of 0.65 for the ion optics assumed, the knee discharge losses (eV/ion) used here are

$$E = 73 (A_p/A_b) (Ar) \quad (A.1a)$$

$$E = 67 (A_p/A_b) (Xe) . \quad (A.1b)$$

The corresponding neutral losses (A-equiv.) are

$$J_o (1 - \eta_i) = 3.4 A_o / (V_p/A_p) (Ar) \quad (A.2a)$$

$$J_o (1 - \eta_i) = 0.41 A_o / (V_p/A_p) (Xe) , \quad (A.2b)$$

where A_o is the effective open area ($\phi_a A_b$) of the ion optics (m^2), and V_p and A_p are the volume and outside area of the primary electron region (m^3 and m^2). The effective open area, both here and in ion optics

designs with accel holes significantly smaller than the screen holes, is the accelerator open area times the Clausing factor for the length-to-diameter ratio of the accelerator holes used. Since a simple cylindrical design was assumed for the discharge chamber, the primary electron region was assumed to be the cylinder that would just fit within the anodes, pole pieces, and screen grid. A simpler expression was sufficient for the correlation because only a single chamber diameter and optics design were used.

A convenient starting point for the ion optics design is the screen hole diameter. In general, the smaller the screen holes, the larger the current capacity of the ion optics. Several experimental studies have shown, though, that screen holes smaller than about 2 mm in diameter depart substantially from expected space-charge-flow performance. A diameter of 1.9 mm is commonly used and is assumed here to be the minimum diameter.

The choice of accelerator hole size is a compromise between the current-carrying capacity and neutral loss, both of which increase as hole diameter is increased. To a first approximation, these variations are not dependent on the use of a two- or three-grid ion optics design or on the value of net-to-total voltage ratio, R , used. The beam current capacity is proportional to the normalized perveance (N.P.), while the neutral loss is proportional to the effective open area of the accelerator grid. A performance index can therefore be obtained by dividing the normalized perveance by the effective open area of a single aperture. The effective open area also includes a Clausing factor, so a typical ratio of accel thickness to screen hole diameter of 0.2 is assumed. Expressing the accel hole area as a fraction of screen hole area, the performance index is $N.P. / (d_a/d_s)^2 K_c$. Using two-grid experimental data for an R of 0.7, a plot of this index against accel-to-screen hole diameter ratio, d_a/d_s , is shown in Figure A-1. The normalized perveance used was for mercury propellant, but the d_a/d_s value for the maximum would be the same for other propellants. The significant point about the data shown in Figure A-1 is the maximum near the data point

ORIGINAL PAGE IS
OF POOR QUALITY

for $d_a/d_s = 0.64$. More detailed ion optics data would probably give a slightly different value. In addition, the exact d_a/d_s would shift slightly for different operating conditions. For the purposes of this study, though, a value of $d_a/d_s = 0.64$ should be sufficiently precise.

For the maximum span-to-gap ratio, hence maximum thruster diameter, some form of ion optics using dished molybdenum grids will be assumed. As described in a preliminary study of large thrusters, a maximum span-to-gap ratio of about 600:1 can be assumed for this approach. This maximum span-to-gap ratio is essentially determined by thermal/mechanical effects and will undoubtedly vary somewhat with size, power level, and the specific mechanical design used. As with other assumptions, however, the use of a single limit value is appropriate for this analysis.

Another ion-optic parameter that must be selected is grid spacing relative to screen hole diameter, ℓ_g/d_s . We are not just interested in physically large thrusters: we also want them to have high performance. For high current and power densities, it is necessary that the grid spacing be small. As shown in Figure A-2, the benefits of small ℓ_g 's are limited for $\ell_g/d_s \ll 1$. The best simple parameter for acceleration distance between a screen grid and an accelerator grid is the effective acceleration distance, ℓ_e , defined by the equation given in the sketch. The ratio ℓ_e/d_s decreases with decreasing ℓ_g/d_s , but the decrease becomes very small as ℓ_g/d_s approaches zero. A tradeoff is indicated because a small ℓ_e/d_s is desirable for high current density, but the tolerance and electrical breakdown problems become critical as ℓ_g/d_s approaches zero.

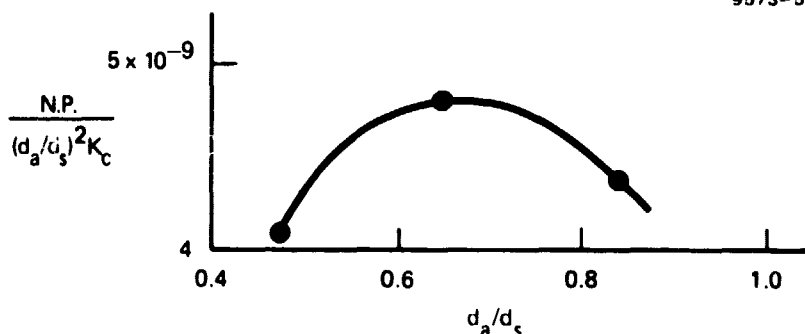


Figure A-1. Ion optics performance index as a function of d_a/d_s .

9573-6

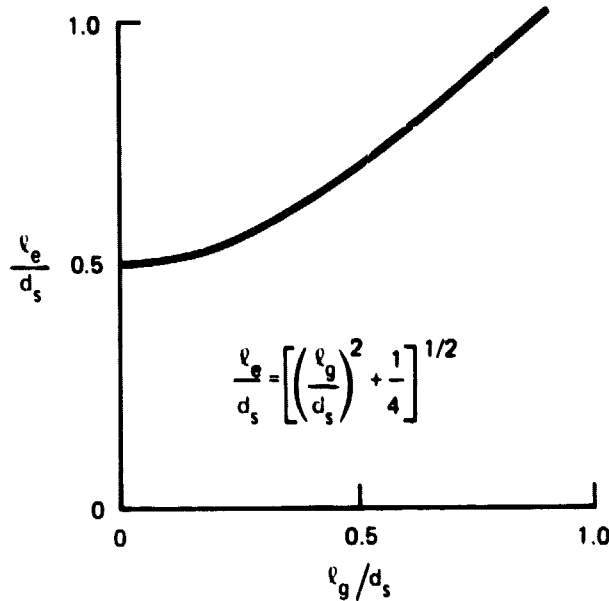


Figure A-2.
Normalized acceleration
length as a function of nor-
malized interelectrode
spacing.

As a partially arbitrary assumption, a value of 0.5 was selected for $\frac{l_g}{d_s}$. The argument given above for a small $\frac{l_g}{d_s}$ is most persuasive for low specific impulses, where the maximum electric fields are not a limit, even though the smallest permissible screen hole diameter is used. There is, though, a thermal expansion argument that is valid at all specific impulses. For the maximum span-to-gap ratio, thermal expansion would be a larger fraction of screen-hole diameter if a larger value of $\frac{l_g}{d_s}$ were used. Specific designs (particularly high specific impulses at less than maximum span-to-gap ratio) may benefit from larger values of $\frac{l_g}{d_s}$, but the value selected appears to be a reasonable choice for all designs.

For ion-beam calculations, a normalized perveance of 3×10^{-9} (Ar) appears to be a reasonable value. That is high, but not so high as to risk serious accelerator impingement. For xenon, the normalized perveance was corrected by the square root of atomic mass. Backstreaming calculations for the assumed geometry indicate a maximum R of 0.8, while the minimum R was assumed for two grids to be 0.7 (for 15° half angle) and for three grids to be 0.17 (same 15° half angle, $l_g = l_d$).

For three grids, the decelerator grid should also have holes about 0.83 times the screen hole diameter. The decelerator grid spacing was assumed equal to the accelerator grid spacing because, for the largest thrusters, both spacings should be subject to roughly the same limit in span-to-gap ratio.

For minimum screen hole diameter, then, the minimum gap is 0.5×1.9 , or 0.95 mm. A safe limit on maximum electric field appears to be 2000 V/mm, although further breakdown data with operating thrusters may show that this is too small for the smaller gaps. This 2000 V/mm limit was used for all calculations made here. Then for the smallest grid gap, a total voltage of 1900 V ($0.95 \text{ mm} \times 2000 \text{ V/mm}$) is permissible. The gap can be increased to above the 0.95 mm value if required to (1) maintain the permissible span-to-gap ratio of 600:1 or (2) reduce the screen-accel electric field to 2000 V/mm.

For the preliminary calculations shown here, neither an off-axis thrust loss nor a neutralizer propellant loss was included, and the only power loss was assumed due to the discharge.

To avoid an unnecessary iteration, a performance calculation at a given specific impulse was started by assuming a propellant utilization. The net voltage necessary to obtain the required average propellant velocity was then calculated; then the complete ion optics performance consistent with span-to-gap and electric field limits was calculated. Next, the discharge chamber length (or depth) required for the assumed utilization was calculated. (The neutral loss is actually the parameter of interest for this length and is available from the assumed utilization and the calculated beam current. It should be noted that it is possible to initially assume a propellant utilization that is too high to be obtained by any discharge chamber length.) With chamber length known, the discharge loss and thruster efficiency were calculated.

Double-ion production was considered in this analysis, although not in detail. From the information presented earlier in this report, it was assumed that low discharge voltages would reduce double-ion production to a level consistent with both long life and high performance. The present understanding of electron diffusion is also assumed to be sufficient to permit reaching the necessary low discharge voltages.

A. CALCULATED PERFORMANCE

Calculated performance data are shown for argon propellant in Figures A-3 through A-10 and for xenon propellant in Figures A-11 through A-16. These data are also shown in Tables A-1 through A-14.

In Figures A-3 and A-10, performance is shown over a range of specific impulse for a thruster with a 0.5-m beam diameter. At each specific impulse, the propellant utilization was iterated to the nearest 0.001 to maximize thruster efficiency. The beam diameter of 0.5 m is large, but not so large that the minimum grid spacing is increased above 0.95 mm due to span-to-gap ratio (d_b/ℓ_g). The maximum efficiency also required that the ion optics for each specific impulse be optimized, although this optimization did not require any iteration.

Optimized in this manner, the data in Figures A-3 and A-10 show the minimum net-to-total voltage ratio, R , at low specific impulses, the maximum of 0.8 at high specific impulses, and intermediate values in between. At low specific impulses (below about 2000 sec for Ar and below about 3000 sec for Xe), the minimum spacing of 0.95 mm is used, but the screen-accel electric field is less than the maximum of 2000 V/mm. The use of the minimum permissible R is necessary to obtain maximum beam current which, in view of neutral-loss theory, is required to obtain maximum utilization and thruster efficiencies.

In the intermediate specific impulse range (about 3000 to 7770 sec for Ar and about 2000 to 4620 sec for Xe), the maximum beam current is obtained by keeping the minimum gap dictated by the span-to-gap ratio and decreasing the total voltage to agree with the electric field limit. This conclusion can be shown by Child's law, with current varying as $\Delta V_t^{3/2}/\ell_e^2$. Using a gap larger than the minimum while maintaining maximum electric field will result in ℓ_e^2 increasing more than $\Delta V_t^{3/2}$, thus decreasing maximum current. With the gap fixed at the minimum and the electric field at the maximum, the extracted ion current is also a constant in this specific impulse range (see Figures A-3(b) and A-10(b)).

In the high specific impulse range (above about 7770 sec for Ar and about 4620 sec for Xe), the net voltage is so high that R will increase

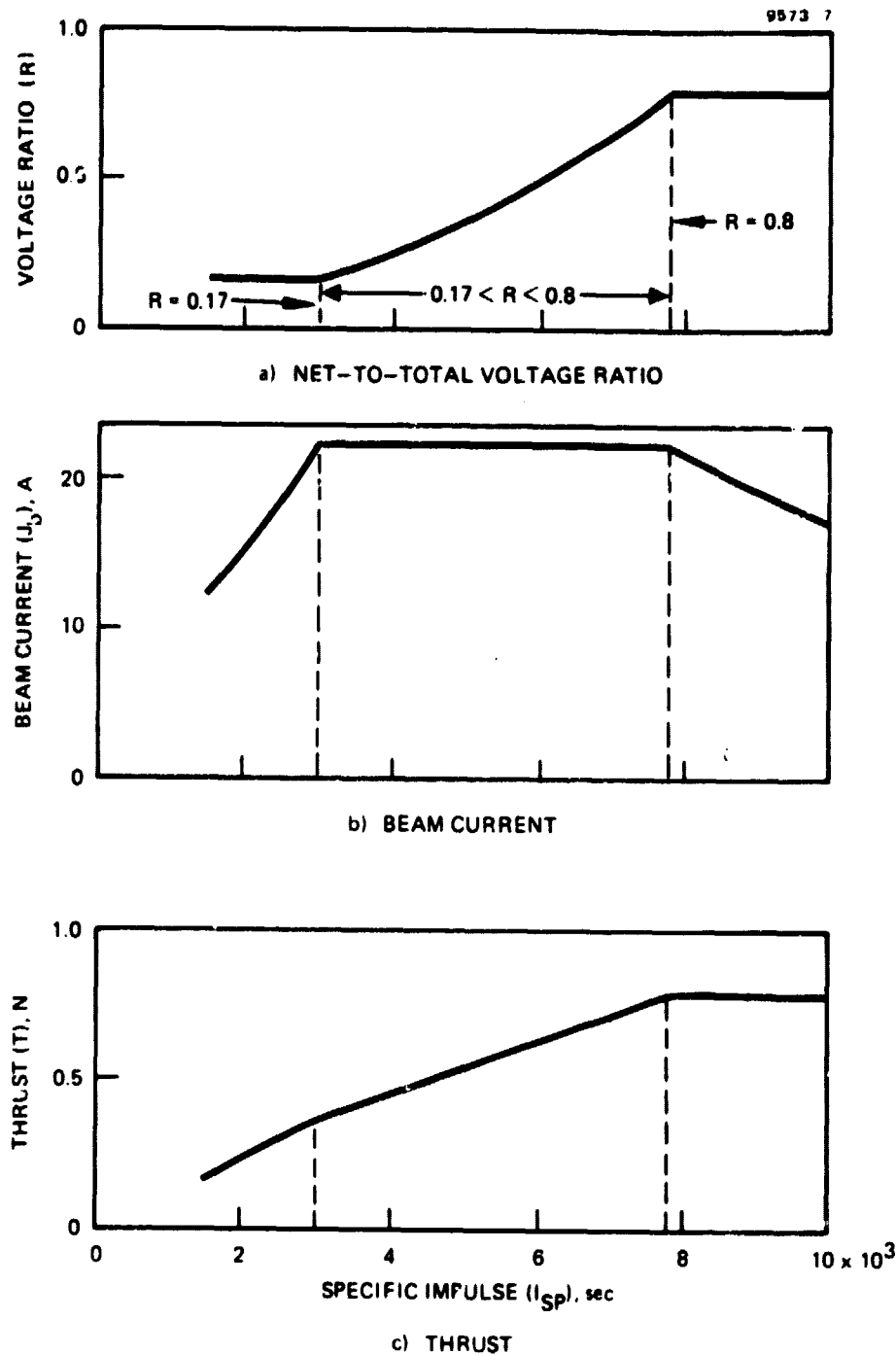


Figure A-3. Effect of specific impulse on performance. Propellant, argon; beam diameter, 0.5 m; propellant utilization, optimized for maximum thruster efficiency.

ORIGINAL PAGE IS
OF POOR QUALITY

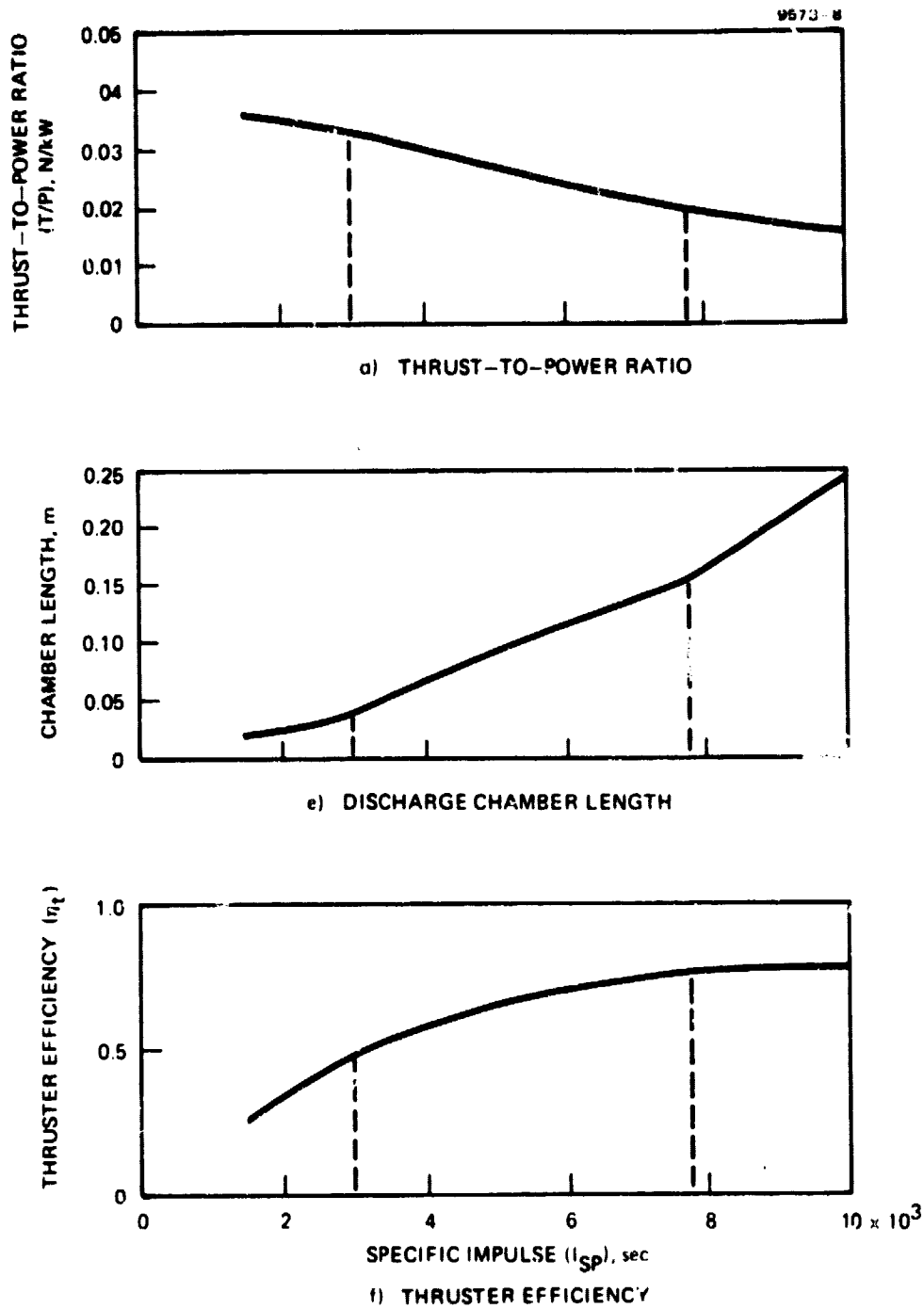


Figure A-3. Continued.

ORIGINAL PAGE IS
OF POOR QUALITY

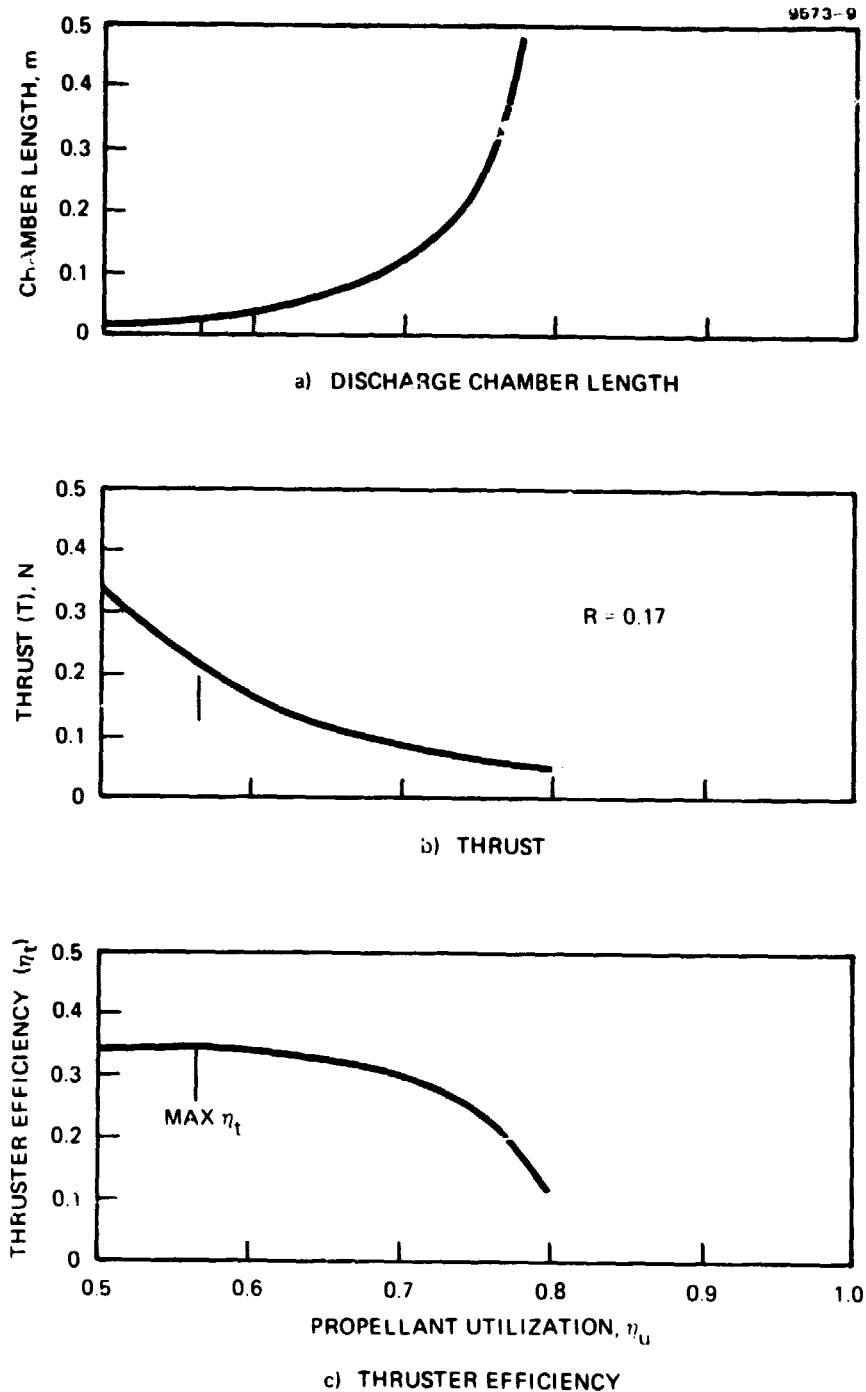


Figure A-4. Effect of propellant utilization on performance. Propellant, argon; beam diameter, 0.5 m; specific impulse, 2000 sec.

ORIGINAL PAGE IS
OF POOR QUALITY

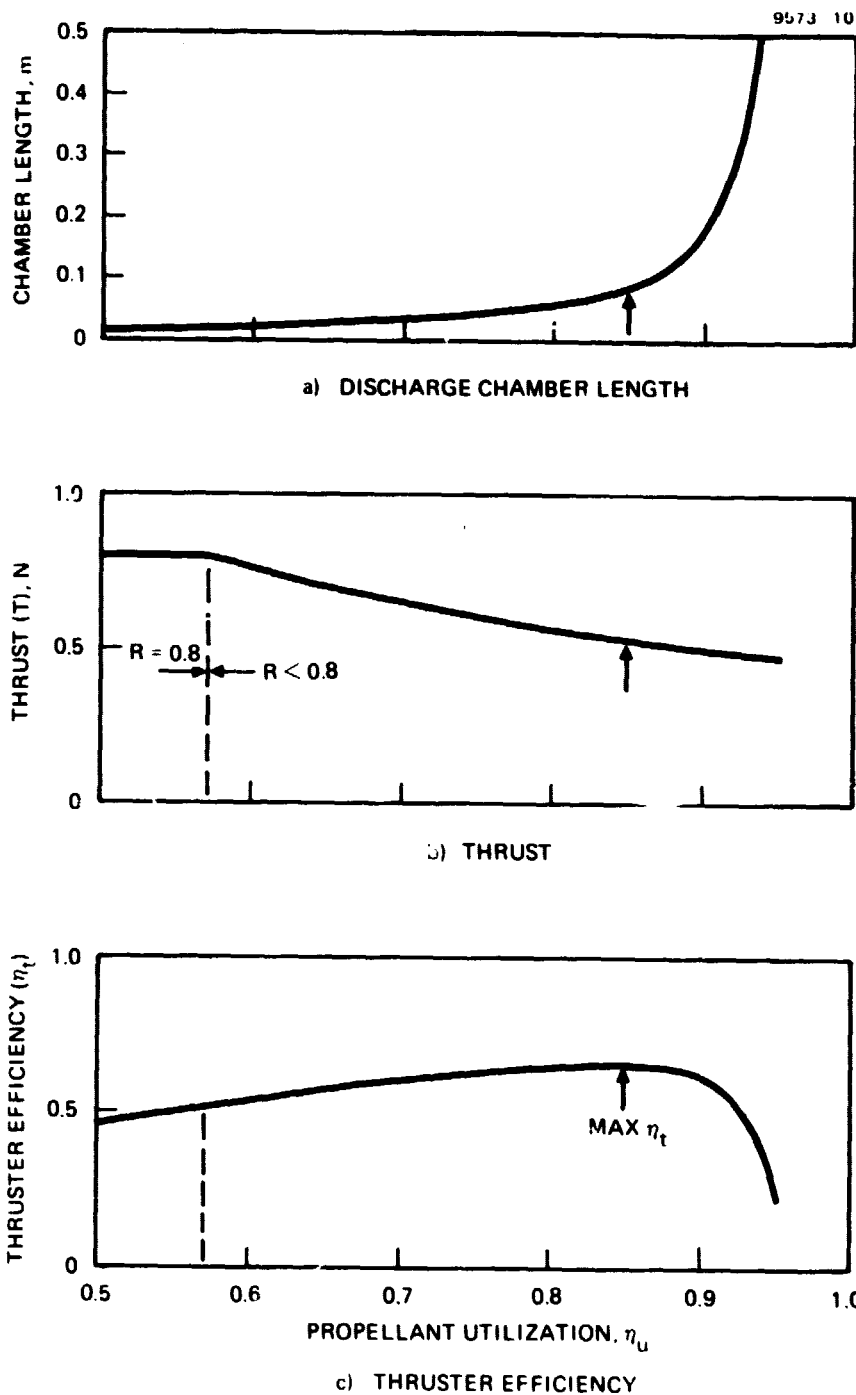


Figure A-5. Effect of propellant utilization on performance. Propellant, argon; beam diameter, 0.5 m; specific impulse, 5000 sec.

9573-11

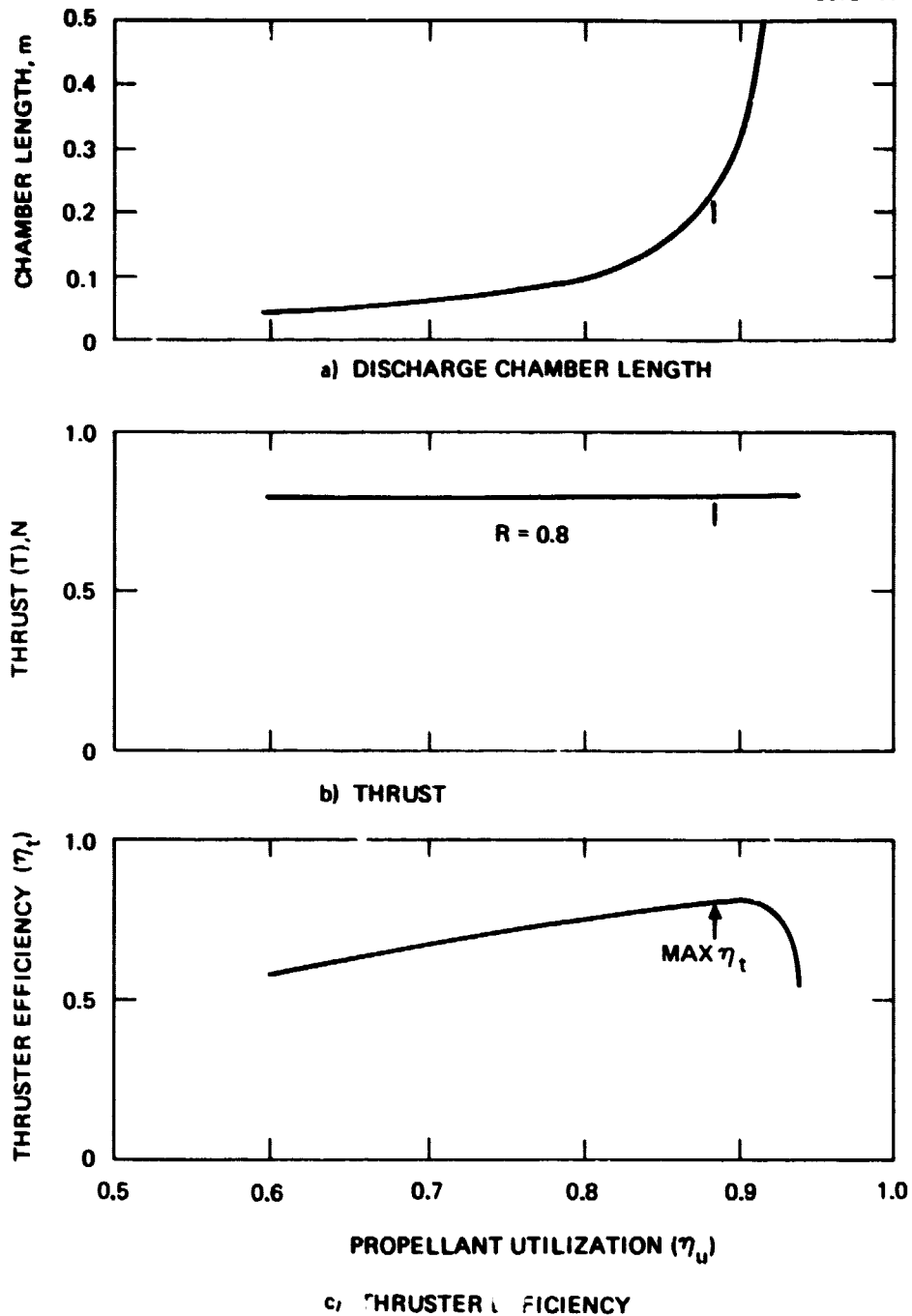


Figure A-6. Effect of propellant utilization on performance. Propellant, argon; beam diameter, 0.5 m; specific impulse, 10,000 sec.

ORIGINAL PAGE IS
OF POOR QUALITY

9573-12

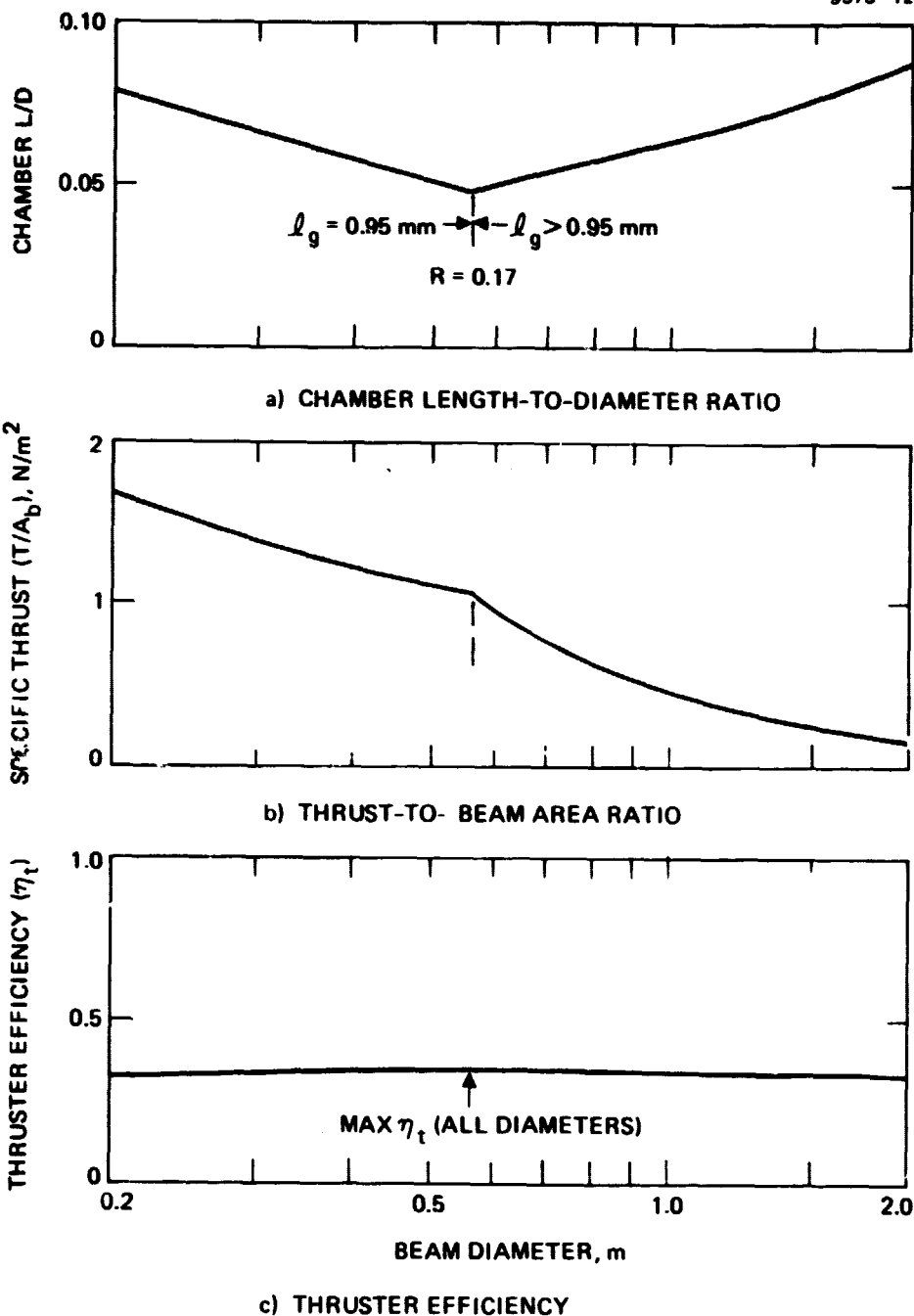


Figure A-7. Effect of beam diameter on performance. Propellant, argon; specific impulse, 2000 sec; propellant utilization, optimized for maximum thruster efficiency.

ORIGINAL PAGE IS
OF POOR QUALITY

9573-13

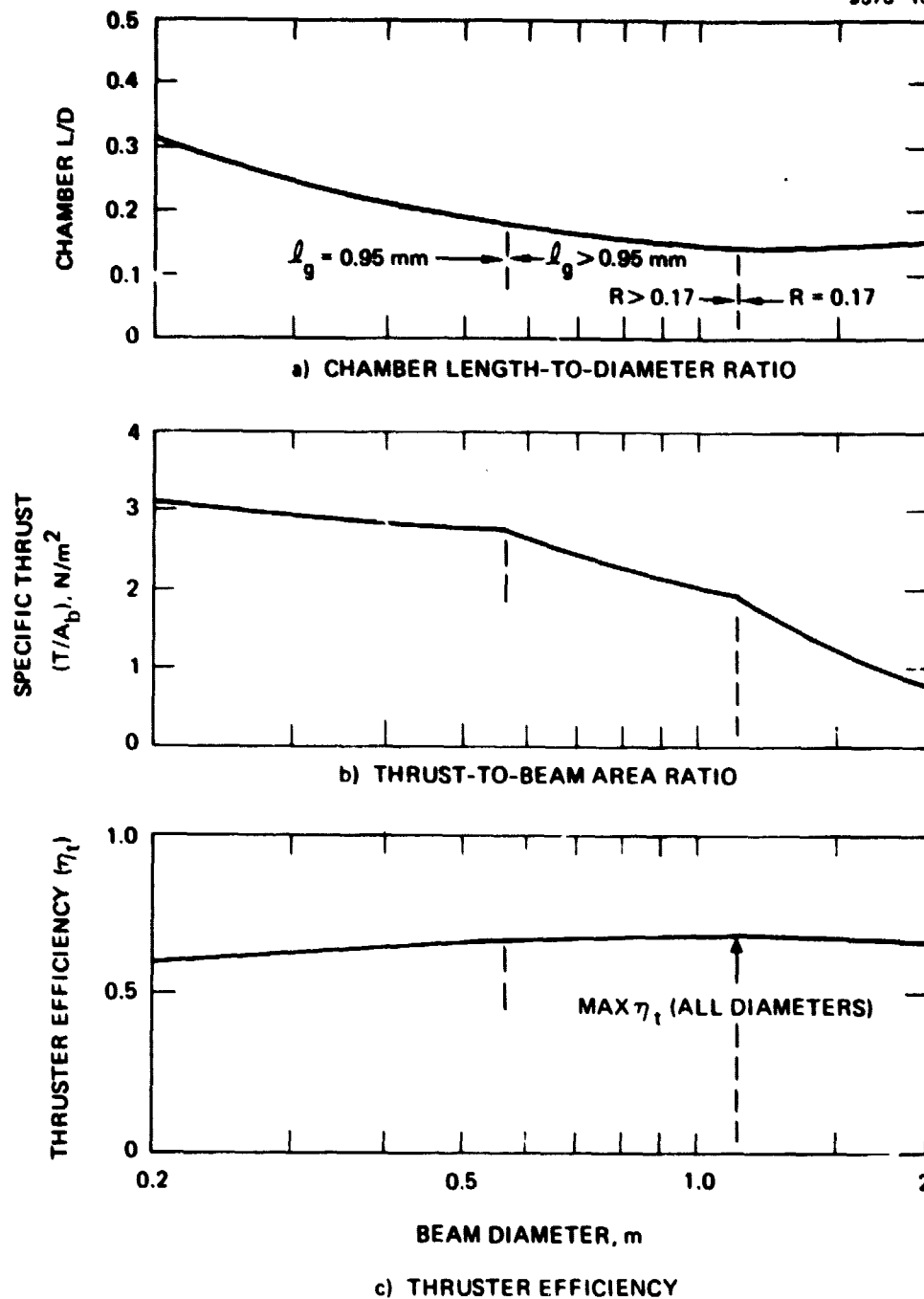


Figure A-8. Effect of beam diameter on performance. Propellant, argon; specific impulse, 5000 sec; propellant utilization, optimized for maximum thruster efficiency.

9573-14

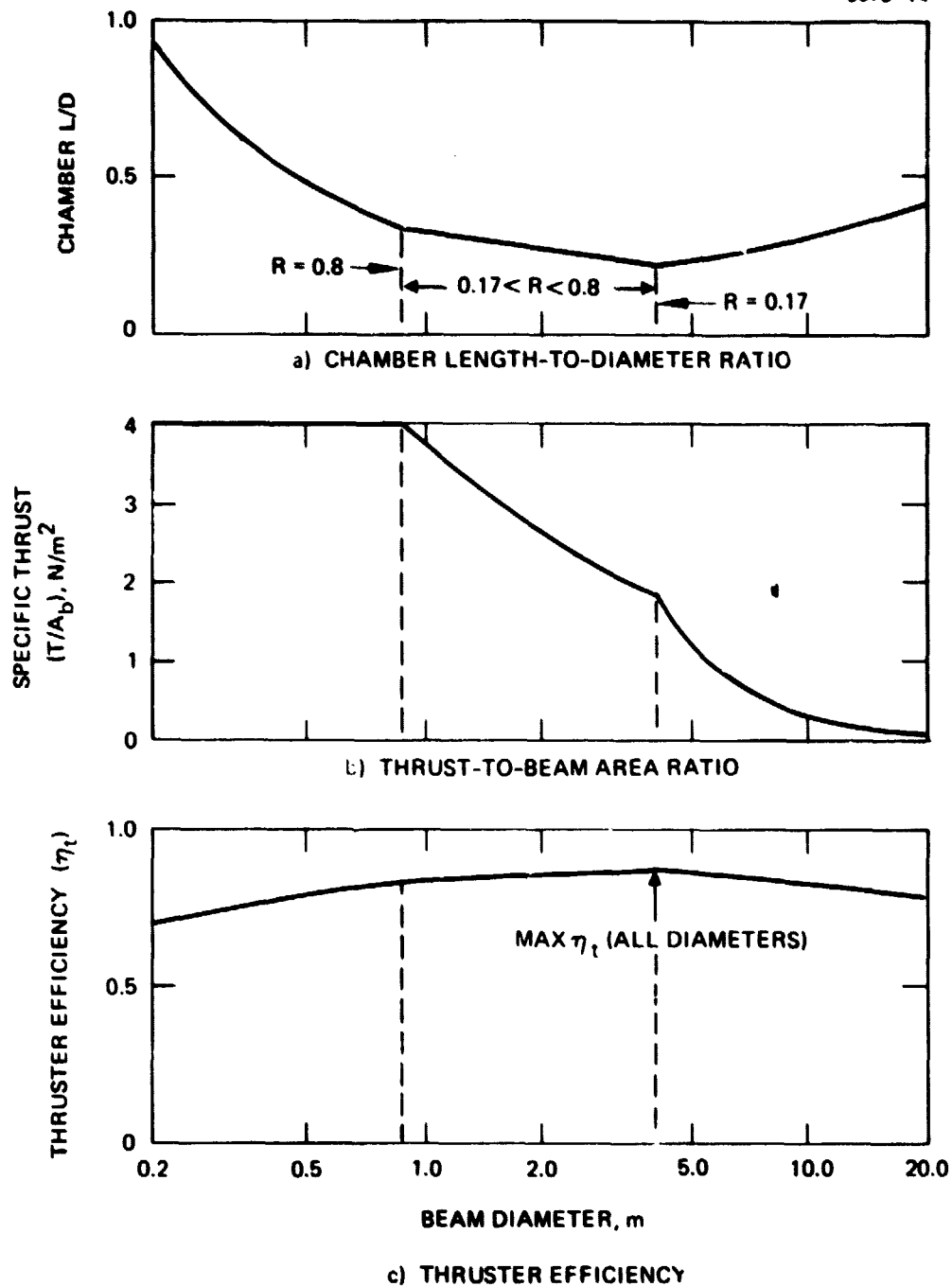


Figure A-9. Effect of beam diameter on performance. Propellant, argon; specific impulse, 10,000 sec; propellant utilization, optimized for maximum thruster efficiency.

9573-18

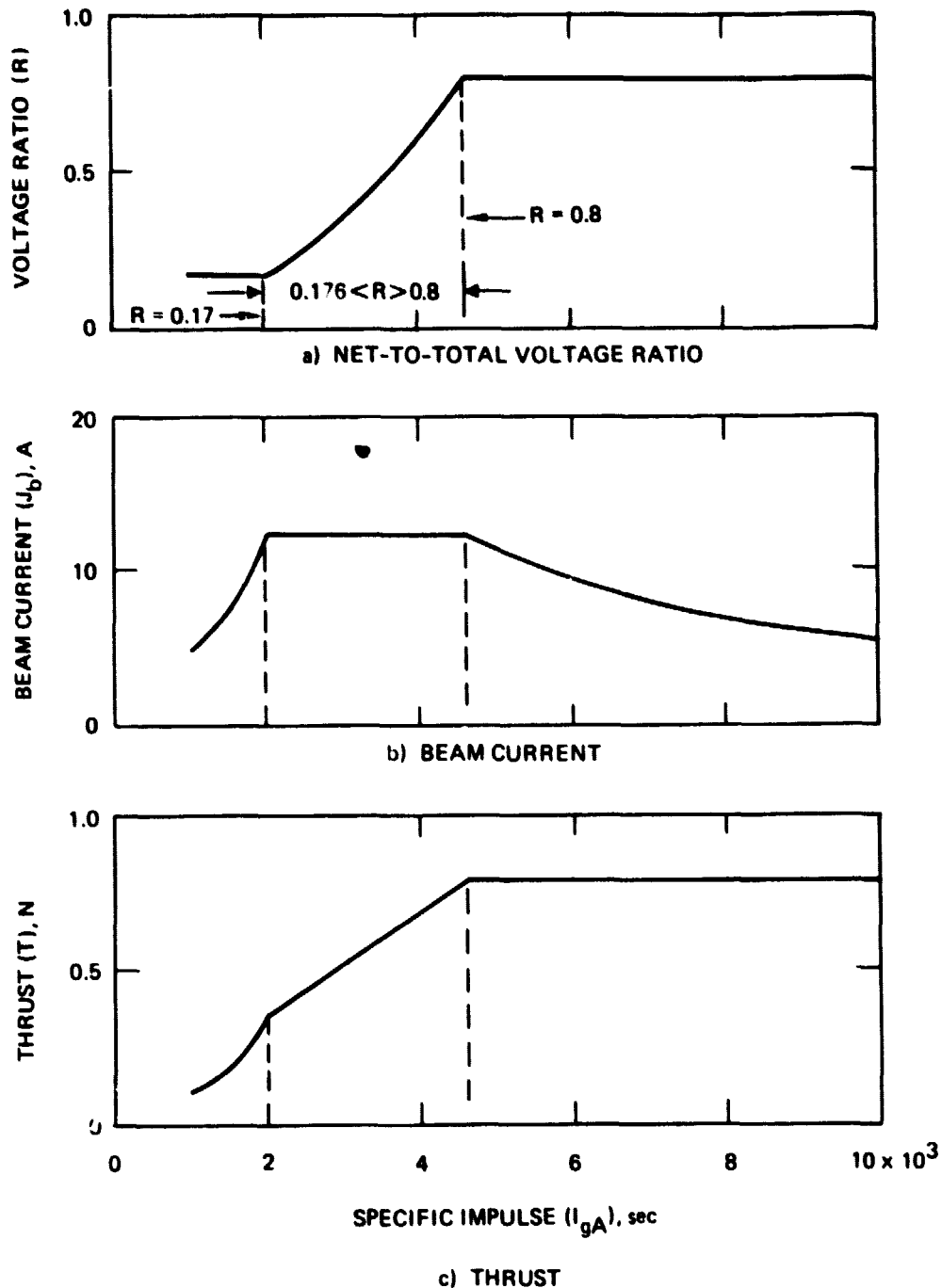
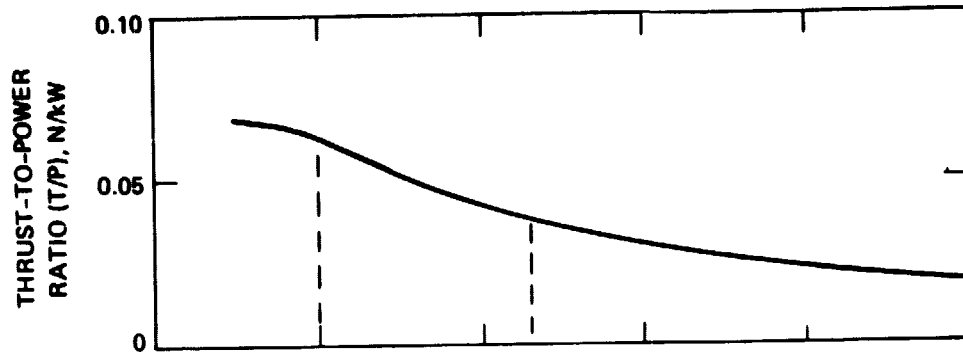
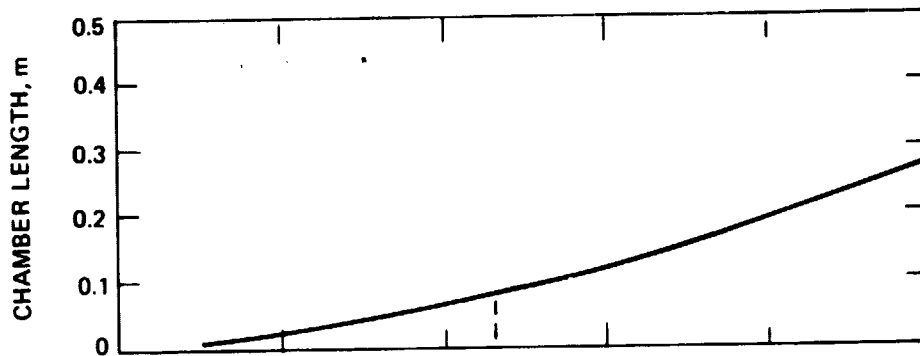


Figure A-10. Effect of specific impulse on voltage ratio, beam current, thrust, thrust to power ratio, discharge chamber length, and thruster efficiency. Propellant, xenon; beam diameter, 0.5 m; propellant utilization optimized for maximum thruster efficiency.

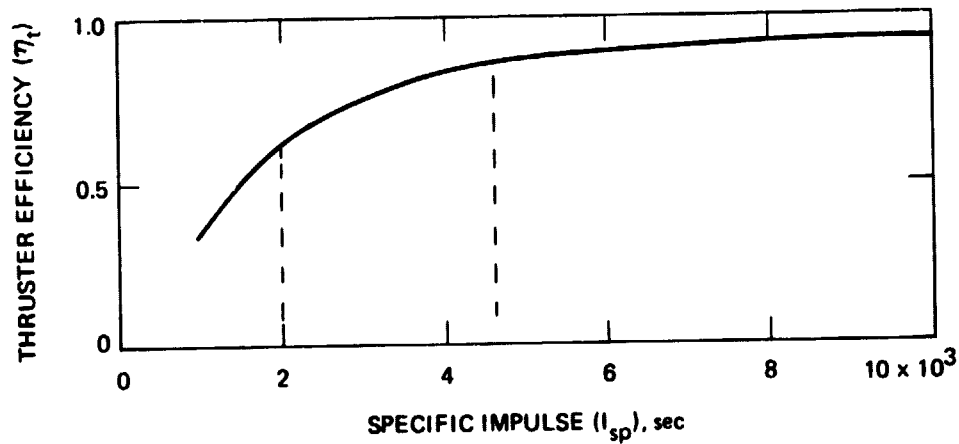
9573-16



d) THRUST-TO-POWER RATIO



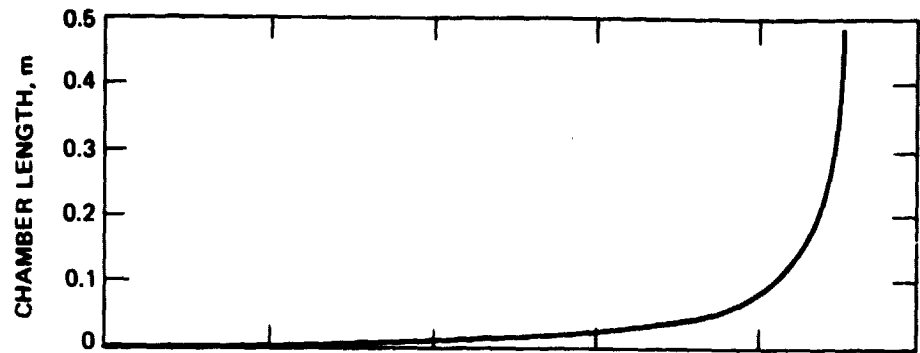
e) DISCHARGE CHAMBER LENGTH



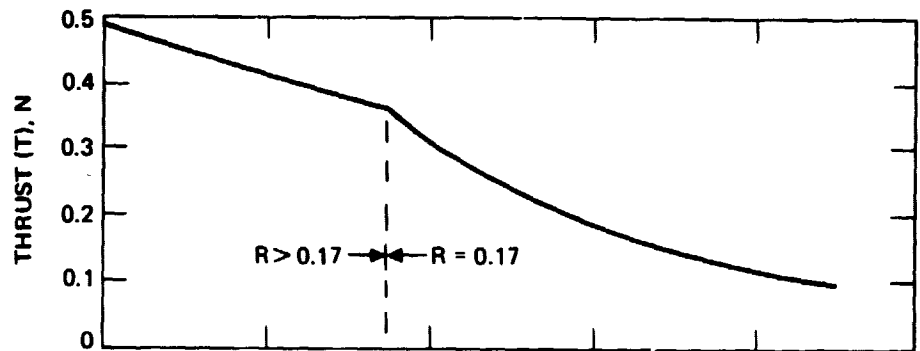
f) THRUSTER EFFICIENCY

Figure A-10. Continued.

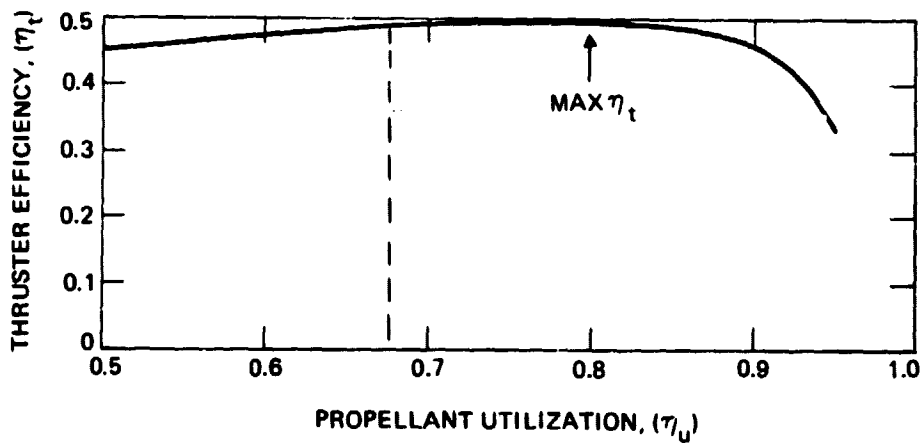
9573-17



a) DISCHARGE CHAMBER LENGTH



b) THRUST



c) THRUSTER EFFICIENCY

Figure A-11. Effect of propellant utilization on performance. Propellant, xenon; beam diameter, 0.5 m, specific impulse, 1500 sec.

9573-18

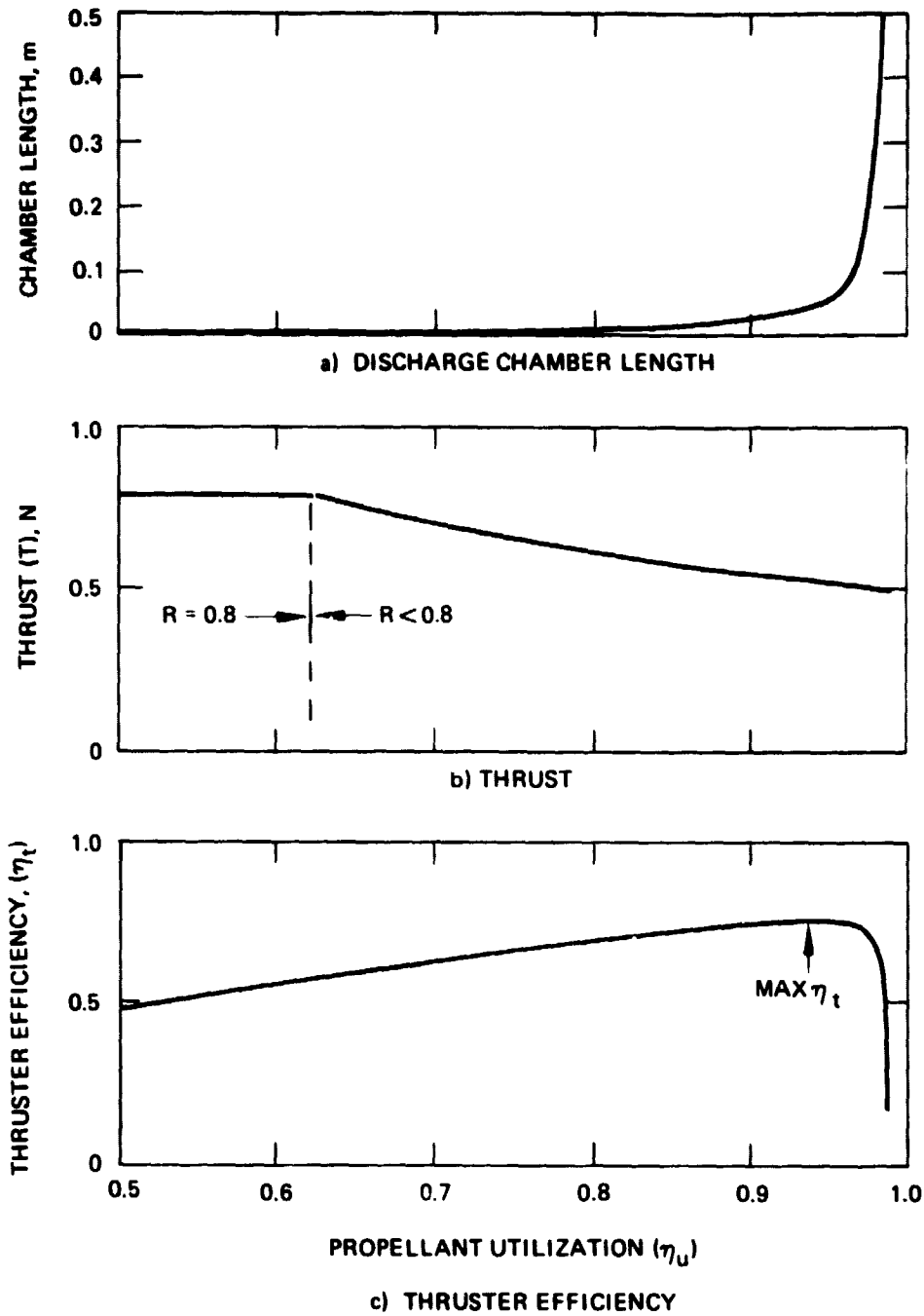


Figure A-12. Effect of propellant utilization on performance. Propellant, xenon; beam diameter, 0.5 m; specific impulse, 3000 sec.

9573-19

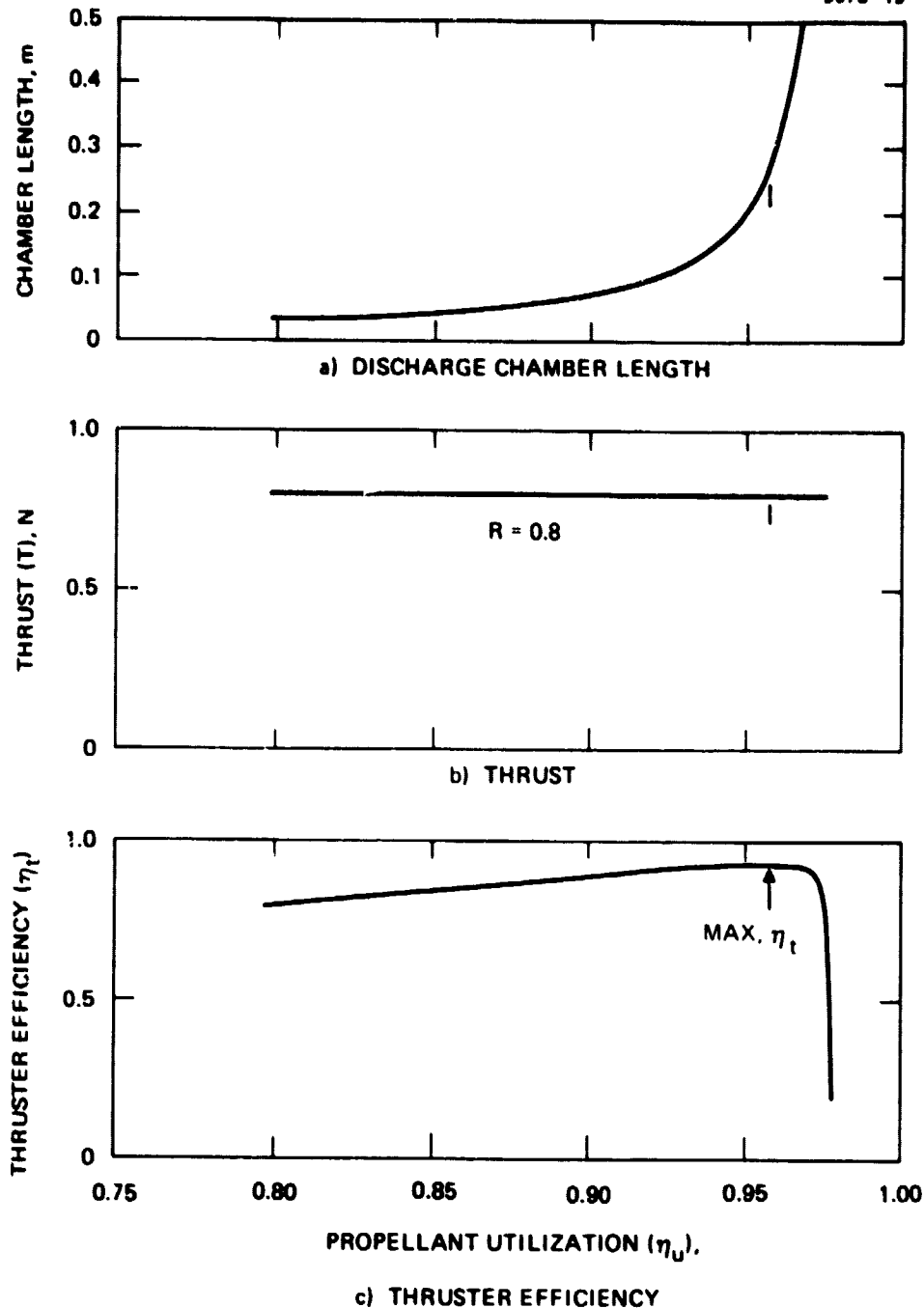


Figure A-13. Effect of propellant utilization on performance. Propellant, xenon; beam diameter, 0.5 m; specific impulse, 10,000 sec.

ORIGINAL PAGE IS
OF POOR QUALITY

9873-20

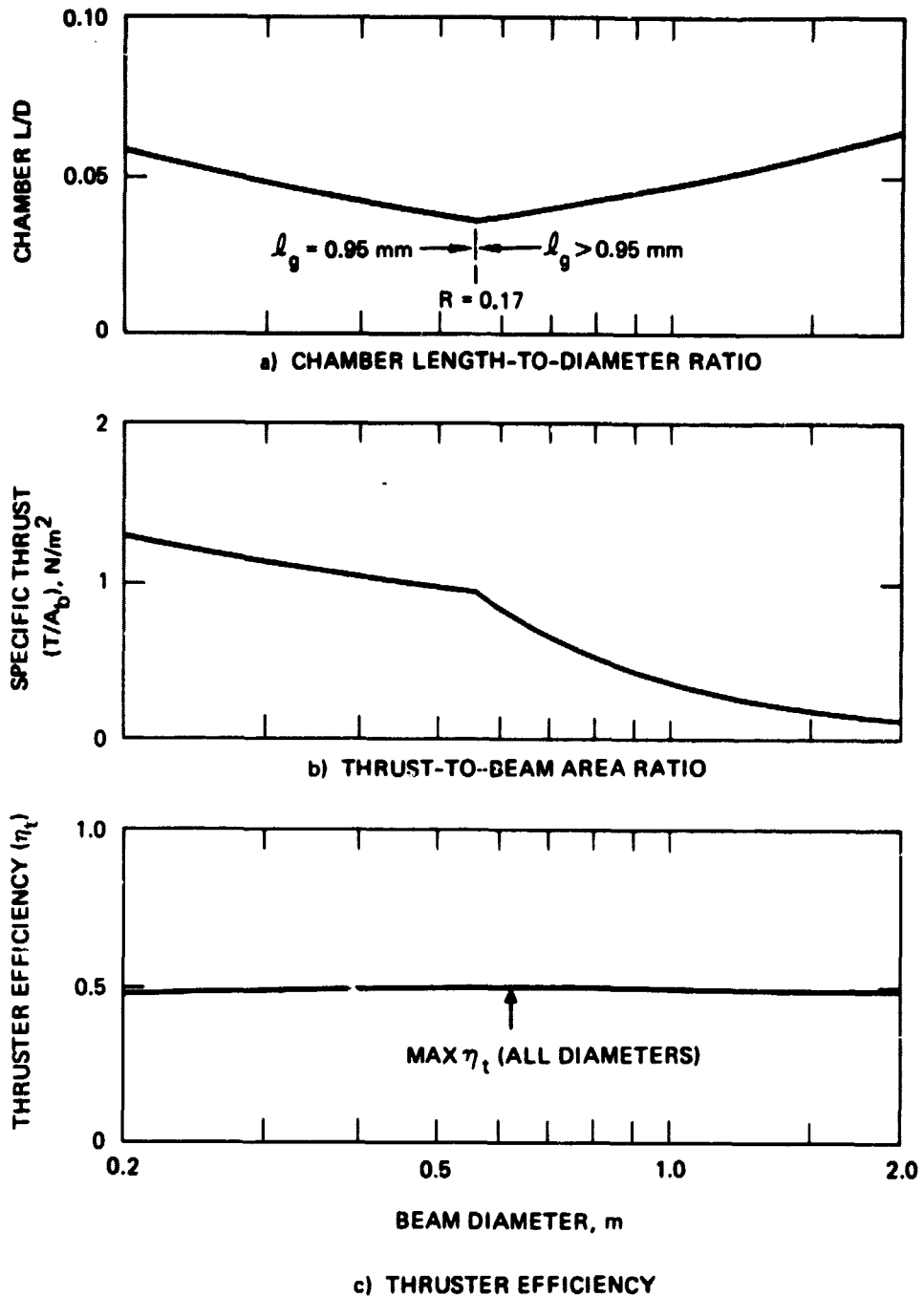
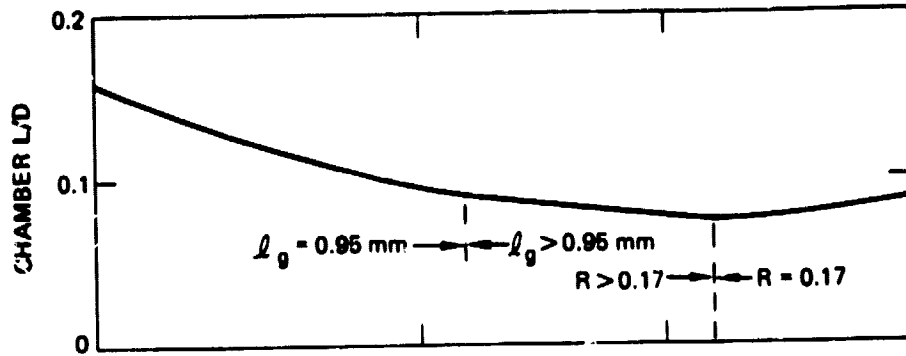
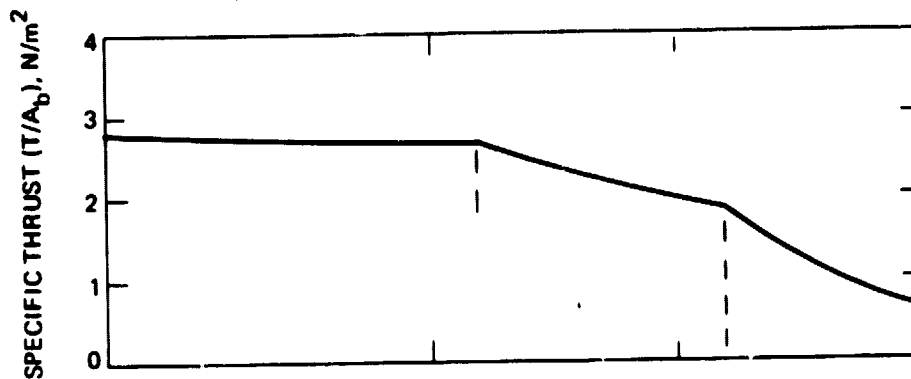


Figure A-14. Effect of beam diameter on performance. Propellant, xenon; specific impulse, 1500 sec. Propellant utilization, optimized for maximum thruster efficiency.

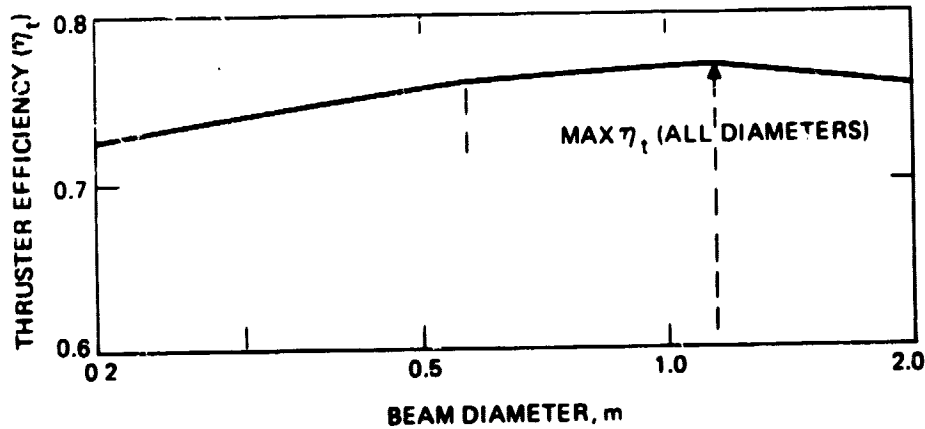
9573-21



a) CHAMBER LENGTH-TO-DIAMETER RATIO



b) THRUST-TO-BEAM AREA RATIO



c) THRUSTER EFFICIENCY

Figure A-15. Effect of beam diameter on performance. Propellant, xenon; specific impulse, 3000 sec; propellant utilization, optimized for maximum thruster efficiency.

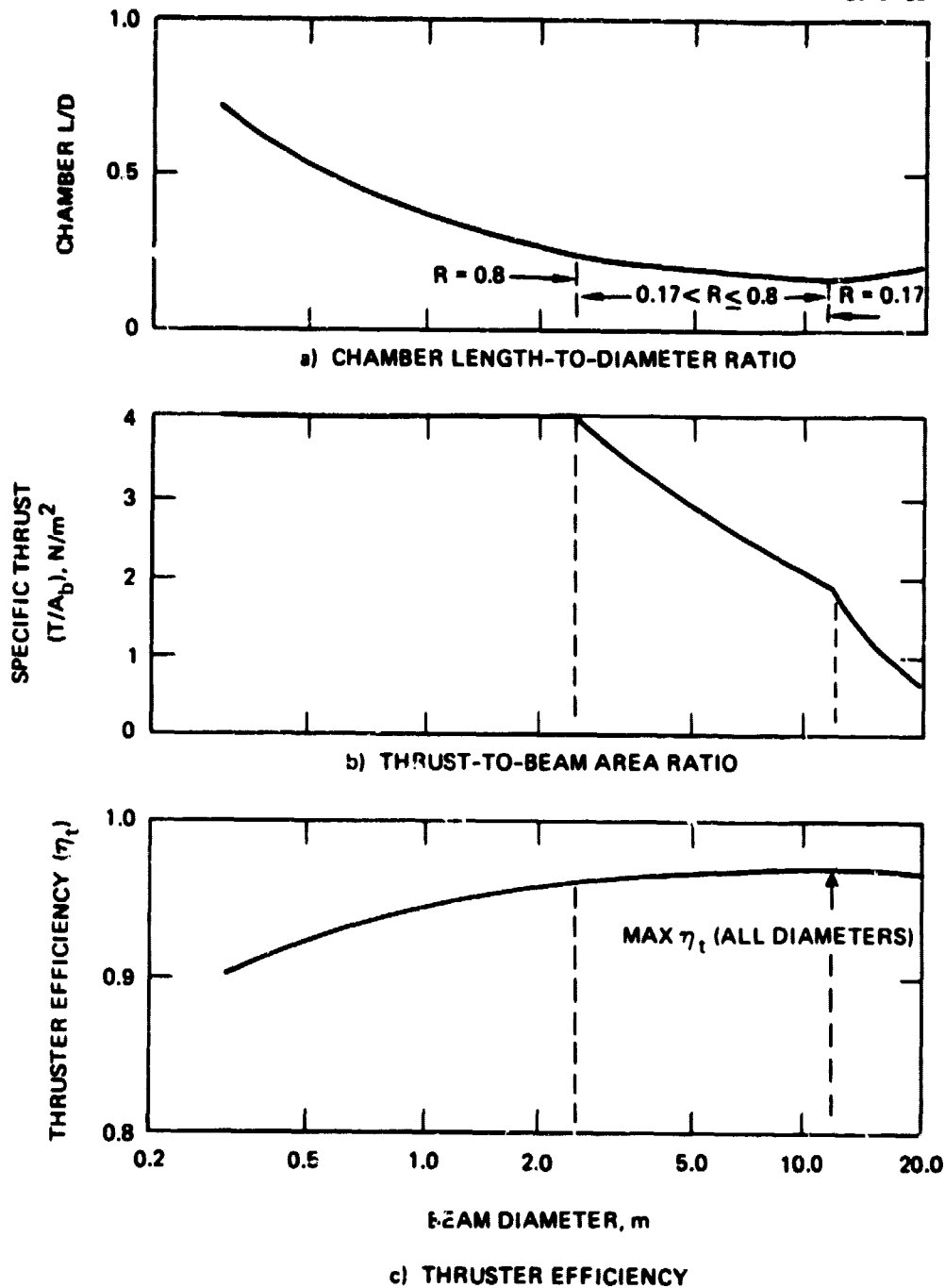


Figure A-16. Effect of beam diameter on performance. Propellant, xenon; specific impulse, 10,000 sec; propellant utilization, optimized for maximum thruster efficiency.

Beam Diameter, m	Specific Impulse, sec	Propellant Utilization, η_p	Thrust Efficiency, η_t	Power, KW	Thrust, N	Beam Current, A	Net Voltage, ΔV_n , V	Total Voltage, ΔV_t , V	Voltage Ratio, R	Grid Gap l_g , mm	Chamber Length, m	Discharge Loss, eV/ion
Table A-1 Argon Propellant, 0.5 m Beam Diameter, Optimum Propellant Utilization.												
1500.	0.454	0.263	4.64	0.166	12.4	217.	1279.	0.1700	0.950	0.020	157.	
2000.	0.566	0.344	6.21	0.217	15.2	249.	1462.	0.1700	0.950	0.026	161.	
2500.	0.633	0.419	8.46	0.289	18.8	289.	1686.	0.1700	0.950	0.031	164.	
3000.	0.745	0.488	11.1	0.367	22.4	323.	1899.	0.1700	0.950	0.041	170.	
4000.	0.819	0.588	14.8	0.445	22.4	475.	1900.	0.2500	0.950	0.070	187.	
5000.	0.849	0.658	20.0	0.537	22.4	691.	1900.	0.3635	0.950	0.093	200.	
6000.	0.867	0.709	26.2	0.631	22.4	954.	1900.	0.5019	0.950	0.114	213.	
7000.	0.880	0.746	33.3	0.725	22.4	1260.	1900.	0.6631	0.950	0.137	226.	
7770.	0.889	0.769	39.5	0.796	22.4	1521.	1901.	0.8000	0.951	0.157	238.	
8000.	0.891	0.773	40.4	0.796	21.8	1605.	2007.	0.8000	1.003	0.170	245.	
9000.	0.890	0.787	44.6	0.796	19.4	2036.	2545.	0.8000	1.273	0.205	266.	
10000.	0.888	0.797	49.0	0.796	17.4	2525.	3156.	0.8000	1.578	0.242	288.	

Table A-2 Argon Propellant, 0.5 m Beam Diameter, 2000 sec.										
0.40	0.307	14.6	0.465	22.4	498.	1900.	0.2620	0.950	0.008	151.
0.50	0.337	10.4	0.357	22.0	319.	1874.	0.1700	0.950	0.013	154.
0.566	0.344	6.21	0.217	15.2	249.	1462.	0.1700	0.950	0.026	161.
0.60	0.342	4.94	0.172	12.7	221.	1301.	0.1700	0.950	0.036	167.
0.70	0.303	3.01	0.0930	8.01	163.	956.	0.1700	0.950	0.115	213.
0.75	0.246	2.82	0.0705	6.51	142.	833.	0.1700	0.950	0.248	291.
0.77	0.207	3.01	0.0635	6.02	134.	790.	0.1700	0.950	0.377	366.
0.80	0.114	4.70	0.0545	5.37	124.	732.	0.1700	0.950	1.036	751.

Table A-3 Argon Propellant, 0.5 m Beam Diameter, 5000 sec.										
0.50	0.464	42.1	0.796	19.6	1991.	2489.	0.8000	1.245	0.015	155.
0.572	0.519	37.6	0.796	22.4	1521.	1902.	0.8000	0.951	0.017	156.
0.60	0.539	34.6	0.759	22.4	1383.	1900.	0.7278	0.950	0.019	157.
0.70	0.602	26.5	0.651	22.4	1016.	1900.	0.5347	0.950	0.032	164.
0.80	0.649	21.5	0.570	22.4	778.	1900.	0.4094	0.950	0.060	181.
0.849	0.558	20.0	0.537	22.4	691.	1900.	0.3135	0.950	0.093	200.
0.90	0.634	19.6	0.506	22.4	615.	1900.	0.3235	0.950	0.191	258.
0.93	0.546	22.0	0.496	22.4	576.	1900.	0.3029	0.950	0.444	405.
0.95	0.231	51.0	0.480	22.4	552.	1900.	0.2903	0.950	2.697	1721.

Table A-4 Argon Propellant, 0.5 m Beam Diameter, 10,000 sec.										
0.60	0.532	67.1	0.796	11.8	5331.	6914.	0.8000	3.457	0.040	169.
0.70	0.670	58.2	0.796	13.7	4064.	5080.	0.8000	2.540	0.056	179.
0.80	0.751	52.0	0.796	15.7	3111.	3889.	0.8000	1.945	0.095	202.
0.86	0.789	49.5	0.796	16.9	2692.	3365.	0.8000	1.633	0.162	241.
0.88	0.796	49.0	0.796	17.3	2571.	3214.	0.8000	1.607	0.212	270.
0.888	0.797	49.0	0.796	17.4	2525.	3007.	0.8000	1.578	0.242	288.
0.90	0.795	49.1	0.796	17.6	2458.	3073.	0.8000	1.536	0.307	325.
0.92	0.767	50.9	0.796	18.0	2353.	2941.	0.8000	1.470	0.554	470.
0.93	0.716	54.5	0.796	18.2	2302.	2878.	0.8000	1.439	0.927	687.
0.94	0.523	74.7	0.796	18.4	2254.	2817.	0.8000	1.408	0.283	1749.

Table A-5 Argon Propellant, Optimum Propellant Utilization, 2000 sec.											
0.20	0.511	0.329	1.56	0.0324	3.30	305.	1794.	0.1700	0.950	0.016	169.
0.30	0.536	0.336	2.84	0.0973	6.42	277.	1631.	0.1700	0.950	0.020	165.
0.40	0.553	0.340	4.40	0.153	10.4	260.	1532.	0.1700	0.950	0.023	162.
0.50	0.566	0.344	6.21	0.217	15.2	249.	1462.	0.1700	0.950	0.026	161.
0.57	0.574	0.345	7.59	0.267	18.9	242.	1422.	0.1700	0.950	0.027	160.
0.60	0.574	0.345	7.60	0.267	18.9	242.	1422.	0.1700	1.000	0.031	161.
0.70	0.562	0.343	8.33	0.291	20.1	252.	1483.	0.1700	1.167	0.037	162.
0.80	0.554	0.341	8.87	0.308	21.0	260.	1527.	0.1700	1.333	0.046	163.
1.00	0.541	0.337	9.85	0.339	22.4	272.	1601.	0.1700	1.667	0.064	165.
2.00	0.498	0.325	14.2	0.472	28.9	321.	1889.	0.1700	3.333	0.174	171.

Beam Diameter, m	Specific Impulse, sec	Propellant Utilization, η_u	Thrust Efficiency, η_t	Power, kW	Thrust, N	Beam Current, A	Net Voltage, AV, V	Total Voltage, AV, V	Voltage Ratio, R	Grid Gap, mm	Chamber Length, m	Discharge Loss, eV/ion
Table A-6 Argon Propellant, Optimum Propellant Utilization, 5000 sec.												
0.20		0.762	0.597	3.93	0.096	3.59	857.	1900.	0.4512	0.950	0.063	238.
0.30		0.805	0.627	7.96	0.204	8.08	766.	1900.	0.4033	0.950	0.075	219.
0.40		0.831	0.645	13.3	0.351	14.4	721.	1900.	0.3794	0.950	0.084	207.
0.50		0.849	0.658	20.0	0.537	22.4	691.	1900.	0.3635	0.950	0.093	200.
0.57		0.859	0.665	25.4	0.689	29.2	675.	1900.	0.3551	0.950	0.099	197.
0.70		0.866	0.670	34.0	0.931	39.7	664.	2333.	0.2845	1.167	0.114	194.
0.80		0.870	0.674	41.2	1.132	48.5	658.	2667.	0.2466	1.333	0.125	192.
1.00		0.877	0.679	56.7	1.569	67.8	647.	3333.	0.1942	1.667	0.147	189.
1.139		0.878	0.682	68.5	1.905	82.4	646.	3797.	0.1701	1.898	0.156	186.
1.50		0.855	0.672	77.4	2.120	89.3	681.	4006.	0.1700	2.500	0.204	186.
2.00		0.836	0.660	86.2	2.320	95.5	712.	4190.	0.1700	3.333	0.300	190.

Table A-7 Argon Propellant, Optimum Propellant Utilization, 10,000 sec.												
0.20		0.787	0.697	8.96	0.127	2.47	3215.	4019.	0.8000	2.009	0.183	414.
0.50		0.888	0.797	49.0	0.796	17.4	2525.	3156.	0.8000	1.578	0.242	288.
0.879		0.922	0.835	144.	2.460	55.9	2342.	2930.	0.7994	1.465	0.296	244.
1.0		0.925	0.838	174.	2.975	67.8	2327.	3333.	0.6982	1.667	0.324	241.
2.0		0.940	0.854	476.	8.290	191.	2258.	6667.	0.3387	3.333	0.532	224.
3.90		0.949	0.867	1263.	22.34	522.	2211.	13000.	0.1701	6.500	0.838	209.
5.0		0.941	0.859	1320.	23.12	536.	2249.	13228.	0.1700	8.322	1.186	215.
10.		0.913	0.830	1541.	26.09	587.	2389.	14052.	0.1700	16.67	3.154	238.
20.		0.874	0.793	1920.	31.07	669.	2500.	15334.	0.1700	33.33	8.134	265.

Table A-8 Xenon Propellant, 0.5 m Beam Diameter, Optimum Propellant Utilization.												
1000.		0.613	0.340	1.54	0.107	4.90	174.	1025.	0.1700	0.950	0.011	140.
1500.		0.799	0.492	2.80	0.187	7.47	231.	1357.	0.1700	0.950	0.019	144.
2000.		0.900	0.617	5.93	0.367	12.4	323.	1900.	0.1701	0.950	0.026	148.
2500.		0.925	0.700	7.82	0.446	12.4	477.	1900.	0.2511	0.950	0.038	154.
3000.		0.939	0.758	10.3	0.528	12.4	668.	1900.	0.3517	0.950	0.048	160.
4000.		0.953	0.830	16.4	0.694	12.4	1153.	1900.	0.6069	0.950	0.068	170.
4620.		0.959	0.858	21.0	0.796	12.4	1519.	1900.	0.7996	0.950	0.082	180.
5000.		0.959	0.870	22.4	0.796	11.4	1779.	2224.	0.8000	1.112	0.091	183.
6000.		0.960	0.891	26.3	0.796	9.34	2557.	3196.	0.8000	1.598	0.122	200.
7000.		0.960	0.904	30.2	0.796	8.18	3480.	4350.	0.8000	2.175	0.155	217.
8000.		0.960	0.912	34.2	0.796	7.16	4546.	5682.	0.8000	2.841	0.195	238.
9000.		0.959	0.918	38.3	0.796	6.36	5765.	7206.	0.8000	3.603	0.231	258.
10000.		0.958	0.922	42.4	0.796	5.71	7132.	8915.	0.8000	4.458	0.272	280.

Table A-9 Xenon Propellant, 0.5 m Beam Diameter, 1500 sec.											
0.50	0.407	8.97	0.496	12.4	589.	1900.	0.3101	0.950	0.003	135.	
0.60	0.450	6.75	0.413	12.4	409.	1900.	0.2153	0.950	0.004	136.	
0.65	0.467	6.01	0.381	12.4	349.	1900.	0.1835	0.950	0.005	137.	
0.675	0.474	5.70	0.367	12.4	323.	1900.	0.1701	0.950	0.006	137.	
0.75	0.489	3.63	0.241	9.01	262.	1540.	0.1700	0.950	0.011	140.	
0.799	0.492	2.80	0.137	7.47	231.	1537.	0.1700	0.950	0.019	144.	
0.85	0.487	2.21	0.146	6.21	204.	1199.	0.1700	0.950	0.034	152.	
0.90	0.461	1.85	0.116	5.23	182.	1070.	0.1700	0.950	0.073	173.	
0.93	0.415	1.81	0.102	4.74	170.	1002.	0.1700	0.950	0.144	211.	
0.95	0.332	2.07	0.0937	4.45	163.	960.	0.1700	0.950	0.316	303.	

Table A-10 Xenon Propellant, 0.5 m Beam Diameter, 3000 sec.											
0.50	0.473	24.8	0.796	9.94	2356.	2946.	0.8000	1.473	0.003	136.	
0.55	0.514	22.3	0.796	10.9	1948.	2434.	0.8000	1.217	0.004	136.	
0.623	0.572	20.5	0.796	12.4	1518.	1900.	0.7989	0.950	0.004	136.	
0.75	0.662	14.7	0.661	12.4	1027.	1900.	0.5512	0.950	0.008	138.	
0.85	0.724	11.9	0.533	12.4	815.	1900.	0.4292	0.950	0.016	143.	

Beam Diameter, m	Specific Impulse, sec	Propellant Utilization, η_u	Thrust Efficiency, η_c	Power, KW	Thrust, N	Beam Current, A	Nec Voltage, V_n	Total Voltage, V_t	Voltage Ratio, R	Grid Gap g , mm	Chamber Length, m	Discharge Loss, eV/ion
Table A-10 Xenon Propellant, 0.5 m Beam Diameter, 3000 sec. (Continued)												
0.90	0.748	10.8	0.551	12.4	727.	1900.	0.3828	0.950	0.026	148.		
0.93	0.757	10.4	0.553	12.4	681.	1900.	0.3585	0.950	0.041	156.		
0.939	0.758	10.3	0.528	12.4	668.	1900.	0.3517	0.950	0.048	160.		
0.95	0.756	10.2	0.522	12.4	653.	1900.	0.3436	0.950	0.063	168.		
0.97	0.732	10.3	0.511	12.4	626.	1900.	0.3295	0.950	0.129	203.		
0.98	0.675	11.0	0.506	12.4	613.	1900.	0.3228	0.950	0.268	277.		

Table A-11 Xenon Propellant, 0.5 m Beam Diameter, 10,000 sec.												
0.80	0.788	49.5	0.796	4.77	10228.	12785.	0.8000	6.392	0.031	150.		
0.85	0.836	46.7	0.796	5.07	9060.	11325.	0.8000	5.662	0.043	157.		
0.90	0.881	44.3	0.796	5.37	8081.	10102.	0.8000	5.051	0.070	172.		
0.93	0.907	43.1	0.796	5.55	7568.	9460.	0.8000	4.730	0.114	195.		
0.95	0.920	42.4	0.796	5.67	7253.	9066.	0.8000	4.533	0.195	238.		
0.956	0.922	42.4	0.796	5.71	7132.	8915.	0.8000	4.458	0.272	280.		
0.96	0.922	42.4	0.796	5.73	7103.	8878.	0.8000	4.439	0.302	296.		
0.97	0.905	43.1	0.796	5.79	6957.	8696.	0.8000	4.348	0.675	496.		

Table A-12 Xenon Propellant, Optimum Propellant Utilization, 1500 sec.												
0.20	0.744	0.477	0.615	0.0399	1.48	266.	1565.	0.1700	0.950	0.011	149.	
0.30	0.769	0.484	1.19	0.0786	3.02	249.	1465.	0.1700	0.950	0.014	147.	
0.40	0.787	0.489	1.92	0.127	5.00	238.	1399.	0.1700	0.950	0.017	145.	
0.50	0.799	0.492	2.80	0.197	7.47	231.	1357.	0.1700	0.950	0.019	144.	
0.57	0.807	0.494	3.48	0.224	9.42	226.	1330.	0.1700	0.950	0.020	143.	
0.70	0.795	0.491	3.72	0.248	9.86	233.	1371.	0.1700	1.167	0.027	144.	
1.0	0.774	0.485	4.19	0.276	10.7	246.	1446.	0.1700	1.667	0.046	146.	
1.5	0.749	0.478	4.85	0.315	11.8	263.	1544.	0.1700	2.500	0.083	149.	
2.0	0.730	0.472	5.44	0.349	12.7	276.	1626.	0.1700	3.233	0.125	151.	

Table A-13 Xenon Propellant, Optimum Propellant Utilization, 3000 sec.												
0.20	0.900	0.725	1.79	0.0831	1.98	727.	1900.	0.3828	0.950	0.031	176.	
0.30	0.920	0.741	3.85	0.194	4.46	696.	1900.	0.3663	0.950	0.038	168.	
0.40	0.931	0.751	6.63	0.311	7.92	680.	1900.	0.3577	0.950	0.043	163.	
0.50	0.939	0.758	10.3	0.528	12.4	668.	1900.	0.3517	0.950	0.048	160.	
0.57	0.943	0.761	13.2	0.683	16.1	662.	1900.	0.3487	0.950	0.052	158.	
0.60	0.944	0.762	14.2	0.737	17.4	661.	2000.	0.3305	1.000	0.054	153.	
0.70	0.946	0.764	17.8	0.927	21.9	658.	2333.	0.2821	1.167	0.060	157.	
0.80	0.943	0.766	21.7	1.130	26.7	656.	2667.	0.2458	1.333	0.066	156.	
1.0	0.951	0.768	30.1	1.574	37.4	651.	3333.	0.1954	1.667	0.078	155.	
1.145	0.953	0.770	36.8	1.928	45.8	649.	3816.	0.1700	1.908	0.087	154.	
1.5	0.943	0.764	38.6	2.007	47.3	662.	3897.	0.1700	2.500	0.119	155.	
2.0	0.934	0.757	40.5	2.085	48.6	675.	3972.	0.1700	3.233	0.179	158.	

Table A-14 Xenon Propellant, Optimum Propellant Utilization, 10,000 sec.												
0.30	0.938	0.899	15.6	0.297	2.01	7440.	9300.	0.8000	4.650	0.215	326.	
0.50	0.954	0.922	42.4	0.796	5.71	7132.	8915.	0.8000	4.458	0.272	280.	
0.70	0.967	0.931	82.0	1.561	11.3	7000.	8750.	0.8000	4.375	0.315	255.	
1.0	0.974	0.942	116.	3.135	23.2	6900.	8625.	0.8000	4.310	0.364	231.	
1.5	0.981	0.951	170.	7.166	52.7	6802.	8502.	0.8000	4.251	0.468	218.	
2.0	0.984	0.955	254.	12.74	93.9	6760.	8451.	0.8000	4.225	0.520	204.	
2.52	0.986	0.958	335.	20.23	149.	6734.	8416.	0.8000	4.208	0.567	194.	
3.0	0.987	0.959	434.	26.27	194.	6719.	10000.	0.6719	5.000	0.662	193.	
5.0	0.989	0.962	2875.	56.41	418.	6692.	16667.	0.4015	8.333	0.977	186.	
7.0	0.990	0.964	4749.	93.35	692.	6679.	23333.	0.2862	11.67	1.239	181.	
11.76	0.991	0.966	10308.	203.1	1507.	6665.	39200.	0.1700	19.60	1.701	173.	
15.0	0.990	0.964	10374.	203.9	1512.	6679.	39287.	0.1700	25.00	2.587	180.	
20.0	0.988	0.961	15075.	205.6	1522.	6706.	39428.	0.1700	31.33	3.940	187.	

ORIGINAL PAGE IS
OF POOR QUALITY

ORIGINAL PAGE IS
OF POOR QUALITY

Propellant Utilization (η_u)	Voltage Ratio (R)	Beam Current (J_b)	Thruster Efficiency (η_t)	Power (P, kw)	Thrust (T, N)	Grid Gap (ℓ_g , mm)	Net Voltage ΔV_n , V	Total Voltage ΔV_t , V	Chamber Length (ℓ_{ch} , mm)	Discharge Loss (eV/ion)	Power Efficiency (η_p)
Table A-15 Argon, $I_{sp} = 6076$, $d_b = 0.5$ m											
0.70	0.7896	22.44	0.6308	37.36	0.7911	0.950	1500	1900	31.7	164	0.9012
0.75	0.6878	22.44	0.6634	33.16	0.7383	0.950	1307	1900	42.2	171	0.8845
0.80	0.5345	22.44	0.6912	29.84	0.6922	0.950	1149	1900	59.7	181	0.8640
0.85	0.5355	22.44	0.7099	27.34	0.6515	0.950	1017	1900	93.9	201	0.8352
0.869	0.5123	22.44	0.7121	26.66	0.6372	0.950	973	1900	117.6	215	0.8194
0.89	0.4884	22.44	0.7076	26.20	0.6222	0.950	928	1900	159.6	239	0.7951
0.90	0.4777	22.44	0.7009	26.15	0.6153	0.950	908	1900	191.3	258	0.7788
0.91	0.4672	22.44	0.6891	26.31	0.6025	0.950	888	1900	237.4	285	0.7572

Table A-16 Xenon, $I_{sp} = 3530$, $d_b = 0.5$ m											
0.80	0.6708	12.38	0.7209	17.51	0.7291	0.950	1274	1900	11.0	140	0.9011
0.85	0.5942	12.38	0.7547	15.74	0.6862	0.950	1129	1900	15.9	143	0.8879
0.90	0.5300	12.38	0.7846	14.30	0.6481	0.950	1007	1900	26.2	148	0.8718
0.92	0.5072	12.38	0.7943	13.82	0.6340	0.950	964	1900	34.5	153	0.8634
0.94	0.4859	12.38	0.8007	13.41	0.6205	0.950	923	1900	49.5	161	0.8519
0.94 ^a	0.4777	12.38	0.8015	13.29	0.6153	0.950	908	1900	59.5	166	0.8454
0.95	0.4757	12.38	0.8014	13.26	0.6140	0.950	904	1900	62.7	168	0.8436
0.955	0.4707	12.38	0.8005	13.21	0.6108	0.950	894	1900	72.1	173	0.8382
0.96	0.4658	12.38	0.7982	13.18	0.6076	0.950	885	1900	84.8	179	0.8314
0.965	0.4610	12.38	0.7938	13.18	0.6044	0.950	876	1900	102.6	189	0.8225
0.97	0.4513	12.38	0.7852	13.25	0.6013	0.950	867	1900	129.5	203	0.8100

above the backstreaming limit if the gap is maintained at the minimum value. The maximum beam current in this range is obtained by increasing the gap (at maximum electric field) until the total voltage, with the calculated net voltage, corresponds to the maximum permissible R . This region also corresponds to constant thrust (see Figures A-3(c) and A-10(c)). In a space-charge-limited condition, the electric field force at the accelerator corresponds to the time-rate-of-change of charged particle momentum between the emitter and the accelerator. With constant electric field, then, the thrust force at the accelerator is constant. With R also constant, a constant fraction of this thrust appears as thrust after deceleration.

Although the number of grids is not indicated, a three-grid ion optics assembly is assumed for any R below 0.7. In the R range from 0.7 to 0.8, either two- or three-grid optics could be used.

The thrust-to-power ratio (see Figures A-3(d) and A-10(d)) generally rises as specific impulse is reduced, as one would expect from the reduced kinetic energy requirements of lower specific impulses. What is less obvious is the leveling off of thrust-to-power ratio at low specific impulses. For a constant discharge loss and a constant propellant utilization, the thrust-to-power ratio will actually show a maximum at a net voltage equal to the discharge loss in eV/ion (power efficiency of 0.5). The optimization of propellant utilization used here prevents this maximum from being evident. As the specific impulse is decreased below the value where this maximum might be expected, the optimization procedure selects increasingly lower propellant utilizations. For example, argon at 1500 sec gives an optimum propellant utilization of 0.454, while xenon at 1000 sec gives 0.613. The thrust-to-power ratio rises slightly at these low specific impulses because the low utilizations are obtained by using very shallow discharge chambers, which, in turn, give very low discharge losses. For argon at 1500 sec, the 0.5-m-diameter chamber has a depth of only 2 cm, while for xenon at 1000 sec, the depth is only 1.1 cm.

Optimum operation at very low specific impulses is, in effect, obtained by operating at near optimum electrical values and throwing away increasing fractions of un-ionized propellant as specific impulse is decreased. Such operation will generally not be of interest in mission analysis: if it should appear to be preferred, it usually indicates that a stage mismatch exists. That is, overall performance would be increased by using a smaller mass for the electric propulsion stage and operating the thruster at a high specific impulse. Such a mismatch may exist in any case where a thruster efficiency less than about 0.5 is indicated as being desirable.

Sensitivity analyses are shown for variations of propellant utilization about the optimum values in Figures A-4 through A-6 for argon and Figures A-11 through A-13 for xenon. In the low specific impulse range ($R = 0.17$ at optimum utilization), shown in Figures A-4 and A-11, relatively large departures from optimum propellant utilization cause small decreases from maximum thruster efficiency, not thrust, as clearly indicated by Figures A-4(b) and A-11(b). Small decreases in thruster efficiency from maximum can be exchanged for relatively large increases in thrust. These thrust increases correspond to operating at higher net and total voltages, so that the increased thrusts result from the increased current capacities of the ion optics at the higher voltages. At a sufficiently low propellant utilization, the total voltage can reach the maximum electric field value and R must increase above 0.17. Although shown only for xenon, the same change in R occurs at lower propellant utilization than covered in Figure A-4 for argon.

The effect of varying propellant utilization away from optimum has a more pronounced effect on thruster efficiency at higher specific impulses, as shown in Figures A-5, A-6, A-12, and A-13. Decreasing propellant utilization from the optimum value increases thrust slightly in the intermediate specific impulse range (Figures A-5 and A-12), and not all in the high specific impulse range (Figures A-6 and A-13).

The effects of varying thruster diameter are shown in Figures A-7 through A-9 and Figures A-14 through A-16. All data shown in these figures were optimized for maximum thruster efficiency at each thruster

diameter. As with the effect of propellant utilization variations, the nature of diameter effects depend on the specific impulse range under consideration.

At the lowest specific impulse, Figures A-7 and A-14, the grid gap remains at the 0.95 mm value until a beam diameter of 0.57 m is reached. Above this diameter, the span-to-gap limit required that the gap be increased proportionally with the diameter. The effect on thrust can best be understood by first ignoring the effect of propellant utilization changes. For beam diameters less than 0.57 m, the grid gap is fixed at 0.95 mm, and the thrust per unit area should be constant at a constant specific impulse. At beam diameters larger than 0.57 m, all ion optics dimensions are increased in proportion to the beam diameter. At constant propellant utilization, the voltages would again be constant. A classic space-charge-flow calculation has shown that beam current (and thrust) are independent of ion optics size when all dimensions are changed in proportion with voltages held constant.

We will now include the additional effects of changing propellant utilization. As beam diameter is decreased from 0.57 m, the volume-to-area ratio, the primary electron region, V_p/A_p , tends to decrease. Although (A_o) also decreases, beam current decreases about the same amount, and hence the net effect on propellant utilization is negligible. This tendency to decrease V_p/A_p can be partially offset by an increase in discharge chamber ℓ_o/d_b . But, because an increase in ℓ_o/d_b also results in an increase in discharge losses, the increase in ℓ_o/d_b must be a compromise between maintaining propellant utilization and increasing discharge losses. This compromise results in a net decrease in optimized thruster efficiency. There is also a net loss in propellant utilization as beam diameter is decreased below 0.57 m. This loss results in increases in net and total voltages; these increases are the cause of the increase in the thrust-to-beam area ratio as beam diameter is increased.

When beam diameter is increased above 0.57 m, the ratio V_p/A_p tends to increase. But this is more than offset by the increase in A_j , which

increases with the beam diameter squared. But with beam current tending to remain constant as beam diameter is increased, the propellant utilization must suffer a net decrease. This net decrease, in turn, results in a decrease in optimized thruster efficiency as beam diameter is increased above 0.57 m.

Maximum thruster efficiency (all beam diameters) in the low specific impulse range thus corresponds to the maximum beam diameter for which the minimum grid gap can be maintained. The thruster mass has not been discussed, but it normally increases somewhat less rapidly than beam area. It appears that maximum thrust-to-weight ratio would also be found at a beam diameter of 0.57 m. Further, the mass penalty for going above 0.57 m appears to be substantial. Large thrust applications in this specific impulse range thus strongly indicate the use of the maximum beam diameter consistent with the minimum grid gap.

The tradeoffs are slightly different for beam diameter variations in the intermediate specific impulse range (Figures A-8 and A-15). Above a beam diameter of 0.57 m, the grid gap again increases above the 0.95 mm value. However, the freedom to decrease R as the grid gap is increased more than offsets any thruster efficiency loss that might be expected from the grid gap increase. The efficiency tradeoff shifts when R is decreased to 0.17 since further diameter increases result in a net loss in optimized thruster efficiency as well as a rapid loss in the thrust-to-beam area ratio.

The variation in thrust-to-mass ratio is probably not great in the diameter range with $\ell_g > 0.95$ mm and $R > 0.17$. The need for both maximum thruster efficiency and minimum parts count (for increased reliability and reduced cost) would thus indicate a beam diameter for large thrust systems such that an R of 0.17 is just reached. That is, the beam diameter is such that the grid gap (from the span-to-gap limit) corresponds simultaneously to maximum electric field and to an R of 0.17.

Except for having a region with $R = 0.8$, the qualitative effects of varying beam diameter in the high specific impulse range (Figures A-9 and A-16) are similar to the effects described above. Again, the optimum beam diameter appears to correspond to maximum electric field

and an R of 0.17 at a grid gap given by the span-to-gap limit. The optimum beam diameter at 10000 sec, however, is quite large - 3.90 m for argon and 11.76 m for xenon. The power levels are even larger for this optimum beam diameter - 1.26 MW for argon and 10.31 MW for xenon.

B. CONCLUSIONS

Much of the significance of the large thruster analysis presented here lies in the specific performance values obtained. These values are adequately presented in the various figures and tables that have been included and need not be repeated here. There are other significant results, however, that may not be as obvious.

One result was the extremely shallow depths obtained for optimum discharge chambers. At 5000 sec, for example, the optimum depths for 0.5-m-diameter chambers were less than 0.1 m for both argon and xenon. At lower specific impulses, the optimum chamber depths were even less than 10 cm. The sensitivity analysis for propellant utilization indicates that small increases in depth from the optimum value will result in even smaller losses in efficiency. Even so, the optimum depths are well below what might be expected without detailed analysis. Only at specific impulses approaching 10,000 sec do the length-to-diameter ratios of the discharge chambers approach values normally expected.

The distribution of electrons to a chamber with an ℓ_p/d_b of 0.2, or less, is another aspect that deserves mention. Obtaining a uniform distribution of primaries from a single baffle annulus is probably beyond present technology.

The effect of beam diameter on thruster performance was examined at low, intermediate, and high specific impulses. The optimum choice of beam diameter for very large systems was indicated for these three ranges. The optimum choice of beam diameter can also be described in terms of simultaneously satisfying multiple limits. These limits are minimum net-to-total voltage ratio, maximum span-to-gap ratio, and either minimum gap or maximum electric field. Further examination of these limits should obviously be considered in future technology studies.

The size, power, and efficiency limits indicated by this study are clearly much more restrictive at low specific impulses. Alternatives to "conventional" discharge chambers and ion optics could offer substantial advantages at these low specific impulses, and should therefore be considered.

REFERENCES

- A1. P.J. Wilbur and H.R. Kaufman, "Scaling Relationships for Mercury and Gaseous Propellant Ion Thrusters," AIAA Paper 78-667, April 1978.

APPENDIX B

DETERMINATION OF MULTIPLY CHARGED ION EFFECTS

Operation of the gas thruster at a specified thrust level and specific impulse defines the propellant flow rate to the thruster. If the production and loss rates of both ionic species (singly and doubly charged) are required to balance and the loss rate of propellant is required to be equal to its supply rate, then the neutral to singly ionized atom density ratio is given by

$$\frac{n_o}{n_+} = \frac{Z_+^{++}}{Z_o^+} + C, \quad (B.1)$$

where the quantities n_o and n_+ represent, respectively, the densities of neutrals and singly charged ions, and the Z 's represent the primary electron rate factors for transition from the subscripted to the superscripted states. The effect of Maxwellian electrons has been neglected in this analysis because their effect is calculated to be small. The plasma parameter C defined in Eq. B.1 is given by

$$C = \left(\frac{4v_+}{F_+v_o} \right) \left(\frac{A_s}{A_A} \right) \left(\frac{1 - \eta_i}{\eta_i} \right), \quad (B.2)$$

where v_+ is the Bohm velocity for singly charged ions, v_o is the thermal velocity for neutral atoms, F_+ is the uniformity factor for singly charged ions, A_s is the effective open area of the screen grid to ions, A_A is the effective open area of the grid system to neutrals, and η_i is the ionization efficiency defined by

$$\eta_i = \frac{\Gamma_+ + \Gamma_{++}}{\Gamma_o},$$

where Γ_+ and Γ_{++} are the fluxes of singly and doubly charged ions that have left the discharge chamber through the ion beam, and Γ_o is the

flux of neutral atoms into the discharge chamber. For xenon propellant, a neutral atom temperature of about 800°K, a Maxwellian electron temperature of about 4 eV, and effective open-area fractions for the screen and accelerator grids of 0.7 and 0.2, respectively, Eq. B.2 becomes

$$C = \frac{70}{F_+} \frac{(1 - \eta_1)}{\eta_1} \quad . \quad (B.3)$$

The propellant utilization is left as a parameter to facilitate the optimization of the total design, and the uniformity factor for singly charged ions also appears because of the uncertainty in the proper value for this parameter. This uncertainty comes about because of the small amount of test data available for both the multipole configuration and argon and xenon propellants.

Once the ratio of densities of neutral atoms to singly charged ions is known, the ratio of doubly to singly charged ion fluxes can be determined using

$$\frac{\Gamma_{++}}{\Gamma_+} = \frac{F_{++}}{CF_+} \frac{Z_{++}}{Z_+} \quad . \quad (B.4)$$

This equation is a result of equating the production and loss rates of doubly charged ions. To evaluate it, the assumption of approximately equal uniformity factors for doubly and singly charged ions has been made ($F_{++} = F_+$). Investigating the behavior predicted by Eq. B.4 for xenon, Figure B-1 shows the variation of the ion flux ratio for variation of the parameter C, with the potential difference between the anode and keeper ($V_D - V_K$) as a parameter and using the rate factors given in Table B-1. This parameter enters because the rate factors^{B-1} appearing in Eq. B.1 are dependent on primary electron energy, which is approximately equal to this potential difference.

ORIGINAL PAGE IS
OF POOR QUALITY

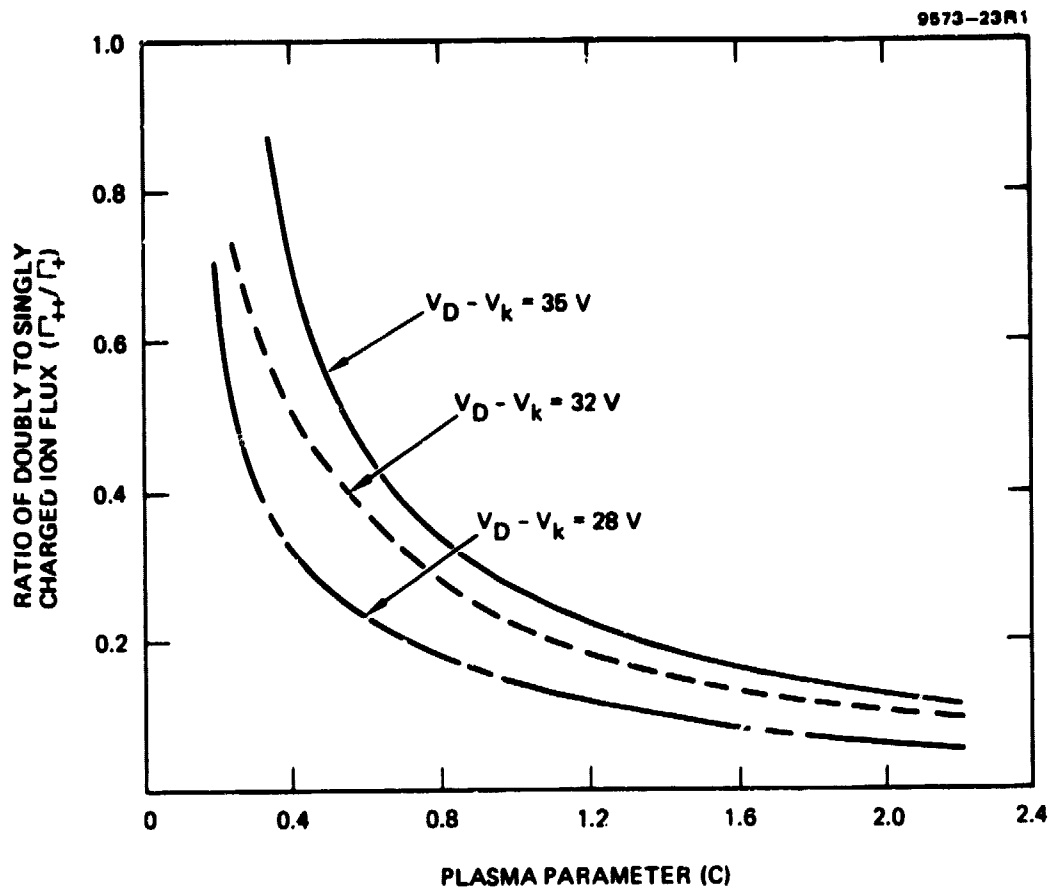


Figure B-1. Variation of the ratio of doubly charged ion flux to singly charged ion flux as a function of the plasma parameter C (xenon propellant).

Table B-1. Xenon Rate Factors

$V_D - V_K$	$Z_+^{++}, m^3/sec$	$Z_0^+, m^3/sec$
40	5.6×10^{-14}	16.5×10^{-14}
36	4.1×10^{-14}	15×10^{-14}
34	3.8×10^{-14}	14.7×10^{-14}
32	3.15×10^{-14}	13.8×10^{-14}
30	2.45×10^{-14}	12.8×10^{-14}
28	1.75×10^{-14}	11.8×10^{-14}

7013

Multiplying the flux ratio determined from Figure B-1 by two yields the ratio of doubly to singly ionized currents; dividing the flux ratio by $\sqrt{2}$ yields the particle density ratio for the two species. This figure shows that the doubly charged ion flux ratio rises rapidly as C is reduced to very low values. This can be realized physically by increasing the utilization to values very near unity, a condition that would correspond to operation with an excessively large volume-to-surface area region for the prevailing densities in the chamber. Low values of the plasma parameter C can also be realized if there are steep gradients in plasma properties near boundaries. This condition is reflected in an increase in the value of the uniformity factor F_+ .

Under some operating conditions for the xenon thruster, the doubly charged ion density can become comparable to the singly charged ion density. When this occurs, the possibility of significant triply charged ion production becomes a concern. The dominant reaction whereby these ions are formed is



Computation of the density of the triply charged specie requires as input the cross-section curves for the reaction. Figure B-2 shows

ORIGINAL PAGE IS
OF POOR QUALITY

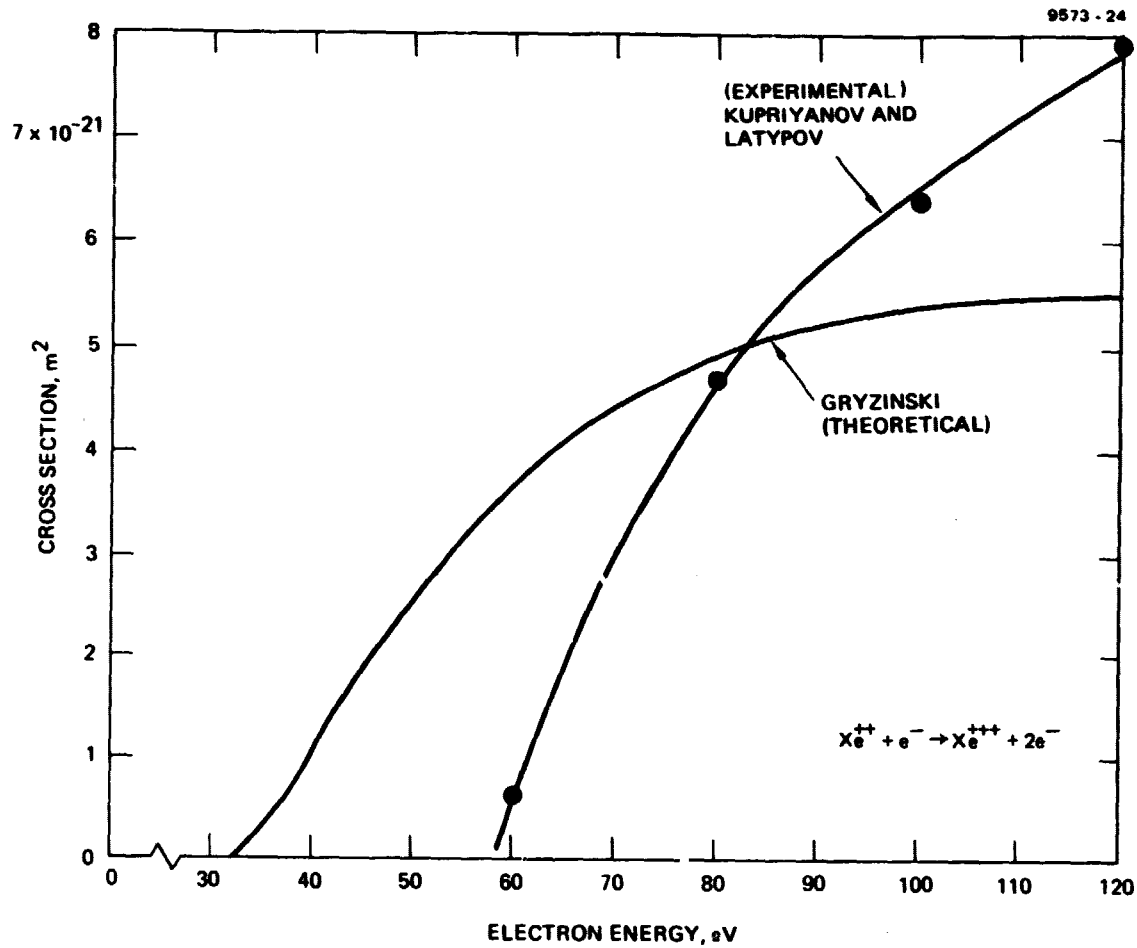


Figure B-2. Cross section for production of triply ionized xenon.

C-2

experimental data for this reaction obtained by Kupriyanov and Latypov.^{B-1} These data suggest that the density of triply charged ions would not be significant because the energies required for significant production (~60 eV) would probably not be available. There is, however, a question about the suitability of these data for the application considered here, both because of possible errors pointed out by the authors and because the cross section is essentially zero in the region immediately above the 32.1-V ionization potential associated with the reaction.

To determine what would appear to be a more reasonable cross section, a theoretical approach due to Gryzinski^{B-3} was used to calculate them:

$$\sigma = \sum_i \frac{6.56 \times 10^{-10}}{U_i^2} \left\{ \frac{1}{X_i} \left(\frac{X_i - 1}{X_i + 1} \right)^{3/2} \left(1 + \frac{2}{3} \left[1 - \frac{1}{2X_i} \right] \ln \left\{ 2.7 + (X_i - 1)^{1/2} \right\} \right) \right\}, \quad (B.6)$$

where $X_i = E/U_i$, E is the energy of the ionizing electron (eV), and U_i is the ionization potential (eV) for the i^{th} electron. The only electrons that need to be considered in the above summation are the four 5p electrons left in the outer shell of doubly ionized xenon. Evaluating the above as a function of energy yields the theoretical curve shown in Figure B-2.

Using the theoretical curve results of Figure B-2, the primary electron rate factor Z_{++}^{+++} (m^3/sec) inducing the subject reactions can be determined from

$$Z_{++}^{+++} = \sigma v_e = \sigma \sqrt{\frac{2E}{m_e}} = 9.56 \times 10^5 \sigma \sqrt{E}. \quad (B.7)$$

Values obtained from this equation and the theoretical curve of Figure B-2 will be used in subsequent analysis because they will give higher values of the rate factor and thereby assure a conservative design.

**ORIGINAL PAGE IS
OF POOR QUALITY**

Equating the production and loss rates of the triply charged xenon gives the ratio of triply to doubly charged ion densities (n_{+++}/n_{++}),

$$\frac{n_{+++}}{n_{++}} = \frac{F_{+++}}{v_{+++}} Z_{++}^{+++} \left(\frac{v_p}{A_p} \right) n_p \quad , \quad (B.8)$$

where F_{+++} is the uniformity factor for triply charged ions, n_p is the primary electron density, v_{+++} is the Bohm velocity for triply charged ions, and v_p/A_p is the volume to surface area ratio of the primary electron region of the thruster. The loss rate of doubly charged ions resulting from the production of triply charged ions should be accounted for; for the case being considered here, however, the triply charged ion production is sufficiently small that this correction would be insignificant. From previous work, the Bohm velocity and primary electron density are given by

$$v_{+++} = \sqrt{3} v_+ \quad (B.9)$$

and

$$n_p = \frac{A_p v_+ / \gamma_p}{C F_+} \left(\frac{1}{Z_o^+ + \frac{n_+}{n_o} Z_+^{++}} \right) \quad . \quad (B.10)$$

Combining Eqs. B.8 through B.10 and using the above numerical values yield

$$\frac{n_{+++}}{n_{++}} = \frac{1}{\sqrt{3} C} \left(\frac{Z_{++}^{+++}}{Z_o^+ + \frac{n_+}{n_o} Z_+^{++}} \right) \quad . \quad (B.11)$$

For the case of interest here, where $C = 0.65$, the rate factors are given by Table B-1 and Figure B-2, and the density ratio is computed using Eq. B.11 to obtain the values in Table B-2.

ORIGINAL PAGE IS
OF POOR QUALITY

Table B-2. Triply Charged Ion Density as a Function
of Primary Electron Energy ($V_D - V_K$)

$V_D - V_K$	n_+/n_o	$Z_{++}^{+++}, m^3/sec$	n_{+++}/n_{++}
40	1.18	6.53×10^{-15}	0.027
35	1.09	1.70×10^{-15}	0.008
32	1.02	0	0

7013

The ratio of triply charged ion flux (Γ_{+++}) to doubly charged ion flux (Γ_{++}) is given by

$$\frac{\Gamma_{+++}}{\Gamma_{++}} = \sqrt{\frac{3}{2}} \frac{n_{+++}}{n_{++}} = 1.22 \frac{n_{+++}}{n_{++}}, \quad (B.12)$$

and the ratio Γ_{+++}/Γ_+ is given by

$$\frac{\Gamma_{+++}}{\Gamma_+} = 1.22 \frac{n_{+++}}{n_{++}} \frac{\Gamma_{++}}{\Gamma_+}. \quad (B.13)$$

Because the triply charged ion flux will be small, it can be neglected in all of the following analysis except that associated with screen grid erosion. Neglecting triply charged ions and using the definition of specific impulse while expressing the combined thrust of both singly and doubly charged ions in terms of the net accelerating voltage (V_b) and the flux of each ionic species, one obtains the following expression for net accelerating voltage:

$$V_b = \frac{I_{sp}^2 m_o g_o^2}{2e \eta_i^2} \left[\frac{1 + \Gamma_{++}/\Gamma_+}{1 + \sqrt{2} \Gamma_{++}/\Gamma_+} \right]^2. \quad (B.14)$$

Substituting into this equation the xenon atomic mass [$m_o = (131)$ (1.67×10^{-27} kg)], the acceleration due to gravity ($g_o = 9.8 \text{ m/sec}^2$), the specific impulse ($I_{sp} = 3530 \text{ sec}$), and the electron charge ($1.6 \times 10^{-19} \text{ C}$) yields:

ORIGINAL PAGE IS
OF POOR QUALITY

$$v_b \eta_1^2 = 818 \left[\frac{1 + \Gamma_{++}/\Gamma_+}{1 + \sqrt{2} \Gamma_{++}/\Gamma_+} \right]^2 \quad (B.15)$$

For the case under consideration, the results of doing this are shown graphically in Figure B-3, where the left side of Eq. B.15 (net accelerating voltage parameter) is plotted against the parameter C.

The beam current which would be measured from the thruster is given by

$$J_b = e \left(\Gamma_+ + 2\Gamma_{++} \right) = \eta_1 J_o \left(\frac{1 + 2\Gamma_{++}/\Gamma_+}{1 + \Gamma_{++}/\Gamma_+} \right) \quad (B.16)$$

where J_o is the neutral flow rate into the thruster in units of A equiv. This flow rate is fixed under the constraint of operation at a specified specific impulse and thrust (T) by the expression defining specific impulse (I_{sp}):

$$J_o = \frac{eT}{I_{sp} m_o g_o} \quad (B.17)$$

The neutral propellant flow rate determined from Eq. B.17 for the case of xenon propellant at a 3530-sec specific impulse and a 0.5-N thrust level is 10.6 A. The beam current as determined from the results of Figure B-1 and Eq. B.16 is given in Figure B-4 as a function of the parameter C. The decrease in beam current as C increases is a result of corresponding reductions in the doubly to singly charged ion flux ratio (Figure B-1).

The beam current and net acceleration voltage required to effect operation under the specified specific impulse and thrust conditions can also be computed; the equations for these two quantities become

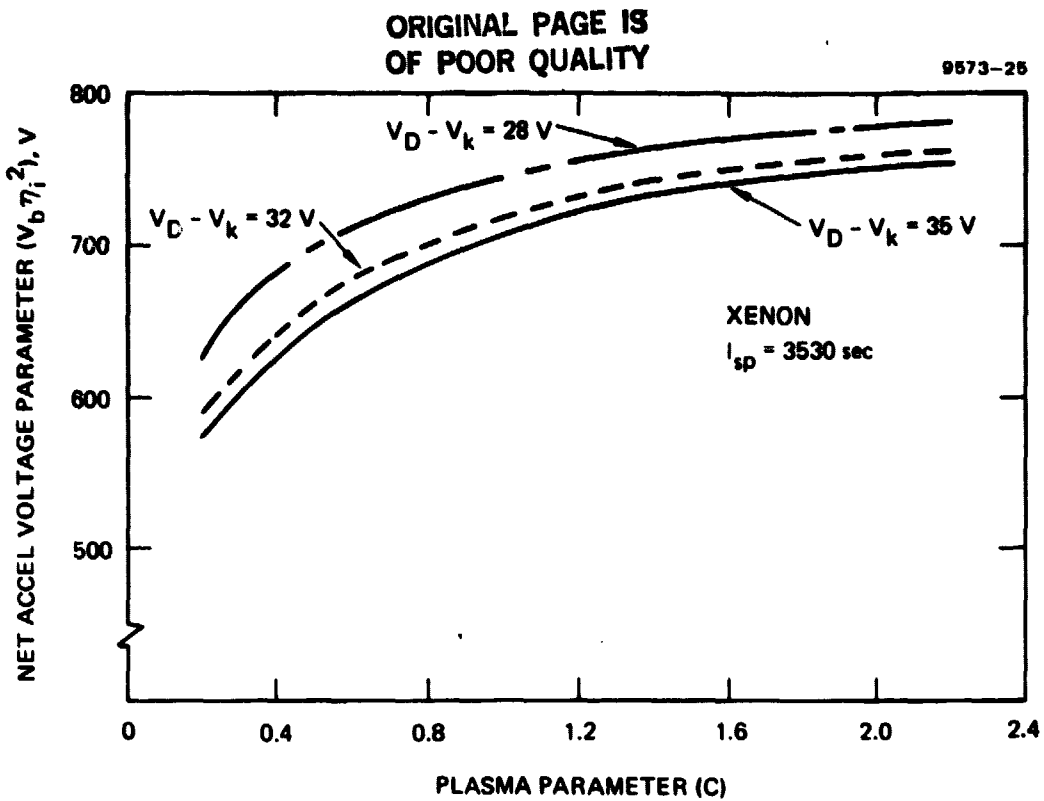


Figure B-3. Net acceleration voltage parameter variation.

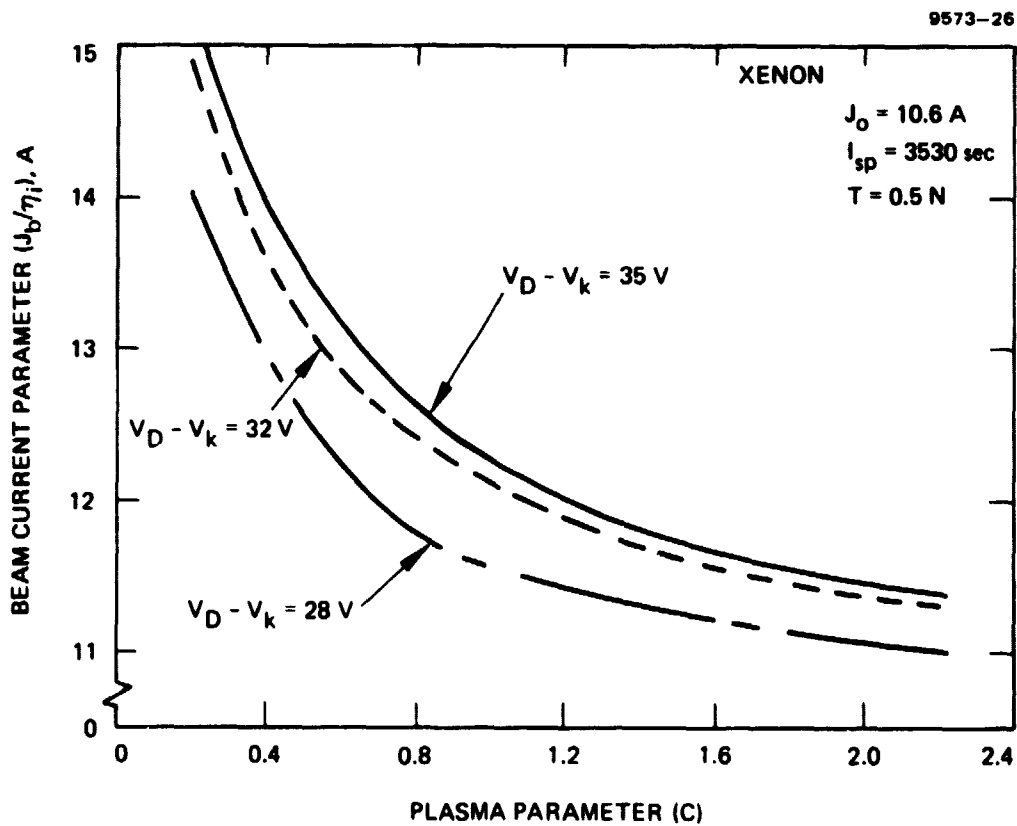


Figure B-4. Beam current parameter variation.

ORIGINAL PAGE IS
OF POOR QUALITY

$$J_b = \eta_1 J_o \left[\frac{1 + 2\Gamma_{++}/\Gamma_+ + 3\Gamma_{+++}/\Gamma_+}{1 + \Gamma_{++}/\Gamma_+ + \Gamma_{+++}/\Gamma_+} \right] \quad (B.18)$$

and

$$V_b = \frac{818}{\eta_1^2} \left[\frac{1 + \Gamma_{++}/\Gamma_+ + \Gamma_{+++}/\Gamma_+}{1 + \sqrt{2} \Gamma_{++}/\Gamma_+ + \sqrt{3} \Gamma_{+++}/\Gamma_+} \right]^2 \quad (B.19)$$

For the levels of triply charged ions encountered here, however, this current and voltage are not altered significantly from the values that neglect triply charged ions.

It is convenient to be able to calculate the thrust of an ion source from measured beam currents as net accelerating voltages. The ratio of the actual thrust to that calculated using these quantities is referred to as the thrust correction factor for doubly charged ions, α . It is plotted against the parameter C in Figure B-5.

The ionization efficiencies achievable using argon as the propellant do not cause nearly as much double ionization as when the thruster is operated with xenon, and formation of triply charged ions is negligible. Design curves comparable to those shown for xenon (as functions of the plasma parameter C) are shown in Figures B-6 through B-9 for operation of a thruster on argon.

ORIGINAL PAGE IS
OF POOR QUALITY

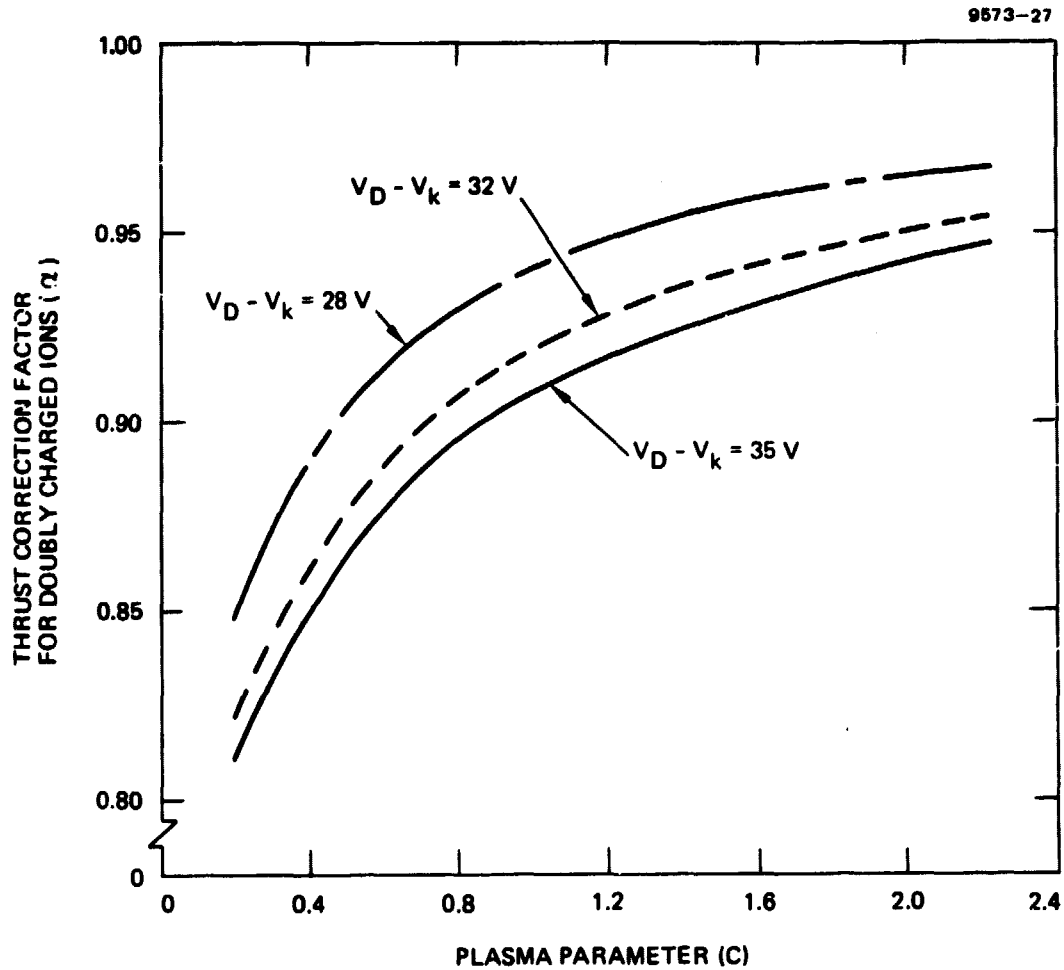


Figure B-5. Variation of the thrust correction factor for doubly charged ions, α , as a function of the plasma parameter C (with $V_D - V_k$ as a parameter). Xenon propellant.

ORIGINAL PAGE IS
OF POOR QUALITY

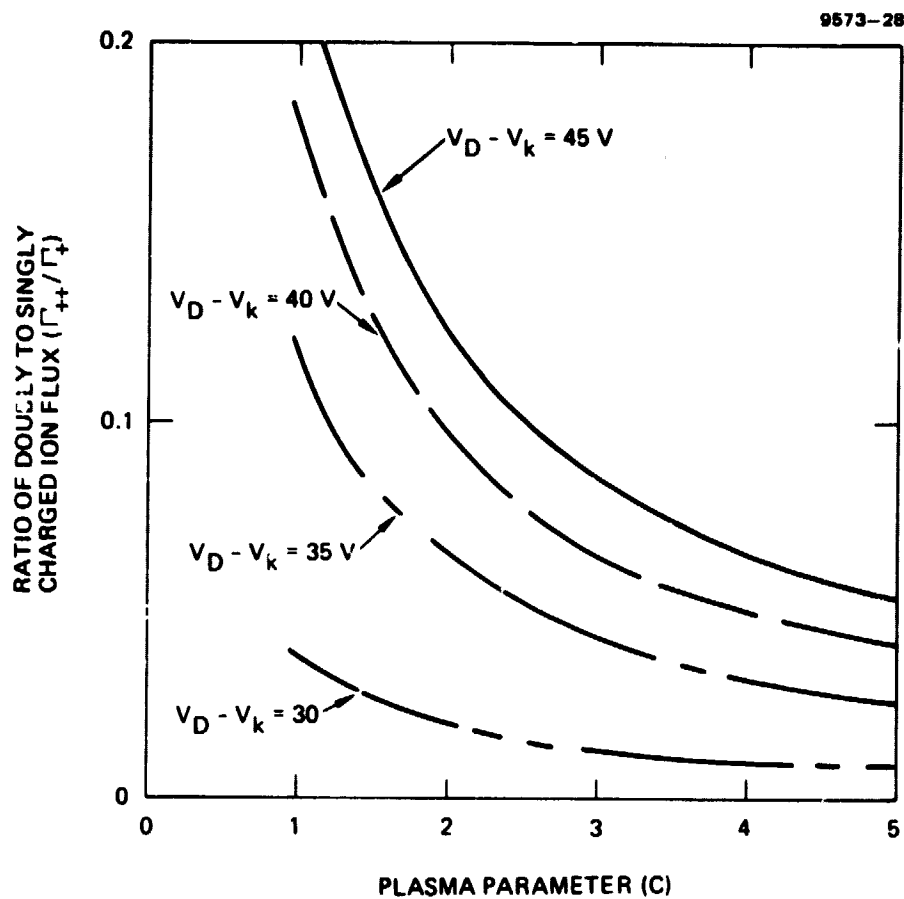


Figure B-6. Variation of the ratio of doubly to singly charged ion flux as a function of the plasma parameter C. Argon propellant.

ORIGINAL PAGE IS
OF POOR QUALITY

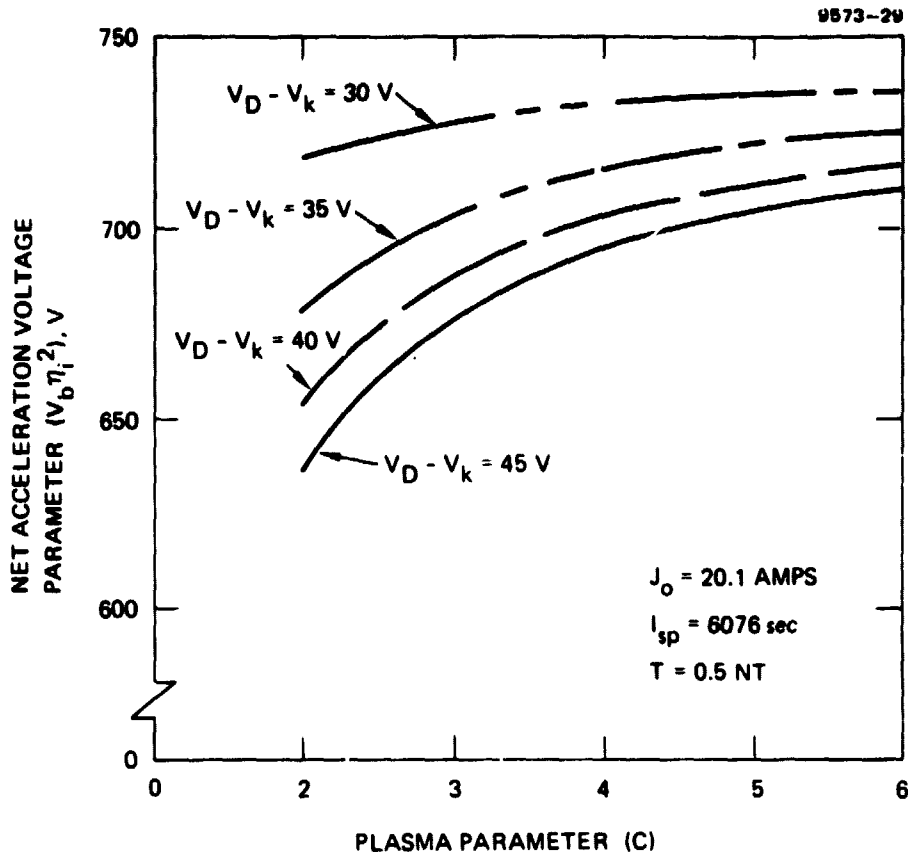


Figure B-7. Variation of the net acceleration voltage parameter as a function of the plasma parameter C. Argon propellant.

ORIGINAL PAGE IS
OF POOR QUALITY

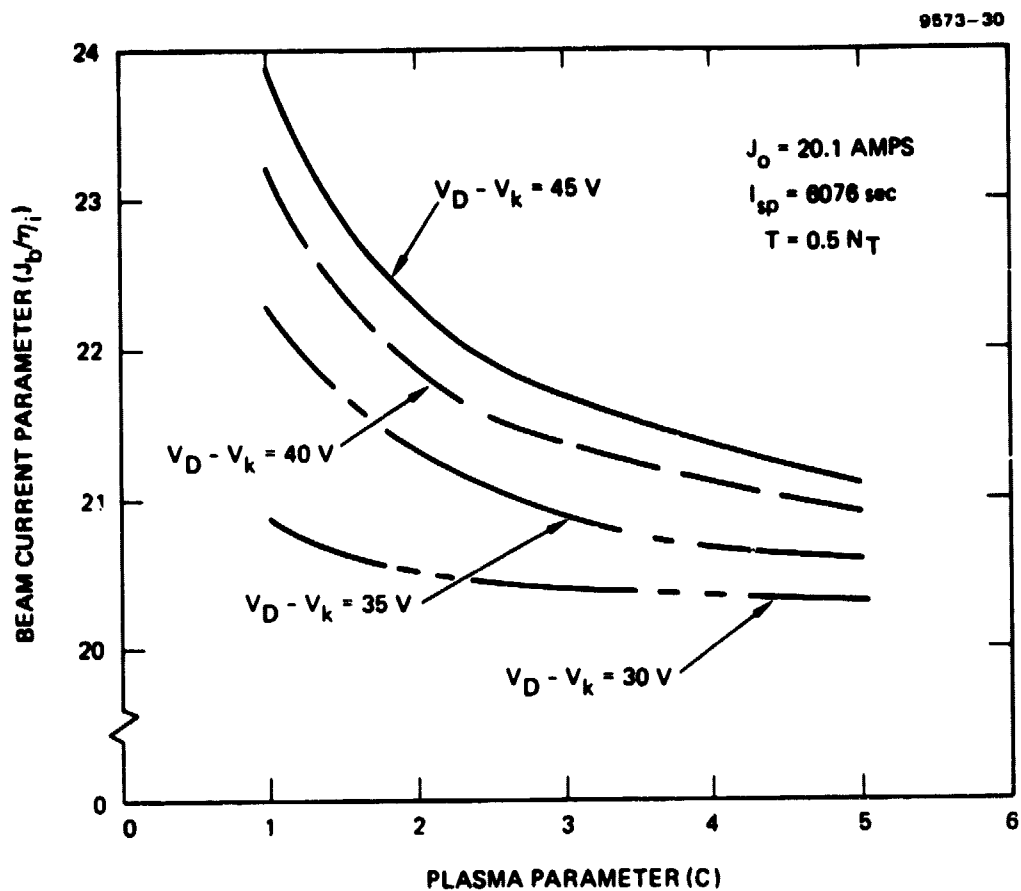


Figure B-8. Variation of the beam current parameter as a function of the plasma parameter C. Argon propellant.

ORIGINAL PAGE 15
OF POOR QUALITY

9873-31

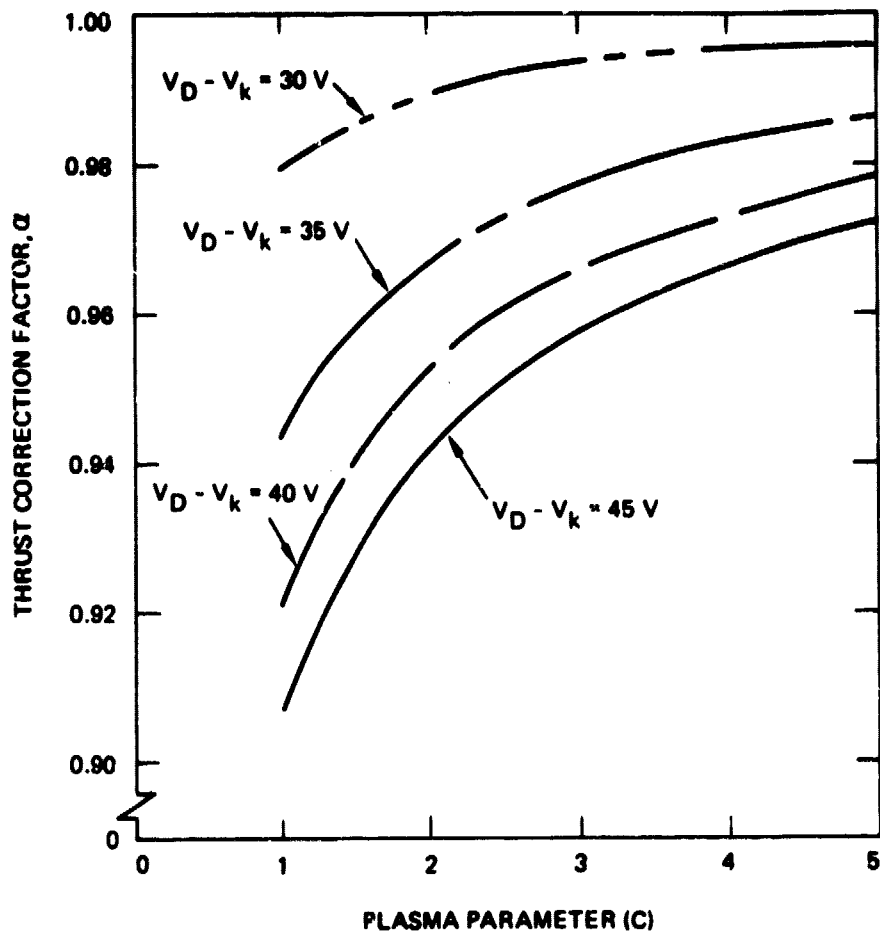


Figure B-9. Variation of the thrust correction factor, α , as a function of the plasma parameter C. Argon propellant.

REFERENCES

- B1. P.J. Wilbur and H.R. Kaufman, "Scaling Relationships for Mercury and Gaseous Propellant Ion Thrusters," AIAA Paper 78-667, April 1978.
- B2. S.E. Kupriyanov and Z.Z. Latypov, "Ionization of Positive Ions by Electrons," JETP (USSR) 45, 815-816, September 1963 and Latypov, Kupriyanov, Tunitshii, "Ionizing Collisions of Electrons with Ions and Atoms," Soviet Physics JETP 19, No. 3, 570-574, September 1964.
- B3. M. Gryzinski, "Classical Theory of Atomic Collisions. I. Theory of Inelastic Collisions," Phys. Rev. 138, No. 2A, A336-A358, April 1965.